Towards Dependability of Ultra Lightweight Tendon Driven Series Elastic Robots

TECHNISCHE
UNIVERSITÄT
DARMSTADT

Am Fachbereich Informatik der
Technischen Universität Darmstadt
zur Erlangung des akademischen Grades eines
Doktor-Ingenieurs (Dr.-Ing.)
eingereichte

Dissertation

von

M.Sc. Jérôme Kirchhoff
(geboren in Frankfurt am Main)

Erstgutachter: Prof. Dr. Oskar von Stryk
Zweitgutachter: PD Dr.-Ing. habil. Dirk Wollherr
(Technische Universität München)

Darmstadt 2017

Kirchhoff, Jérôme: Towards Dependability of Ultra Lightweight Tendon Driven Series Elastic Robots
Darmstadt, Technische Universität Darmstadt

Jahr der Veröffentlichung der Dissertation auf TUprints: 2018
URN: urn:nbn:de:tuda-tuprints-76375
URL: http://tuprints.ulb.tu-darmstadt.de/id/eprint/7637
Tag der Einreichung: 30.06.2017
Tag der mündlichen Prüfung: 16.08.2017

Contents

Abstract

Ultra lightweight tendon driven series elastic robots exhibit unique high safety features based on very low moving link masses and mechanical decoupling of actuator inertias from links. These make them highly suitable for safe physical human-robot interaction and collaboration. However, such actuation approach introduces a number of challenges to be overcome in order to capitalize on their advantages. These include some inherent uncertainties regarding their dependability, which mainly result from the combination of possible changes in the drive train caused by wear, unavoidable system model inaccuracies, and the high mechanical elasticities facilitating oscillations in the joints. It is shown that the resulting challenges, in particular influencing the performance in velocity estimation, robust torque transmission, trajectory control, and human-robot collaboration, can to a large extent be overcome. Thereby, achieving dependable usage of such robots marks a key step towards utilizing their unique high safety features for physical human-robot collaboration in industrial applications. In order to get an insight into the safety capabilities as a collaborative robot, a risk analysis according to the new ISO/TS 15066 has been performed comparing the class of tendon driven ultra lightweight series elastic robots with downscaled and stiff robots. Further, the influence of high compliance during contact situations has been demonstrated during a collision test.

In lightweight and downscaled robotic structures, the suitable joint position sensor size is limited, resulting in a relatively coarse discrete position signal. Furthermore, joint elasticities facilitate fast and oscillating motions containing a broad bandwidth of frequencies and velocities. In order to effectively damp the controlled motion and also for model-based computations, an accurate velocity estimation is essential. Kalman filter approaches already showed accurate performance in position signal based velocity estimation, but within a small bandwidth that correlates with the filter's measurement variance parameter. In order to create an estimation approach more suitable for the considered concept of tendon driven series elastic actuation, the velocity and frequency dependent optimal measurement variance parameter has been analyzed. The observed parameter characteristics serve as the basis for the proposed new measurement variance update rule. The resulting novel adaptive Kalman filter approach adapts better to the investigated application than the compared state-of-the-art approach. It produces a smoother and more accurate velocity estimation, as will be demonstrated in virtual and real robot experiments.

In biologically inspired mechanical structures, tendons are used to transmit forces along a kinematic chain, which must satisfy high robustness requirements by simultaneously allowing small pulley radii. Cables or belts are often not applicable due to size and force requirements in contrast to thin synthetic fiber ropes. Besides the breaking force, only a little information about the ropes is provided by the manufacturer. Thus, further research is required to investigate whether a rope is suitable to be used as a reliable component of a drive train which mainly depends on its elongation behavior. In this regard, new systematic creep experiments regarding different materials, manufacturers, and diameters, as well as bending experiments are presented in this

work. The findings obtained for the rope characteristics support the material selection decisions during the system design process and give insights into the long-term behavior. In order to monitor the long-term behavior, an observer approach is presented which does not need joint torque measurements but nevertheless enables elongation detection in tendon driven kinematic chains even subject to model inaccuracies. This has been demonstrated in simulated and real robot experiments.

In an industrial application, a robotic system is expected to perform a motion without alterations over time accurately. The inherent uncertainties of the elastic tendon driven actuation can strongly influence the control performance and, thus, the reliability of the robot motion. State-of-the-art control approaches for joint elastic robot arms rely on accurate joint torque measurements and accurate models of drive train dynamics. Available torque sensors with a suitable torque range are heavy and large and do not fit into the lightweight actuation. Thus, so far only erroneous model-based joint torque estimation and consequently inaccurate load dependent friction models can be used, for which these control approaches perform unsatisfactorily. With the aim to reduce the model dependency, the performance of a friction observer under joint torque estimation errors is investigated in this thesis. This leads to the final proposed controller design that is able to compensate for both, drive train and load dynamics model inaccuracies. In particular, it integrates a friction observer into a state space approach without the need for explicit joint torque measurements eliminating the steady-state control errors and realizes contact handling. The resulting control performance has been evaluated in simulated and real robot experiments demonstrating an accurate and damped motion performance.

An essential part of human-robot collaboration consists of physical interaction for joint task solving. To perceive physical interactions, the robotic arm must be able to estimate external forces. This can be achieved by disturbance observers, which only use internal data and are therefore suitable for the regarded system. In this thesis, the accuracy limitations are investigated and discussed theoretically and via simulated robot experiments to reveal the capabilities of tendon driven joint elastic robots regarding external torque estimations. Furthermore, the user should be able to teach the needed robot motion for the executed process without high effort. For this purpose, a teach-in controller that enables hand guided motions even under drive train model errors is presented and evaluated in realistic simulation. Besides the physical interaction, successful collaboration requires clear communication between the human and robot. To investigate the influence of robot state visualizations on the user's situational awareness and robot's intention estimation in collaborative task solving, a preliminary user study is conducted. Further, metrics for wear estimation are introduced and discussed to support the human during the assessment of the robot's integrity and serve to increase trust in collaboration.

Keywords: physical human-robot interaction, cobots, tendon driven compliant actuation, velocity estimation, synthetic fiber ropes, trajectory tracking, human-robot collaboration

Zusammenfassung

Sehnengetriebene, serienelastische Ultraleichtbauroboter weisen einzigartige Sicherheitseigenschaften auf, die auf ihrer sehr geringen Masse der sich bewegenden Teile, sowie der mechanischen Entkopplung der Motor- und Gliederträgheiten basieren. Dadurch sind sie besonders gut für die sichere physikalische Mensch-Roboter-Interaktion und -Kollaboration geeignet. Allerdings gehen mit diesem Antriebskonzept auch inhärente Unsicherheiten hinsichtlich der Zuverlässigkeit einher, die hauptsächlich aus der Kombination von Verschleißerscheinungen, unvermeidlichen Modellungenauigkeiten und den hohen mechanischen Elastizitäten, die Schwindungen in den Gelenken begünstigen, resultieren. Um die oben genannten Vorteile des Antriebskonzepts nutzen zu können, muss daher zunächst eine Reihe von Herausforderungen überwunden werden. Es zeigt sich, dass diese Herausforderungen, insbesondere die Leistungsfähigkeit der Geschwindigkeitsschätzung, die robuste Drehmomentübertragung, die Trajektorienregelung und die Mensch-Roboter-Kooperation, weitgehend überwunden werden können. Der damit einhergehende, zuverlässige Einsatz solcher Roboter ist ein wichtiger Schritt zur Nutzung ihrer einzigartigen Sicherheitsfunktionen für die physikalische Mensch-Roboter-Kollaboration in industriellen Anwendungen. Um einen Einblick in die Sicherheitseigenschaften im Einsatz als kollaborierende Roboter zu erhalten, wurde eine Risikoanalyse gemäß der neuen ISO/TS 15066 durchgeführt und die Klasse von sehnengetriebenen, serienelastische Ultraleichbauroboter mit den weit verbreiteten, herunterskalierten, steifen Roboter verglichen. Zudem wurde durch einen Kollisiontest der Einfluss von hoher Nachgiebigkeit in Kontaktsituationen aufgezeigt.

In leichtgewichtigen und herunterskalierten Roboterstrukturen ist die einsetzbare Größe der Positionssensoren begrenzt, was zu einem relativ groben, diskreten Positionssignal führt. Darüber hinaus erleichtern Gelenkelastizitäten schnelle und schwingende Bewegungen mit einer großen Bandbreite von Frequenzen und Geschwindigkeiten. Für eine effektiv gedämpft-geregelte Bewegung, aber auch für modellbasierte Berechnungen, ist eine genaue Geschwindigkeitsschätzung unerlässlich. Kalman-Filter-Ansätze zeigten bereits genaue Ergebnisse bei der Positionssignalbasierten Geschwindigkeitsschätzung, aber lediglich innerhalb einer kleinen Bandbreite, die mit dem Messvarianzparameter des Filters korreliert. Um für das betrachtete Antriebskonzept ein geeignetes Verfahren zu entwickeln, wird in der vorliegenden Arbeit der geschwindigkeits- und frequenzabhängige optimale Filterparameter der Messvarianz zunächst analysiert. Die hierbei beobachteten Parametereigenschaften dienen als Basis für die vorgestellte, neue Aktualisierungsvorschrift der Messvarianz. Der resultierende, neuartige adaptive Kalman-Filter-Ansatz ist für die betrachtete Anwendung besser als der verglichene State-of-the-Art-Ansatz geeignet, da eine glattere und genauere Geschwindigkeitsschätzung erzeugt wird.

In biologisch inspirierten, mechanischen Strukturen werden Sehnen zur Übertragung von Kräften entlang einer kinematischen Kette verwendet, welche hohen Ansprüchen an Robustheit genügen und gleichzeitig kleine Umlenkradien ermöglichen müssen. Aufgrund der Anforderungen an die Größe und die zu übertragene Kraft sind Drahtseile und Riemen hier häufig nicht einsetzbar – im Gegensatz zu Synthetikfaserseile. Über die Reißkraft hinaus werden von den

Herstellern hierzu allerdings nur wenige Produktinformationen bereitgestellt. Daher sind weitere Untersuchungen notwendig, um zu ermitteln, ob ein Seil als zuverlässige Komponente des Antriebs geeignet ist, was hauptsächlich von dem Längungsverhalten abhängt. Hierzu werden in der vorliegenden Arbeit neue, systematische Kriechversuche bzgl. verschiedener Materialien, Hersteller und Durchmesser sowie Biegeversuche vorgestellt. Die erlangten Erkenntnisse über die Seileigenschaften unterstützen die Entscheidung zur Materialauswahl während der Entwicklungsphase eines Systems und geben Einblicke in das Langzeitverhalten. Zur Überwachung des Langzeitverhaltens, wird ein in Simulationen und Roboterexperimenten evaluiertes, beobachterbasiertes Verfahren vorgestellt, welches ohne Gelenkdrehmomentmessung auskommt und dennoch eine Erkennung der Seillängung auch unter Modellungenauigkeiten ermöglicht.

In einer industriellen Anwendung wird erwartet, dass ein Robotersystem eine Bewegung präzise und ohne Änderungen im Zeitverlauf durchführt. Die geschilderten Unsicherheiten der elastischen Sehnenantriebe können die Regelungsgenauigkeit und damit die Zuverlässigkeit der Roboterbewegung jedoch stark beeinflussen. Moderne Regelungsansätze für gelenkelastische Roboterarme beruhen auf genaue Gelenkmomentmessungen und Dynamikmodelle. Verfügbare Drehmomentsensoren mit einem geeigneten Drehmomentbereich sind allerdings schwer und groß und passen daher nicht zu dem Leichtgewichtsantriebskonzept. Daher können bislang lediglich fehlerbehaftete, modellbasierte Drehmomentschätzungen und damit ungenaue, lastabhängige Reibungsmodelle verwendet werden, mit denen die bisherigen Regelungsansätze keine zufriedenstellenden Ergebnisse zeigen. Mit dem Ziel, die Modellabhängigkeiten zu reduzieren, wird in der vorliegenden Arbeit die Leistung eines Reibungsbeobachters unter fehlerhaften Drehmomentschätzungen untersucht. Als Ergebnis wird ein Regelungsentwurf vorgeschlagen, der Ungenauigkeiten sowohl im Antriebsstrang als auch der Roboterdynamik ausgleicht. Dieser Regelungsentwurf integriert einen Reibungsbeobachter in einen Zustandsregelungsansatz ohne die Notwendigkeit einer expliziten Drehmomentmessung, eliminiert Restregelabweichungen und ermöglicht Kontaktsituationen.

Ein wesentlicher Bestandteil einer Mensch-Roboter-Kollaboration ist unter anderem die physikalische Interaktion zur Lösung von gemeinsamen Aufgaben. Um diese zu erfassen, muss der Roboterarm externe Kräfte schätzen können. Dies kann durch Störungsbeobachter, die lediglich auf Basis interner Daten arbeiten und damit für das betrachtete System geeignet sind, geschehen. In der vorliegenden Arbeit werden die Genauigkeitseinschränkungen dieser Ansätze theoretisch und in simulierten Roboterexperimenten untersucht. Ziel ist es, die Fähigkeiten von sehnengetriebenen, gelenkelastischen Robotern zur Schätzung externer Drehmomente aufzudecken. Zudem sollte es dem Benutzer möglich sein, die auszuführenden Bewegungen ohne hohen Aufwand einzulernen. Zu diesem Zweck wird ein Teach-In-Regler, der handgeführte Bewegungen auch unter fehlerhaften Antriebsmodellen ermöglicht, vorgestellt und in realistischen Simulationen evaluiert. Neben der physikalischen Interaktion erfordert eine erfolgreiche Kollaboration darüber hinaus eine klare Kommunikation zwischen Mensch und Roboter. Zur Untersuchung der Einflüsse von Roboterzustandsvisualisierungen auf das Situationsbewusstsein des Benutzers und die Schätzung der Roboterintention während kollaborativer Aufgaben wird eine vorläufige Benutzerstudie durchgeführt. Außerdem werden Metriken zur Verschleißschätzung eingeführt und diskutiert, die den Menschen dabei unterstützen, die Intaktheit des Roboters zu beurteilen.

Stichworte: physikalische Mensch-Robot-Interaktion und -Kollaboration, Cobots, nachgiebige Sehnenaktuierung, Geschwindigkeitsschätzung, Synthetikfaserseile, Trajektorienverfolgung

Acknowledgments

This thesis was written during my time as a research assistant at the Simulation, Systems Optimization, and Robotics Group (SIM) at the Department of Computer Science of Technische Universität Darmstadt. Parts of my research have been supported by the Hessian State Ministry of Higher Education, Research, and the Arts (HMWK).

Many people accompanied me and supported my work during the time creating this thesis for which I am very grateful, even if they are not explicitly named below. These are especially my colleagues and students with whom I was lucky to work with.
My supervisor Oskar von Stryk gave me the opportunity to work as a research assistant, which paved the way for the completion of this thesis. I would like to thank him for his patience and continuous support over the last years, in particular, the encouraging and valuable discussions and making it possible to work on a fascinating robotics field. Likewise, I want to thank PD Dr.-Ing. habil. Dirk Wollherr for agreeing to become my second referee, his interest in my work and reassuring feedback.

A special thanks for his support goes to my former colleague Thomas Lens who first introduced me to the topic of ultra lightweight series elastic actuated robots as supervisor of my bachelor's and master's thesis, which guided my way to SIM. I am also particularly grateful for all the constructive discussions over the last years with Janis Wojtusch. Further, I really appreciate the support of Frank Blasch, Juliane Euler, Dorian Scholz, Marie Schumacher, and Marian Wieczorek for proofreading parts of this thesis.
I would also like to thank Jan Röhlinger, Michael Schanz, and Ralf Teichmann at Bionic Robotics GmbH for the good and fruitful cooperation.

Most of all, I want to thank my family for their constant support during my studies, I could not have finished the work on this thesis without them. Very special thanks go to Kathrin for all her patience and understanding about long work days and nights, but also her encouragement to complete this thesis.

List of Figures

List of Tables

List of Symbols

Remark: Hat above a variable represents the variable estimation.

Robot Kinematics and Dynamics

β	ratio of minimum to maximum effective mass of current joint configuration
$\boldsymbol{C}(\boldsymbol{q}, \dot{\boldsymbol{q}})$	matrix of centrifugal and Coriolis terms $\in \mathbb{R}^{N \times N}$, with N DoF
Δ_e	motor position offset caused by tendon elongation $\in \mathbb{R}$ written in bold for elongation offset vector $\boldsymbol{\Delta_e} \in \mathbb{R}^N$, with N DoF second subscript: indicates joint
F_c, F_L	friction model Coulomb and load coefficient $\in \mathbb{R}^N$, with N DoF subscript: indicates joint
$\boldsymbol{g}(\boldsymbol{q})$	gravity torque vector $\in \mathbb{R}^N$, with N DoF
I_g	gear box inertia $\in \mathbb{R}$
I_m	reflected motor and gear box inertia $\in \mathbb{R}$ written in bold for diagonal motor and gear box inertia matrix $\boldsymbol{I_m} \in \mathbb{R}^{N \times N}$, with N DoF
I_r	rotor inertia $\in \mathbb{R}$
$\boldsymbol{J_c}^{-1}$	tendon coupling matrix $\in \mathbb{R}^{N \times N}$, with N DoF
$\boldsymbol{J_g}$	diagonal gear box transmission ratio Jacobian $\in \mathbb{R}^{N \times N}$, with N DoF
$\boldsymbol{J_t}$	tendon Jacobian and coupling matrix $\in \mathbb{R}^{N \times N}$, with N DoF
$\boldsymbol{J_v}$	manipulator Jacobian sub matrix related to linear velocity $\in \mathbb{R}^{3 \times N}$, with N DoF
$\boldsymbol{K}$	diagonal joint stiffness matrix $\in \mathbb{R}^{N \times N}$, with N DoF
$\boldsymbol{K_{ad}}$	diagonal matrix of reciprocal admittance spring stiffness $\in \mathbb{R}^{N \times N}$, with N DoF
k_{ad}	admittance spring stiffness $\in \mathbb{R}$
k_e	joint stiffness $\in \mathbb{R}$ written in bold for joint stiffness vector $\boldsymbol{k_e} \in \mathbb{R}^N$ with N DoF second subscript: indicates joint
$\boldsymbol{\Lambda}$	end-effector inertial properties matrix (pseudo kinetic energy matrix)
$\boldsymbol{\Lambda_v^{-1}}$	linear end-effector pseudo kinetic energy matrix describing the translational response to a force

$\boldsymbol{M}(\boldsymbol{q})$	mass matrix $\in \mathbb{R}^{N \times N}$, with N DoF
$m_{\boldsymbol{u}}$	effective mass along a given direction $\boldsymbol{u}$ for current joint configuration $\boldsymbol{q}$
$\bar{m}$	mean effective mass of specific robot (robot name shown in subscript)
n_g	gear box ratio $\in \mathbb{R}$
n_t	transmission ratio $\in \mathbb{R}$
p, $\dot{p}$	link side generalized momentum and time derivative $\in \mathbb{R}$, with N DoF written in bold for generalized momentum vector, e.g., $\boldsymbol{p} \in \mathbb{R}^N$, with N DoF subscript: M indicates generalized momentum of motor instead of link
q, $\dot{q}$, $\ddot{q}$	angular joint position, velocity, and acceleration $\in \mathbb{R}$ written in bold for vectors, e.g., $\boldsymbol{q} \in \mathbb{R}^N$, with N DoF subscript: d for desired, m for discretized
R	radius of the joint pulley $\in \mathbb{R}$
R_s	radius at joint pulley to spring $\in \mathbb{R}$
r	radius of the motor pulley $\in \mathbb{R}$
θ, $\dot{\theta}$, $\ddot{\theta}$	angular motor position, velocity, and acceleration $\in \mathbb{R}$ written in bold for vectors, e.g., $\boldsymbol{\theta} \in \mathbb{R}^N$, with N DoF subscript: d for desired, r for rotor position before gear reduction superscript: e reflected to elastic actuator space, j reflected to joint space
τ_c	control torque $\in \mathbb{R}^N$, with N DoF written in bold for control torque vector $\boldsymbol{\tau_c} \in \mathbb{R}^N$, with N DoF
τ_{el}	elastic joint torque $\in \mathbb{R}$ written in bold for elastic joint torque vector $\boldsymbol{\tau_{el}} \in \mathbb{R}^N$, with N DoF second subscript: indicates joint superscript: e reflected to elastic actuator space, j reflected to joint space
τ_f	motor friction $\in \mathbb{R}^N$, with N DoF written in bold for motor friction vector $\boldsymbol{\tau_f} \in \mathbb{R}^N$, with N DoF
$\tau_{f,j}$	joint friction $\in \mathbb{R}^N$, with N DoF written in bold for joint friction vector $\boldsymbol{\tau_{f,j}} \in \mathbb{R}^N$, with N DoF
τ_m	reflected motor torque $\in \mathbb{R}$, with N DoF written in bold for motor torque vector $\boldsymbol{\tau_m} \in \mathbb{R}^N$, with N DoF subscript: d for desired
τ_r	rotor torque before gear transmission $\in \mathbb{R}^N$, with N DoF
z	combined gear box and transmission ratio $\in \mathbb{R}$

Joint Stiffness Computation

d	spring damping $\in \mathbb{R}$ subscript: i indicates spring number
F	spring force $\in \mathbb{R}$ subscript: p indicated pre-stretch force, i indicates joint
k	spring stiffness $\in \mathbb{R}$ subscript: i indicates spring number
l_p	pre-stretched spring displacement $\in \mathbb{R}$ second subscript: i indicates spring number
x	spring elongation $\in \mathbb{R}$ subscript: i indicates spring number

Motor Model

i_a	motor current $\in \mathbb{R}$
k_t	motor torque constant $\in \mathbb{R}$
k_v	motor speed constant $\in \mathbb{R}$
L_a	motor terminal inductance $\in \mathbb{R}$
R_a	motor terminal resistance $\in \mathbb{R}$
u_c	commanded motor voltage $\in \mathbb{R}$
u_{ind}	induced motor voltage $\in \mathbb{R}$

Observer

$\boldsymbol{K_I}$	positive diagonal observer gain $\in \mathbb{R}^{N \times N}$, with N DoF
L	reciprocal of observer time constant $\in \mathbb{R}$
r, $\dot{r}$	computed residual and time derivative from disturbance observer $\in \mathbb{R}$ written in bold for residual vector, e.g., $\boldsymbol{r} \in \mathbb{R}^N$, with N DoF
s	Laplace operator $\in \mathbb{R}$

External Forces and Torques

$\boldsymbol{F_{ext}}$	external end-effector force vector $\in \mathbb{R}^N$, with N DoF
τ_{ext}	external joint torque $\in \mathbb{R}$ written in bold for external joint torque vector $\boldsymbol{\tau_{ext}} \in \mathbb{R}^N$, with N DoF subscript: t indicates external torque threshold
$\hat{\tau}_{ext}$	external joint torque estimation $\in \mathbb{R}$ written in bold for external joint torque estimation vector $\hat{\boldsymbol{\tau}}_{\boldsymbol{ext}} \in \mathbb{R}^N$, with N DoF subscript: L and ML indicates the used observer (not set means L)

Errors

ϵ	general error term $\in \mathbb{R}$ written in bold error vector $\boldsymbol{\epsilon} \in \mathbb{R}^N$, with N DoF subscript: q, k_e, $init$, n_t, $tendon$, f for joint, joint stiffness, initialization, transmission, tendon, and friction error respectively
ϵ_{AVG}	average relative error $\in \mathbb{R}$
ϵ_{bss}	Cartesian error of basic state space controller $\in \mathbb{R}$
ϵ_{ess}	Cartesian error of extended state space controller $\in \mathbb{R}$
ϵ_{MAX}	maximum relative error $\in \mathbb{R}$
$\epsilon_q, \epsilon_{\dot{q}}, \epsilon_{\ddot{q}}$	position, velocity, and acceleration estimation error $\in \mathbb{R}$ subscript: indicates joint
ϵ_{RMS}	root mean square error $\in \mathbb{R}$

Velocity Estimation

The matrix dimensions for velocity estimation are denoted by L being the state dimension, M being the control input dimension, and O being measurement dimension.

$\boldsymbol{A}$	transition matrix $\in \mathbb{R}^{L \times L}$
α	velocity scaling factor $\in \mathbb{R}$
$\boldsymbol{B}$	control input to state relation matrix $\in \mathbb{R}^{L \times M}$
ΔR	update step size of measurement variance $\in \mathbb{R}$
Δ_p	encoder position resolution $\in \mathbb{R}$
Δ_v	encoder velocity resolution $\in \mathbb{R}$
ε	accuracy range for position estimation $\in \mathbb{R}$
f	frequency $\in \mathbb{R}$
$\boldsymbol{H}$	state to measurement relation matrix $\in \mathbb{R}^{O \times L}$
$\boldsymbol{K_k}$	Kalman gain $\in \mathbb{R}^{L \times O}$
$\mu_{\dot{q}}$, $\mu_{\ddot{q}}$	velocity and acceleration error weights for objective function
N	encoder ticks per rotation $\in \mathbb{R}$
n_n	update rule noise factor $\in \mathbb{R}$
ω	angular frequency $\in \mathbb{R}$
$\boldsymbol{P_k}$	error covariance matrix $\in \mathbb{R}^{L \times L}$
$\boldsymbol{P_k^-}$	estimation covariance matrix $\in \mathbb{R}^{L \times L}$

$\boldsymbol{Q}$	process noise covariance $\in \mathbb{R}^{L \times L}$
R	measurement noise variance $\in \mathbb{R}$ written in bold for measurement noise covariance matrix $\boldsymbol{R} \in \mathbb{R}^{L \times L}$ subscripts: v for velocity dependent, b for initial base value
$s_{\Delta R}$	scaling of update step size $\in \mathbb{R}$
s_v	velocity scaling factor $\in \mathbb{R}$
σ^2	system process variance $\in \mathbb{R}$
T	sample time period $\in \mathbb{R}$
$\boldsymbol{u}$	control input $\in \mathbb{R}^L$
v	measurement noise random variable $\in \mathbb{R}$
$\boldsymbol{w}$	process noise random variable $\in \mathbb{R}^L$
$\boldsymbol{x}$	state vector $\in \mathbb{R}^L$
$\hat{\boldsymbol{x}}_{\boldsymbol{k}}^{-}$	predicted state $\in \mathbb{R}^L$
$\hat{\boldsymbol{x}}_{\boldsymbol{k}}$	corrected state estimation $\in \mathbb{R}^L$
$\boldsymbol{z}$	measurement $\in \mathbb{R}^O$

Contact Modeling

b_c	contact spring damping coefficient $\in \mathbb{R}$
F_c	contact force $\in \mathbb{R}$
k_c	contact spring stiffness coefficient $\in \mathbb{R}$
x_p, $\dot{x}_p$	penetration depth and velocity $\in \mathbb{R}$

List of Abbreviations

AKF	Adaptive Kalman Filter
AR	Augmented Reality
Aramid	Aromatic Polyamide
Cobot	Collaborative Robot
DoF	Degrees of Freedom
EMF	Electromotive Force
GUI	Graphical User Interface
HIC	Head Injury Criterion
HMPE	High Modulus Polyethylene
HRC	Human-Robot Collaboration
HRI	Human-Robot Interaction
LCP	Liquid Crystal Polymer
MTI	Materials Testing Institute
PBO	Polybenzoxazole
pHRI	physical Human-Robot Interaction
SEA	Series Elastic Actuators
TU	Technische Universität (Technical University)

1 Introduction

1.1 Motivation

More than half a century has passed since the industrial automation was started by the application of robots like the Unimate. From this time on, robotic systems have evolved and can now be found in many aspects of life as cleaning robots, lawn mowers, care robots for older adults, surgery robots, rescue robots, different kinds of humanoid robots and so on. But also in the industrial environment, more robot handled tasks can be observed for example as mobile picking robots for storage logistics or intelligent assist devices. It can be noticed that the overall trend brings the robots closer to humans. This trend seems to be reasonable because robots, as artificial machines, can repetitively perform hard or high precision tasks to support humans. Further, the increased computing power and communication possibilities via network enable coordinating tasks between different embedded systems and solving them in an intelligent way creating Cyber-Physical Systems. This currently leads to the next industrial revolution (industry 4.0) with Cyber-Physical-Production Systems realizing smart factories.

The robotic evolution shows that the capabilities of robotic systems have reached the point where they are not restricted anymore to statically programmed motions but can solve complex tasks autonomously. This enables the development of a robotic co-worker that performs tasks in collaboration with humans during manufacturing processes without fences in the same workspace. Here, the automation process can benefit from both, the human's dexterity and process knowledge and additionally from the robot's tireless performance with repeatable precision. Safety of the human work mate regarding, for example, undesired collisions or clamping and, thus, safe physical human-robot interaction (pHRI) is crucial in this scenario.

A host of design approaches can be considered when creating a robotic system intended for safe human-robot interaction. Besides sensor driven approaches (e.g., joint torque sensors, proximity sensors, or camera based workspace observation) also mechanical approaches (e.g., cushioning, joint elasticities, and lightweight structures) can be used to benefit safe collaboration. The introduction of even small joint elasticities in the drive train decouples the motor and link inertia resulting in a reduced transient collision force that is mainly determined by the link inertia [50]. A typical approach to further reduce the transferred kinetic energy during a collision is to downscale industrial robot arms. As long as its motors are fitted inside the joints or links, they have to be downscaled as well. This limits the possible effective mass reduction according to the desired reach and payload.

In addition to downscaling the robot to a human-like size and payload with joint elasticities, tendons can be introduced into the drive train. This enables shifting the motors away from the joints towards the base, further reducing the effective mass and allowing higher velocities at same safety level, creating a different class of lightweight robots compared to the approaches

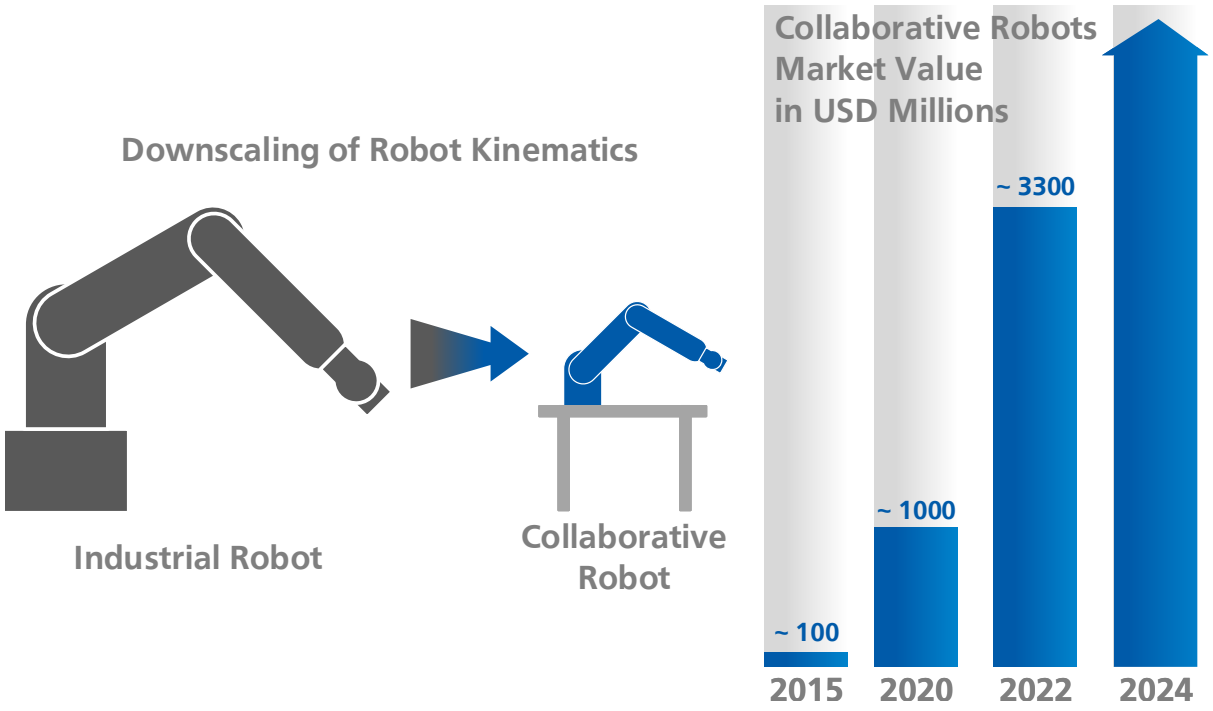

Figure 1.1.: Downscaling rigid joint robots as a typical design approach for collaborative robots. On the right, the market trend analysis of *ABI Research*, forecasting a collaborative robot market value of USD 1 Billion in 2020, which further increases to USD 3.3 Billion in 2022 according to *Markets and Marktes* forecast.

above. This actuation principle makes it possible to realize an intrinsically safe robot that simultaneously allows end-effector velocities suitable for a manufacturing process.

The significant gain in the importance of safe pHRI and robots working in the vicinity of humans in the past years can be seen from the growing range of robots on the market designed for such tasks. Some examples of these robots are the *LBR iiwa* [14], *Franka Emika* [40], *UR3* [132], and *Yumi* [1], which are following the downscaling design approach with joint elasticities introduced only by the used gears and torque sensors as illustrated in Figure 1.1. The growing trend in collaborative robotics is highlighted by different market analysis that predicts an increasing number of used collaborative robots in industrial automation, forecasting a market value of USD 1 Billion in 2020 [2] and USD 3.3 Billion in 2022 [98] (Figure 1.1 right). In terms of safety, an ultra lightweight tendon driven series elastic robot arm seems to be the right answer to these market needs, but only if it provides dependable performance.

Parts of this section have been presented and published in [78] and [79].

1.2 Contribution

Incorporating high elasticities in combination with tendons in the drive train to actuate a robot arm introduces some inherent uncertainties regarding the dependability of such a system. This mainly results from variance in the drive train over the span of its lifetime and system model parameter errors. In order to make the actuation concept dependably usable, the uncertainty

sources have to be identified, their influence on performance investigated and compensated if possible. In this regard, ultra lightweight tendon driven series elastic robots are considered in this thesis. Due to restrictions in weight and size, motor and joint position encoders are assumed as the only available sensors during the dependability evaluation.

As already stated, elasticities in the drive train decouple the motor and link inertia, mitigating the forces resulting from the transferred energy during a collision or contact. This is one key to enable productive and safe human-robot collaboration without the need for specific motion restrictions. The safety requirements for industrial robots has been complemented by the ISO/TS 15066 [68] regarding collaborative robots. The risk assessment mentioned here, for the case of free and transient contacts, regards the human's biomechanical limits to determine the admissible end-effector velocities. According to this technical specification, a tendon driven joint elastic robot and a small-sized, stiff robot are compared to get an insight of the safety capabilities of their robot class. Since the effective mass estimation used in ISO/TS 15066 is very simplified, an effective mass computation scheme is proposed during the investigation that regards the center of mass relocation for tendon driven robots. In Addition to the energy transfer, the effect of high joint compliance is investigated during a collision experiment, showing the immediate reaction to surface contacts especially relevant for clamping situations.

Besides safety, the intrinsic compliant behavior is beneficial for solving contact tasks like peg-in-hole or screwing, because position inaccuracies are compensated through the flexible structure without causing damages to the handled part or environment, as it is the case for rigid structures (without additional sensing). But high joint elasticities and low damping can lead to undesired oscillations or swinging motions, which affect the position accuracy of such systems. In order to effectively damp the controlled motion and also for model-based computations (e.g., observer approaches, dynamics), an accurate velocity estimation is essential.

Because of the lightweight and small size structure in combination with highly flexible joints, the range of possible velocities and oscillations during motion can be very large. Moreover, the restricted space in the lightweight and downscaled design allows only low-resolution sensors for joint position sensing. This requires the velocity estimation approach, based on position encoder data only, to cover a large bandwidth based on a coarse discrete position signal. Kalman filter approaches already showed accurate performance in position based velocity estimation but within a small bandwidth. This limited bandwidth correlates with the filter's measurement variance that should be updated appropriately, which requires knowledge about their characteristics. In order to identify the optimal measurement variance in the particular case, a new optimization-based analysis is proposed in this thesis that reveals the velocity and frequency dependent measurement variance characteristics. On the basis of the obtained observations, a novel measurement variance update rule is determined that enables the filter to cover a broader bandwidth than previous approaches. The proposed filter is compared to a state-of-the-art filter in simulation experiments and robot experiments.

In biologically inspired mechanical structures, tendons are used to transmit forces along a kinematic chain. These tendons must satisfy high robustness requirements by simultaneously allowing small pulley radii. Cables or belts often cannot meet these requirements here, especially if the tendons have to be wired through multiple joints. The evolution of synthetic fibers in the past decades enabled the creation of ropes with enormous tensile forces and high breaking force to weight ratio, well suitable to be used in ultra lightweight robots.

Typically, only a minimal amount of information about the ropes are provided by the manufacturer, like the diameter, fiber type, breaking force, and some qualitative fiber bending curve plots. Based on these characteristics, it is not evident if a specific rope is suitable to be used as a reliable force transmission component or not. In particular, the irretrievable rope elongation characteristic (creep) is a relevant factor because it introduces backlash in the drive train. Thus, further research is required to investigate whether a rope is suitable to be used as a reliable component of a drive train. For this purpose new comparative creep experiments regarding different fiber materials, manufacturers, and diameters have been performed. Further, the influence of the number of pulleys that stress a rope made from commonly used fiber has been experimentally evaluated. The general observations about the rope characteristics support the rope selection during the system design process and provide indications about the long-term behavior. In order to monitor this, an observer approach is proposed that omits the need for joint torque measurements and enables elongation detection in tendon driven kinematic chains even under model inaccuracies, which has been shown in simulation and robot experiments.

It is expected from a robotic arm to precisely execute desired motions and perform a certain task, each time producing the same outcome. But the identified drive train model parameters for tendon driven joint elastic robots can be erroneous because of inaccurate parameters, unmodeled effects or variations over time, for example, because of wear or load dependent friction. This profoundly influences the control performance and, thus, the reliability of the system. State-of-the-art control approaches for joint elastic robot arms require an accurate joint torque measurement, drive train model, and rigid body dynamics model. Torque sensors with a suitable range are heavy and large and do not fit into the lightweight actuation. With the available erroneous model-based joint torque estimation, which leads to inaccurate load dependent friction models, these approaches perform unsatisfactorily.

The novel control approach presented in this thesis addresses these challenges to realize accurate trajectory tracking performance. To reduce the model dependency, the performance of a friction observer under joint torque estimation errors has been analyzed. Based on the gained knowledge a state space controller is proposed that is able to compensate drive train and load dynamics model inaccuracies. In particular, it integrates a friction observer without the need for explicit joint torque measurements, is robust against inaccurate initialization of the relative motor position encoder, and compensates for changes in the robot dynamics caused by gripping or releasing objects. Since the resulting controller eliminates steady-state control errors, contacts that inhibit this compensation would lead to high control torques. To avoid this effect, the proposed controller contains a contact mode based on external torque observation that limits the forces exerted on the environment, enabling contact tasks. This newly introduced control approach has been evaluated in simulation and robot experiments.

For successful human-robot collaboration, the robot should be able to sense interactions with the environment. And in the inverse direction, the human workmate should be able to simply show the robot the needed actions and understand the robot's execution state and intended motion to solve a task jointly. Detecting physical interactions with the environment can be achieved by disturbance observers, which are only based on internal data.

The accuracy limitations of disturbance detection approaches, in dependence of the possible drive train uncertainties caused by model inaccuracies or wear effects, is investigated and presented in this thesis. Besides the theoretical consideration, the disturbance torque estimations

are evaluated in simulation and robot experiments, revealing the capabilities of tendon driven joint elastic robots regarding external torque estimations. Furthermore, an interaction controller that deals with these limitations is proposed for hand guided teach-in by demonstration to enable the user to teach the needed robot motion without high effort. To prevent misunderstandings and enable a smooth collaboration, the human should always be kept informed about the robot's execution state and have an impression of the robot's intention. For this purpose, a preliminary user study is conducted that investigates the influence of state visualizations on the user's situation awareness. Additionally, the user should be able to assess the robot's health state, which increases the trust in collaboration. Regarding this, the possible actuation principle related wear estimation metrics are introduced and discussed, that can be used for degradation monitoring and maintenance scheduling if required.

1.3 Outline

The structure of this thesis is inspired by the development methodology for mechatronic systems, that consists of defining the requirements, and establishing a system design that describes the central solution concept on which basis further detailed designs are concretized. The individual results are finally integrated into the whole system, and the properties continually checked on the basis of the specified requirements. This structure in consideration with the dependability of ultra lightweight tendon driven series elastic robots is depicted in Figure 1.2 and described in the following paragraphs.

In **Chapter 2** the requirements regarding human-robot collaboration including the relevant state of research are presented. Starting with an overview about safety, modeling and control, as well as the definition of dependability, the considered system is differentiated to comparable systems designed for human-robot collaboration.

The concrete design tasks can be divided into two domains concerning the basic functionality (**Chapter 3** - **Chapter 6**) and the human-robot collaboration capabilities (**Chapter 7**).

Regarding the specific robot design, **Chapter 3** introduces the used robotic evaluation hardware, describes the challenges that have to be considered for a dependable system, and compares the safety capabilities of tendon driven series elastic robots with common collaborative robots using recent safety considerations. **Chapter 4** proposes a velocity estimation approach for highly joint elastic robots suitable for the control and observer computations. New insights in synthetic fiber rope elongation are presented in **Chapter 5** to reveal their characteristics and enable wear estimation. **Chapter 6** presents a novel trajectory tracking control approach that is able to compensate for the system specific drive train uncertainties. Finally, the human-robot collaboration capabilities are investigated in **Chapter 7** regarding contact forces, situation awareness and maintenance.

The system integration of the presented solutions and approaches is done continuously and evaluated via experiments presented in each chapter. **Chapter 8** concludes and discusses the results of this thesis.

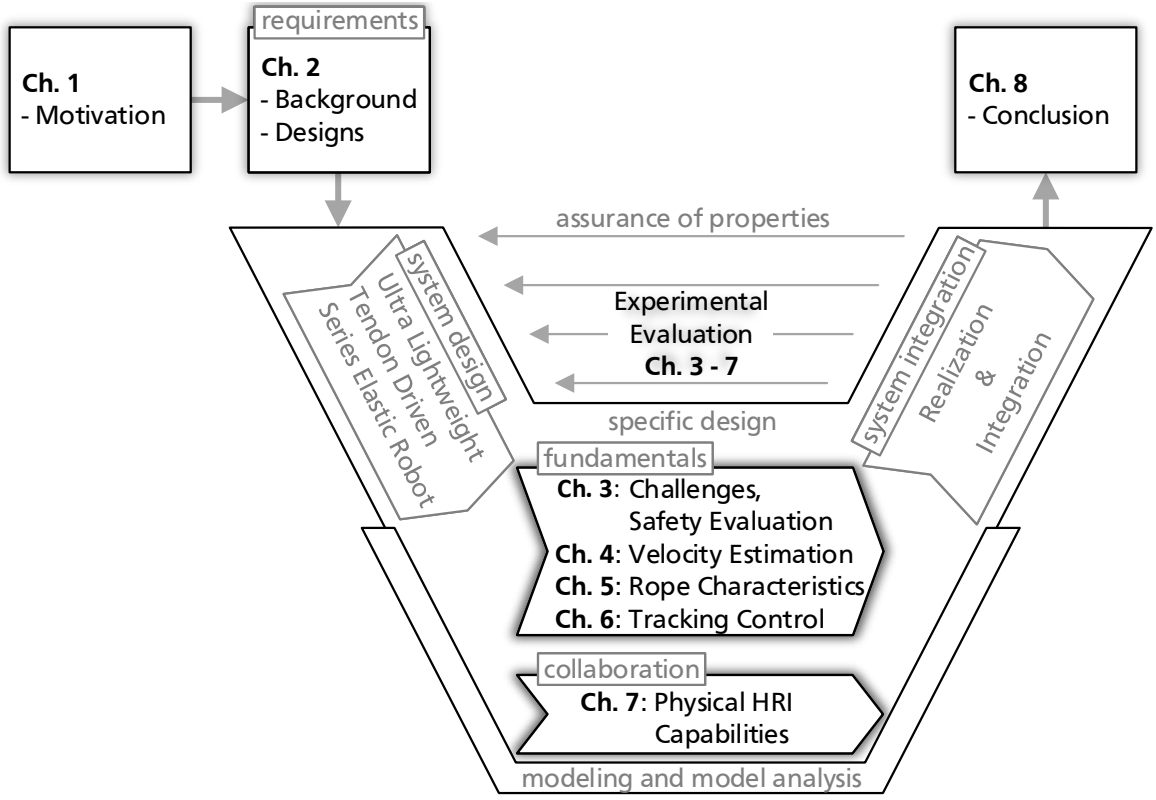

Figure 1.2.: Visualization of chapter structure inspired by VDI 2206 [135].

2 Background and State of Research

Generally, any kind of robot that collaborates with a human being could be named cobot, but typically an industrial robot that physically interacts with a person is meant as defined in [20]. The possibility to remove fences from robots in the industrial environment creates a new kind of automation. Now, yet unsolved tasks can be handled by combining the endurance and precision of a robot with the dexterity of a human. Besides the evolution of possible automation solutions, also the view of the robot's execution changes. With traditional industrial robots, mainly autonomous performed tasks were programmed by an expert with a high knowledge of the robot's properties. In order to realize a collaboration, it is now necessary to program the whole automation process that has to be performed rather than a static, repetitive movement. This approach provides the information that enables the robot to react on changes in its environment and still to perform as required.

The successful human-robot collaboration is considered in many fields of applications where humans and robots interact, but the industrial automation already provides standards that define the scope of collaboration as well as safety requirements. This is the reason why the industrial branch is investigated in this thesis, although many standards and developments can also be transferred to other fields of robotics (e.g., service robotics). This chapter gives an overview of the research efforts made for collaborative robots. This includes safety and basics known from classical robotic research. Further, the concept of dependability as well as robots designed for pHRI are introduced. This finally leads to the concept of the investigated ultra lightweight tendon driven series elastic actuation.

2.1 Aspects Related to Human-Robot Collaboration

Bringing humans and robots together in the same workspace to accomplish a common task, introduced new challenges to industrial robotic arms. First of all, human safety has to be ensured during the task execution. This also results in need of adaptive motion correction to avoid collisions with a modified environment by or with the human itself. Further, changes in a time-varying environment have to be recognized, which probably requires additional internal or external sensors, and strategies available to guarantee successful process execution. This and other challenges have to be regarded on different abstraction layers to realize human-robot collaboration. In Figure 2.1, a general layer structure is introduced to describe the abstraction layers including their responsibilities and research fields.

The bottom layer represents the specific robot mechatronic parts that perform the motion and sense the internal state of the robot. The hardware communication has to be made accessible and interpreted in a way that it can be used in the layers above, as for example to receive the joint position, joint torque or send motor control signals. This objective is part of the hardware abstraction. The next level contains all components that are necessary to execute a specific

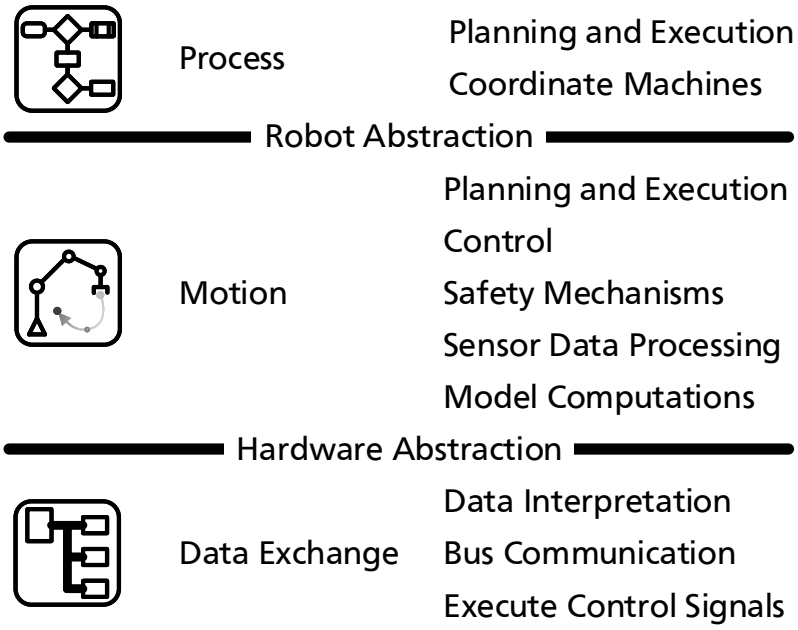

Figure 2.1.: Conceptual overview of abstraction layers including responsibilities and field of research incorporated with human-robot collaboration.

motion with all related computations and essential security mechanisms. The last layer abstracts from a specific robot [1] to plan a task or process that has to be performed. This also includes process execution, dynamic replanning, and special behavior according to the performed task. The uncertainties of the considered tendon driven joint elastic actuation mainly affect the layers below robot abstraction. An overview of the main issues and superposition for pHRI regarding the anthropic domain is presented in [32].

2.1.1 Safe Physical Human-Robot Interaction

As Isaac Asimov already said, "A robot may not injure a human being or, through inaction, allow a human being to come to harm". This well known first law from its science fiction novel "I, Robot" plays a fundamental role if robots and humans should work together. Physical human-robot interaction can occur in two different ways. Firstly, as part of the collaboration task with the human (e.g., Teach-In, part delivery or assembly), secondly, as undesired contact or collision with the workmate or environment. To ensure safety in the industrial automation environment using robots, the international standards [66] and [67] for robots, robotic systems, and their integration evolved since 2005. The defined safety requirements, protective measures, and their validation aims, amongst others, to reduce the worker's injury risk as far as possible.

Using the robot in collaboration has to fulfill at least one of the following methods, if the worker enters the collaborative work space.

a) *Safety-Rated Monitored Stop*: The robot stops and stays in rest.

[1] Changes to available sensors or degrees of freedom have to be regarded.

b) *Hand Guiding*: The robot moves according to the direct input of the operator through a guiding device with a motion below a maximum permissible speed.

c) *Speed and Separation Monitoring*: The robot moves only if it is not closer to the operator than a certain separation distance, and the motion speed is below the maximum permissible speed.

d) *Power and Force Limiting*: The robot is inherently safe or has a safety-related control system, to keep the energy and force below a certain limit during a physical contact situation.

One important change emerged in the year 2016 with the release of the technical specification [68]. Previously, the speed, power, and force limits were fixed to 250 mm/s, 80 W and 150 N respectively in collaborative operation. These limits were not suitable for certain applications or the upcoming collaborative robots. To overcome this, human body part specific biomechanical limits of permissible forces and pressures have been determined. Using these limits and the guidelines in the technical specification allow computing a more accurate estimate of the limits for a specific robot during risk assessment. Additionally, the safety-related control parts or safety operations have to comply with *Performance Level*[2] PL d with category 3 or *Safety Integrity Level*[3] 2.

Typically, force/torque sensors[4] are used in rigid robots to detect the acting torques and forces at the end-effector flange to realize contact applications. This has the drawback that contacts along the kinematic chain cannot be detected. Thus, this approach is not suitable for safe human-robot interaction. To overcome this, a force/torque sensor can be placed in the base of the rigid structure[5]. The latter solution has a certain delay and inaccuracies since the force has to traverse the whole structure before it is observed.

Ensuring safety for humans in the proximity of a robot requires to detect desired or undesired contacts on each link quickly. A fault detection and isolation (FDI) scheme has been proposed in [26] that computes a residual based on the generalized momentum to detect faults caused by collisions or contacts. The used observer design does not require acceleration or force measurements and enables to isolate the robot link where a disturbance occurred. It is also suitable for robots with elastic joints. In [27], [29], and [48] the FDI technique has been used for control purpose to realize different collision reaction strategies and evaluating the resulting collision forces. In the case of elastic joint robots, joint torque measurements have been available.

In order to estimate the risk of danger, it is necessary to determine when a collision with a specific robot starts to be harmful for humans. Here, one has to distinguish between free and constraint contacts. Fundamental collision tests with a wide range of classical industrial robots can be found in [140], [50], [51], [52], [49] and [53]. The major results are summarized in the rest of this paragraph. According to the test results, the typically used *Head Injury Criterion* (HIC) from automobile crash testing, cannot be transferred to the field of robotics. All tested robots (nominal payload 3 - 500 kg) produced a very low injury level according to the HIC, which means that blunt impacts without clamping are unlikely to be life-threatening. Thus,

[2] Performance Level and categories are defined in standard *ISO 13849-1:2006*

[3] Safety Integrity Level with hardware requirements are defined in standard *IEC 62061-1:2005*

[4] For example, the FT 150 or FT 300 sensor from ROBOTIQ (http://robotiq.com/products/robotics-force-torque-sensor/)

[5] This has been presented during the Automatica fair 2016 at KUKA with the KR Agilus Cobotics Concept.

other injury measures, e.g., maximum permissible forces or compressions, seems to be more suitable. Further, it is shown that the injury potential saturates for free collisions at increasing robot mass. In contrast, at constraint impacts, the robot's mass and thus its kinetic energy is crucial for human safety since the human body is only able to absorb a limited amount of kinetic energy without suffering from severe injuries. The collision impact characteristics also showed that even small joint elasticities decouple the motor and link inertia. In this case, the collision force peak is determined by the link inertia, which is transferred in 6 - 10 ms. To increase safety, it has been evaluated that cushioning can reduce the injury risk and that the above-mentioned collision detection scheme is beneficial even at collision with a sharp tool on soft-tissues.

2.1.2 Concept of Dependability

Besides safety in human-robot interaction, the concept of dependability is important since it enables the human operator or workmate to trust the robotic system, especially in the considered complex and semi-structured environment. Dependability can be defined according to [9] as:

> *The ability of a system to avoid service failures that are more frequent or more severe than is acceptable.*

Alternative definitions can be found in [9] and [63]. According to [9] and [81] dependability is an integrated concept that encompasses the attributes

- *Availability*: The readiness for correct service.
- *Reliability*: The continuity of correct service.
- *Safety*: The absence of catastrophic consequences on the user(s) and the environment.
- *Integrity*: The absence of improper system alterations.
- *Maintainability*: The ability to undergo modifications and repairs.

These requirements have some relationships that will be described below as presented in [3] and are visualized in Figure 2.2. In the context of pHRI *safety* can be rephrased as "absence of injury to humans in the robot's environment". Further, a robot should always be ready to carry out its intended tasks, which is encapsulated in the requirement *availability* and *reliability*. Robot *integrity* is a prerequisite for *safety*, *reliability* and *availability*. Corrective and preventive maintenance, in turn, is necessary to achieve *availability*.

The term "service failure" in the definition of dependability means that at least one system state deviates from the correct service state. This deviation is called *error*. Where the cause of an error is called a *fault*. To ensure the dependability attributes to an acceptable level, it is useful to define the possible *faults* that can occur. These *faults* can roughly be classified as *physical* (or internal), *interaction* (or external) and *development faults*. The means to attain dependability can be grouped in four major categories *fault prevention*, *fault tolerance*, *fault removal*, and *fault forecasting*.

As already mentioned, several safety mechanisms exist in the context of physical human-robot interaction. These mechanisms are suitable to protect both, the human and the robot which supports the robot's *integrity*. Further, *safety* and *maintainability* is a relevant part of the robot development phase, which is typically completed if the robot is used. Thus, this work focuses on the dependability attribute of *reliability*, which enhances the *availability* of the robot.

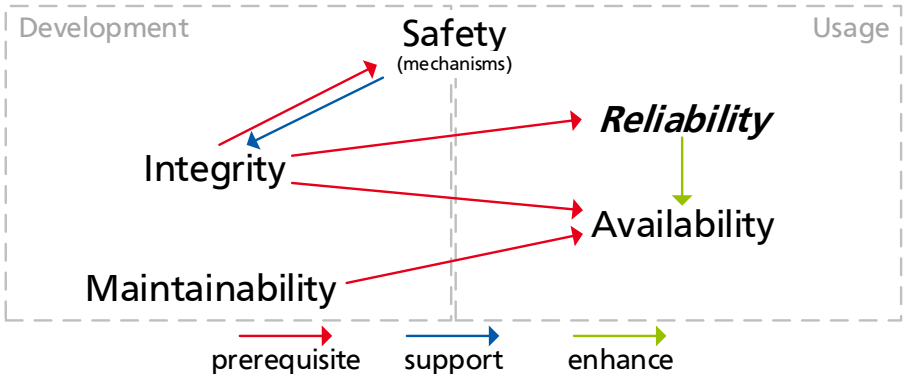

Figure 2.2.: Relationship visualization of the dependability attributes inspired by the textual description in [3].

According to [63] reliability can be defined as:

> *Ability of a system to perform a required function under stated conditions, within a given scope, during a given period of time.*

An important mean to attain reliability in a system with components that properties significantly change over time is *fault tolerance*, which aims for failure avoidance. The technique of *fault tolerance* consists of error detection and system recovery, incorporating error handling (eliminates errors from the system state) and fault handling (prevents faults from being activated again). Typically, fault handling is followed by corrective maintenance to remove the isolated faults (fault handling). A literature review regarding *fault tolerance* is given in [21] and has been investigated for robotic systems for example in [136], [57], [56], [129], and [106]. In the context of safe human-robot interaction, a dependability analysis of antagonistic variable stiffness actuation is presented in [36], and a feature extraction method for fault diagnosis of series elastic actuators in [112], focusing on motor, stiffness and position sensor faults.

In a robotic system, various error sources regarding the particular actuation exist, with each requiring appropriate approaches to obtain reliability. This thesis focuses on the specific challenges and error sources of ultra lightweight tendon driven series elastic actuation as presented in Section 3.2.

2.2 Robot Arms for Human-Robot Collaboration

Creating a robotic arm that fits the needs of human-robot collaboration is a creative process that is highly influenced by the aimed target application. Further, the robot's design depends on

various requirements like the safety concept, targeted price, payload, and reach, or amount and kind of sensors. In this section, an overview of robots designed for human-robot collaboration is presented. Here, two different design approaches are distinguished.

2.2.1 Downscaling the Robot's Kinematic Structure

The trend in the past years to gain human-robot collaboration in the industrial automation environment has been mainly to downscale the mechanical structure of classical industrial robots. The resulting reduced robot mass and velocity also decreases the kinetic energy and, thus, increases human safety. The robotics and mechatronics institute of the German Aerospace Center (DLR) has been one of the pioneers in this research field. The development efforts resulted in the sophisticated modular robot *LWRIII*, with redundant kinematics and highly integrated electronics equipped with joint torque and position sensing [58], [59]. In cooperation with the robot manufacturer *KUKA* this robot has been transformed into a marketable product today known as *KUKA LBR iiwa* [14]. Using a quite similar mechatronic design, but with the purpose to be an out of the box solution for everybody, the robot *Franka Emika* has been developed by *KBee AG* and presented on the *Hannover Messe* in April 2016 [40].

Parallel to the development progress at *DLR* and *KUKA*, three students from the University of Southern Denmark in Odense came up with the idea of creating a light robot that is easy to install and program [132]. They observed that heavy, expensive and unwieldy robots dominated robotics and that there was a market for a more user-friendly option. The funded company *Universal Robots* (UR) was one of the first that opened the automation market for robots that can be programmed and integrated by non-expert user with the aim of safe human-robot collaboration and a fast return on investment. This makes them also interesting for small and medium enterprises. In 2009, the first robots were sold, and since 2012 the annual sales have increased by an average of approximately 75%, which emphasizes the need for this kind of robots. In the past years many, more or less sophisticated *UR* robot clones (e.g., *AUBO-I5* from *AUBO robotics*) appeared on the market.

With the aim to create a complete assembly and automation robot that works safely without cages, *Rethink Robotics* (founded by Rodney Brooks) started to develop the two arm robot *Baxter*, equipped with a novel human-machine interface, cameras, and grippers. This fast by non-engineers trainable robot can be quickly moved from job to job without integrator and is affordable for companies of all sizes [119]. With the two arm robot *YuMi*, the manufacturer *ABB* also designed a robot for this purpose, but in contrast in a smaller scale and with less direct human-machine interface [1]. In contrast to these solutions *BOSCH* developed the optionally mobile solution *APAS assistant* by equipping an industrial robot (*Fanuc*) with a sensor skin and communication interfaces to realize safety and enable fast integration in existing manufacturing environments [120].

An overview of the current major collaborative robots is given in Table 2.1. In summary, one can observe that the robots maximum reach and payload is in a wide rage range of 0.5kg - 14kg and 500mm - 1300mm respectively. Besides these robots, some manufacturers presented solutions to make existing industrial robots ready for human-robot collaboration (e.g., Fanuc CR-35iA) by introducing appropriate soft covers and sensors.

Table 2.1.: Overview of the major cobots currently available on the market and the used evaluation platform. The technical specifications are taken form [1, 8, 120, 39, 40, 75, 80, 95, 119, 132].

Manufacturer	Robot	Degree of Freedom	Weight	Reach	Payload
ABB	YuMi	2x 7	38.0 kg	500 mm	0.5 kg
Automata	Eva	6	n/a	600 mm	0.75 kg
BOSCH	APAS, with Fanuc LR Mate	6	27.0 kg	911 mm	7.0 kg
F&P Personal Robotics	P-Rob 2R	6	20.0 kg	775 mm	3.0 kg
KBee	Franka Emika	7	18.5 kg	800 mm	3.0 kg
KINOVA	JACO^2 MICO^2	6	4.4 kg 4.6 kg	900 mm 700 mm	2.2 kg 1.5 kg
KUKA	LBR iiwa 7 LBR iiwa 14	7	22 kg 30 kg	800 mm 820 mm	7 kg 14 kg
MABI	Speedy 6 Speedy 12	6	28 kg 35 kg	800 mm 1250 mm	6 kg 12 kg
Rethink Robotics	Baxter Sawyer	2x 7 7	75 kg 19 kg	1210 mm 1260 mm	2.2 kg 4 kg
Universal Robotis	UR3 UR5 UR10	6	11 kg 18.4 kg 28.9 kg	500 mm 850 mm 1300 mm	3 kg 5 kg 10kg
Bionic Robotics	BioRob	5	7.8 kg	760 mm	0.5 kg

2.2.2 Tendon Driven and Biological Inspired Robotic Arms

As mentioned in [78], reducing the robot's effective mass by downscaling but still keeping the motors placed in the joints is limited according to the desired reach and payload of the robot. Whereas, introducing tendons in the robot's mechanical design enables to shift the motors away from the joints towards the base, which results in a further reduced effective mass and determines a different class of lightweight robots. This concept is well known from the biomechanical musculoskeletal structure of a human arm, where the muscle (actuator) is not necessarily placed at the joint that is moved.

Realizations of this kind of kinematic design can be found in different types. The German company *IGUS* developed the modular tendon driven robot *robolink W*. Here, all motors are placed in the base and each joint consists of two degrees of freedom that can be combined to a robot with at most six degrees of freedom [62]. Since the materials used for the *robolink W* are plastic for the joints and aluminum for the links, an ultra light weight robot arm has been created. A comparable robot to the *robolink W* has been developed by the start-up company

carbon robotics named *KATIA*. Analog to the *robolink W*, all motors are placed in the base but with the links made of carbon. Further, the kinematic chain, as well as the housing, is more like those of classical industrial robots. Concerning safety, the robot is equipped with capacitive sensors to detect humans in the robot's vicinity. A slightly different actuation approach is used at the *WAM Arm* developed by *Barrett Technology*. Here, the robot is driven by gearless cable differential drives and can be optionally equipped with a force/torque sensor at the wrist [121], [10].

According to the concept for intrinsic safety of DeSanit, Siciliano, DeLuca, and Bicci in [32], the reduced mass of the moving parts resulting from motor relocation using tendons, to lower the transferred impact energy in the collision case, can be supplemented by a compliant transmission. This also follows the example of the human's biomechanical structure. One way to realize mechanical compliance is to integrate springs with appropriate or perhaps adjustable stiffness into the drive train. This decouples the motor inertias mechanically from those of the links but additionally is useful against contact situation to mitigate damages or during peg-in-hole tasks to compensate position inaccuracies. The *BioRob* arm [86] used in this work as evaluation platform, has been developed at the Simulation, Systems Optimization and Robotics Group (SIM) of the Technische Universität (TU) Darmstadt and further developed at the spin-off company *Bionic Robotics GmbH* in cooperation with SIM. The *BioRob* arm actuation concept contains tendons as well as springs in the drive train, well suited regarding the safety requirements for pHRI.

2.3 Modeling and Control of Elastic Joint Robots

Robots with elastic joints, typically introduced by small elasticities in the components of the drive train, have been investigated in the past decades. The basic results regarding modeling and control are summarized in this section, which are relevant for the considered actuation principle in this thesis.

2.3.1 Modeling of Elastic Joint Robots

Dynamics modeling

The incorporation of elastic joints in the dynamics model of a rigid serial robot chain is summarized in [30]. One of the most important results is the simplified dynamics model that has been derived by [127] under the assumptions

- **(A1)** The actuators' masses are rotationally symmetric and their center of masses are located on the rotation axes.
- **(A2)** The angular velocity of the rotors is due only to their own spinning instead of their own together with the link velocity.

Using these assumptions, the link and motor equations of a serial robot with N joints can be expressed with two equations only coupled by a compliant transmission,

$$\boldsymbol{I_m}\ddot{\boldsymbol{\theta}} + \boldsymbol{\tau_{el}} = \boldsymbol{\tau_m} \tag{2.1}$$

$$\boldsymbol{M}(\boldsymbol{q})\ddot{\boldsymbol{q}} + \boldsymbol{C}(\boldsymbol{q},\dot{\boldsymbol{q}})\dot{\boldsymbol{q}} + \boldsymbol{g}(\boldsymbol{q}) = \boldsymbol{\tau_{el}} \tag{2.2}$$

$$\boldsymbol{K}(\boldsymbol{\theta} - \boldsymbol{q}) = \boldsymbol{\tau_{el}} \tag{2.3}$$

Here, the elastic transmission elements are modeled as a linear spring and dissipative terms as friction or damping are omitted. The equations contain the joint positions $\boldsymbol{q} \in \mathbb{R}^N$, its time derivatives $\dot{\boldsymbol{q}}$ and $\ddot{\boldsymbol{q}}$, the motor position $\boldsymbol{\theta} \in \mathbb{R}^N$ and acceleration $\ddot{\boldsymbol{\theta}}$. The motor dynamics equation (2.1) contains the diagonal motor inertia matrix $\boldsymbol{I_m} \in \mathbb{R}^{N\times N}$, the elastic transmission torque $\boldsymbol{\tau_{el}} \in \mathbb{R}^N$, and the motor torque $\boldsymbol{\tau_m} \in \mathbb{R}^N$. The rigid robot dynamics equation (2.2) consists of the mass matrix $\boldsymbol{M}(\boldsymbol{q}) \in \mathbb{R}^{N\times N}$, the matrix $\boldsymbol{C}(\boldsymbol{q},\dot{\boldsymbol{q}}) \in \mathbb{R}^{N\times N}$ of the centrifugal and Coriolis terms and the gravity torque vector $\boldsymbol{g}(\boldsymbol{q}) \in \mathbb{R}^N$ coupled with the elastic transmission $\boldsymbol{\tau_{el}} \in \mathbb{R}^N$. The elastic coupling (2.3) is represented by a linear spring model with the diagonal joint stiffness matrix $\boldsymbol{K} = \mathrm{diag}(k_{e,1}, ..., k_{e,N}) \in \mathbb{R}^{N\times N}$.

Inverse Dynamics

In contrast to rigid robotic systems, the elasticities have to be regarded to compute the desired motor torque for a given joint trajectory. The desired motor positions according to the desired joint positions can be computed using the elastic transmission model (2.3)

$$\boldsymbol{\theta} = \boldsymbol{q} + \boldsymbol{K}^{-1} \cdot \boldsymbol{\tau_{el}}, \tag{2.4}$$

where $\boldsymbol{\tau}_{el}$ is given by the rigid dynamics equation (2.2). The computation of the desired motor torque for a desired joint motion $q_d(t), t \in [0, T]$ has been proposed in [28]. Differentiating (2.4) twice results in the desired motor acceleration

$$\boldsymbol{\theta_d} = \boldsymbol{q_d} + \boldsymbol{K}^{-1} \cdot (\boldsymbol{M}(\boldsymbol{q_d})\ddot{\boldsymbol{q}}_d + \boldsymbol{c}(\boldsymbol{q_d},\dot{\boldsymbol{q}}_d) + \boldsymbol{g}(\boldsymbol{q_d})) \tag{2.5}$$

$$\ddot{\boldsymbol{\theta}}_d = \ddot{\boldsymbol{q}}_d + \boldsymbol{K}^{-1} \cdot \Big(\boldsymbol{M}(\boldsymbol{q_d})\boldsymbol{q}_d^{[4]} + 2\dot{\boldsymbol{M}}(\boldsymbol{q_d})\boldsymbol{q}_d^{[3]} + \ddot{\boldsymbol{M}}(\boldsymbol{q_d})\ddot{\boldsymbol{q}}_d + \ddot{\boldsymbol{c}}(\boldsymbol{q_d},\dot{\boldsymbol{q}}_d) + \ddot{\boldsymbol{g}}(\boldsymbol{q_d})\Big), \tag{2.6}$$

where $\boldsymbol{y}^{[i]} = d^i\boldsymbol{x}/dt^i$ denotes the i-th derivative, and $\boldsymbol{c}(\boldsymbol{q_d},\dot{\boldsymbol{q}}_d)$ is the resulting vector of the multiplication $\boldsymbol{C}(\boldsymbol{q_d},\dot{\boldsymbol{q}}_d)\dot{\boldsymbol{q}}_d$.

With equation (2.6), (2.1) and (2.2) the needed motor torque is obtained

$$\boldsymbol{\tau_{m,d}} = \boldsymbol{I_m}\ddot{\boldsymbol{\theta}}_d + \boldsymbol{M}(\boldsymbol{q_d})\ddot{\boldsymbol{q}}_d + \boldsymbol{C}(\boldsymbol{q_d},\dot{\boldsymbol{q}}_d)\dot{\boldsymbol{q}}_d + \boldsymbol{g}(\boldsymbol{q_d}), \tag{2.7}$$

where the desired trajectory $\boldsymbol{q_d}$ should be at least four times differentiable. How to include dissipative terms representing viscous friction at both transmission sides and spring damping of the elastic joints are presented in [30].

2.3.2 Control of Elastic Joint Robots

Utilizing robots in applications with unknown or changing environments or where contacts are part of the performed task, brings up the need for appropriately handling external forces during the robot's motion. For this purpose, different control strategies have been developed in the past decades that will shortly be described in the next paragraphs.

Realizing peg-in-hole tasks, screwing, or motions containing a continuous contact on a plane with industrial robots is highly dangerous because even small deviations from the desired position caused by position constraints can cause high forces and, thus, damages the environment. As a solution for this class of motions a hybrid control approach has been presented in [118] and [99] that combines force and torque information from a wrist-mounted force sensor with joint positional data to realize compliant motions. During the movement, position and force trajectory constraints are satisfied simultaneously specified in a task related coordinate system. Since the task space is divided into force and motion control, this approach is not suited if both have to be applied in the same direction. Manipulating an object affects both, force and motion control because of the dynamic coupling between the object and the manipulator. Hence, detailed dynamics information are necessary for accurate control performance, which is hard to fulfill, since in collaboration tasks the object is often not known (e.g., unexpected collisions).

In order to enable a defined and repeatable behavior on external disturbances an interaction control strategy regulating the system's impedance according to a defined model has been proposed in [60]. The impedance control reacts on a certain external disturbance in two possible complementary implementations as impedance or admittance, that is a system that accepts input motion (velocity) and outputs effort (force) or vice versa respectively. The interaction with an object can be considered in admittance causality (effort in, motion out), thus, a suitable manipulator should act as an impedance realized by position or velocity feedback and torque or current controlled actuators. The proposed approach masks the true nonlinear manipulator dynamics, that cannot be eliminated, and impose a simpler dynamics behavior, typically defined at the end-effector (Cartesian space). Alternatively, the manipulator can be controlled as admittance. The concept of admittance control is interesting in industrial robotics where the forces are measured at the end-effector using a sensor and the robot is usually position controlled [109].

Impedance control as a strategy to realize interaction between robots and the environment or human beings is in particular interesting for cobots where such interaction is of central relevance. In [4] a state feedback controller structure with gravity compensation has been presented and implemented as position, torque, or joint level impedance with an appropriate parametrization of the control gains. The asymptotic stability was shown based on the passivity characteristics of the controller. A Cartesian impedance controller based on the singular perturbation approach has been presented in [5] consisting of an outer loop controller for the Cartesian impedance and an inner loop controller for the joint torques, taking the forces of the Cartesian behavior as input. The approach presented in [4] has been extended to a Cartesian impedance controller based on the feedback of the motor position, the joint torque and their derivatives in [110] and [6] using a static equivalent of the joint position, which is a function of the motor position to realize gravity compensation. A Cartesian compliance control approach

with only using the motor position and velocity and a *gravity-biased* motor position as an alternative of joint position feedback has been presented in [142]. In [7] the control approaches for the position, torque and impedance control have been analyzed, and a passivity-based control approach that embeds torque feedback has been presented and extended for Cartesian impedance control, which has been further refined in [107]. Looking at the performance and stability properties, impedance control shows stable interaction with stiff environments but has poor accuracy in free-space caused by unmodeled effects, whereas admittance control provides a high level of accuracy in the absence of contact forces but instability during interaction with stiff environments. Based on this motivation, a unified impedance and admittance control approach that allows to continuously switch and interpolate between both implementations to create a stable and accurate performance in the particular case during a single degree-of-freedom case study has been presented in [108] and [111]. A passivity-based control approach that allows accurate Cartesian force tracking as well as compliant Cartesian impedance behavior has been presented in [123]. A comparison of compliant control algorithms for stiff and fixed-compliance robots can be found in [17].

The results presented above showed that compliant behavior in interaction with the environment can be achieved for robotic manipulators with moderate joint elasticities. The key aspects of a proper performance have mainly been an accurate sensing of the joint torques to realize torque control with appropriate actuators, and additional end-effector force sensing in some cases. The absence of this sensor information and additional model uncertainties have a crucial influence to control performance in both, free motion and contact situations. This issue will be discussed in Chapter 6.

3 Tendon Driven Series Elastic Actuation

The unique high safety features of ultra lightweight tendon driven series elastic robots are based on very low moving link masses and the mechanical decoupling of the actuator and link inertias. Nevertheless, this actuation approach introduces some challenges that include some inherent uncertainties regarding their dependability. In this chapter, the robot hardware that is used to evaluate the presented approaches, as well as the relevant drive train models are shortly introduced, followed by the description of the actuation concept related challenges.
Besides the impact force reduction capabilities of tendon driven series elastic robots, that has been investigated in [88], the safety potential according to the human's biomechanical limits must be known for the practical applicability. This potential is presented and compared to a lightweight cobot with downscaled mechanical structure, and set in relation to an optimal robot without mass. Further, the effect of high compliance is evaluated during collision tests.

3.1 The Ultra Lightweight *BioRob* Arm with Tendon Driven SEAs

The *BioRob* arm is a tendon driven robot with four elastic and one rigid, rotary joints (see Figure 3.1). The motors to actuate joint one and two are placed in the robot's base, whereas the motors for joint three and four are placed in the upper arm behind the shoulder rotary axis acting as a counterweight. The fifth, rigid joint modifies the roll angle of the end-effector and is regarded as fixed (associated with link four) if not explicitly mentioned. The robot arms without the fifth rigid joint are called *BioRob X4* or otherwise *BioRob X5*. Unless otherwise noted, the latest major hardware version is used for the experiments. In Figure 3.2, the model of the elastic transmission for one single elastic joint is depicted. The robot has been designed for safe physical human-robot interaction and is equipped with absolute joint and relative motor position encoders. In the following paragraphs, the reflection of the motor position, the position-based joint torque computation, the mechanical motor dynamics, the electrical motor equation, as well as the kinematic coupling caused by the tendons are described, for the used investigations in this thesis. Parts of this section have been presented in a preliminary version at the IEEE/ASME International Conference on Advanced Intelligent Mechatronics 2016 [77].

Motor Position Reflection

According to the described actuation, the reflected motor torque τ_m has been transferred through the gear box and tendons to the joint. Here, one has to regard two ratios, the gear

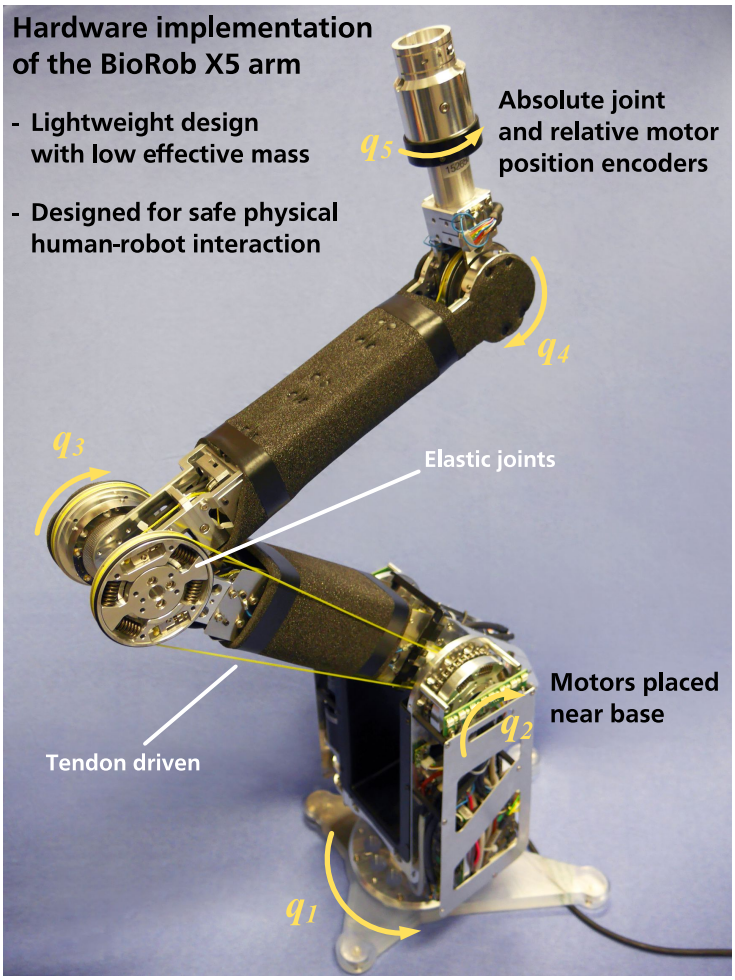

Figure 3.1.: Hardware implementation of a *BioRob X5* arm with four elastically actuated joints (fifth joint not used). The robot arm has a reach of about 75 cm, weights 7.8 kg (incl. power electronics) and a nominal payload of 500 g. The schematic actuation principle with springs embedded in the joint pulley is depicted in Figure 3.2.

box ratio n_g and the transmission ratio n_t. As depicted in Figure 3.2, the transmission ratio n_t is determined by the radius r of the motor pulley and the radius R of the joint pulley as

$$n_t = \frac{R}{r}.$$

Using these ratios, one can reflect the motor position θ_r (subscript r indicates the measured rotor position) into joint space

$${}^e\theta = \frac{1}{n_g} \cdot \theta_r \ , \quad {}^j\theta = \frac{1}{n_t} \cdot {}^e\theta \ ,$$

with the superscript e denoting the reflection to elastic actuator space (after gear transmission) and the superscript j denoting the reflection to joint space (after gear and elastic transmission). The reflected motor position ${}^j\theta$ can now be used to compute the acting joint torque. If the elastic transmission can be modeled as a linear spring, the joint torque can be computed using the known spring stiffness coefficient and the displacement between the reflected motor position ${}^j\theta$ and the joint position q, as described in the next paragraph.

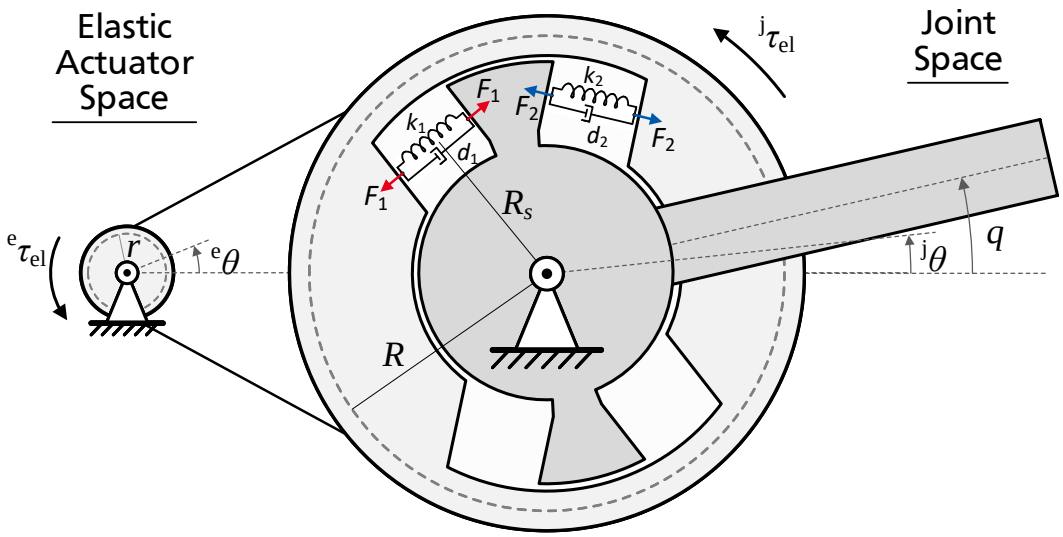

Figure 3.2.: Model of the elastic transmission adapted from [89]. Springs are placed in pulley. Parameters are: elastic actuator torque τ_{el}, elastic actuator joint torque $^{j}\tau_{el}$, spring forces F_i, spring stiffness k_i, spring damping d_i, motor pulley radius r, joint pulley radius R, spring radius R_s, angular joint position q, angular motor position $^{e}\theta$ with respect to the elastic actuator and joint $^{j}\theta$.

For better readability, all variables are assumed as reflected to the joint side, omitting the superscription in the rest of this thesis if not explicitly needed for clarity.

Position-Based Joint Torque Computation

As presented in [89] for joint torque computation with the springs placed in the tendons, one has to determine how the reflected motor position and joint position affect the spring displacement x_1 and x_2 of opposing springs, before the elastic joint torque $^{j}\tau_{el}$ computation can be performed.

If the springs are placed in the joint pulley, one first has to regard that the linear spring displacement results from a rotary displacement. Second, the spring force acts at the radius R_s unequal R. With the ratio $\frac{R_s}{R}$, that transforms the linear displacement of $\left(q - {}^{j}\theta\right)$ at radius R to the springs at radius R_s, the spring elongation can be formulated as

$$x_2 = -x_1 = R\sin\left(q - {}^{j}\theta\right) \cdot \frac{R_s}{R} = R_s \sin\left(q - {}^{j}\theta\right).$$

Now the force F_i that is exerted by the stretched springs $i \in [1,2]$ can be defined, containing the force $F_{p,i}$ of the prestreched springs, analog to [87] as

$$F_i = k_i \left(l_{\mathrm{p}_i} + x_i\right) + d_i \dot{x}_i \qquad F_{p,i} = k_i \, l_{\mathrm{p}_i} \,,$$

with spring stiffness k_i and pre-stretching spring displacement l_{p_i}. Assuming that the damping forces are small compared to the spring elongation and pre-stretched force, this can be approximated by

$$F_i \approx F_{p,i} + k_i \, x_i \; .$$

Using this force, the joint torques can be computed as

$$\begin{aligned} {}^{j}\tau_{el} &= R_s \left(F_{p,1} + k_1 \, x_1 \right) - R_s \left(F_{p,2} + k_2 \, x_2 \right) \\ &= -R_s^2 \left(k_1 + k_2 \right) \sin\left(q - {}^{j}\theta \right) \\ &= -k_e \, \sin\left(q - {}^{j}\theta \right), \end{aligned} \tag{3.1}$$

with $F_{p,1} = F_{p,2}$ and joint stiffness

$$k_e = R_s^2 \left(k_1 + k_2 \right). \tag{3.2}$$

Motor Dynamics

Analogous to the motor position, the produced motor torque has to be reflected to joint space in order to use it in the dynamics computations, here considered in the one degree of freedom (DoF) case

$$\begin{aligned} \tau_m &= \tau_r \cdot z, \\ z &= n_g \cdot n_t, \end{aligned} \tag{3.3}$$

with the reflected motor torque τ_m, the produced motor torque τ_r (subscript r indicates that the torque is regarded at the rotor), and z the combined gear box and transmission ratio.

Using the mechanical motor model one obtains

$$\tau_r = \left(I_r + I_g \right) \cdot \ddot{\theta}_r, \tag{3.4}$$

with the rotor inertia I_r and gear box inertia I_g, that can be summed up since they are expressed according to the same axis. Using (3.3) this results in the reflected motor torque computation

$$\begin{aligned} \frac{\tau_m}{z} &= \left(I_r + I_g \right) \cdot \ddot{\theta} \cdot z \\ \Leftrightarrow \tau_m &= \underbrace{z^2 \cdot \left(I_r + I_g \right)}_{I_m} \cdot \ddot{\theta} \end{aligned}$$

with the reflected motor and gear box inertia I_m. Since the acting inertias are multiplied by the square of the transmission ratio z the reflected motor inertia I_m can result in torques larger than the torques resulting from the link side inertia, which makes a decoupling of both inertias necessary to increase the human's safety.

Electrical Motor Equation

The electrical motor equation describes the electrical principle of operation of the DC motor as a function of the motor parameters known from the manufacturer provided data sheet

$$u_c = R_a \cdot i_a + L_a \cdot \frac{\mathrm{d}i_a}{\mathrm{dt}} + u_{ind}, \tag{3.5}$$

$$u_{ind} = \dot{\theta}_r \cdot k_v, \tag{3.6}$$

with the commanded voltage u_c, the terminal resistance R_a, the terminal inductance L_a, the speed constant k_v, and the induced voltage u_{ind}. Since the mechanical time constant of the motor is usually larger than the electrical time constant resulting from the terminal resistance and inductance, the influence of the inductance is omitted in the following considerations.

The electrical motor equation can be used to compute the torque that is produced, using the coupling between the motor current i_a and the motor torque described by the motor torque constant k_t

$$\tau_r = i_a \cdot k_t. \tag{3.7}$$

Solving (3.5) for i_a with subsequent insertion in (3.7) and reflecting to the joint side results in

$$\tau_r = \frac{u_c - u_{ind}}{R_a} \cdot k_t$$

$$\tau_m = z \cdot \left(\frac{u_c - u_{ind}}{R_a} \cdot k_t \right). \tag{3.8}$$

Equation (3.8) can be used for both, the computation of the current motor torque based on the commanded voltage, as well as computation of the needed voltage to create a particular torque by solving for u_c, where in this case τ_m represents the desired motor torque.

Kinematic Coupling

Biologically inspired actuation approaches that aim to rebuild musculoskeletal structures may result in tendon driven mechanisms where the tendons are routed over multiple joints, for example, to synchronize motions in bipedal robots [117], hand-like structures [45] or to enable the actuator placement more apart from the joint. This introduces kinematic couplings between the joints. In the particular case of ultra lightweight tendon driven series elastic robots, a modeling approach to represent this coupling has been presented in [88] and will shortly be described in the following paragraphs regarding the *BioRob* arm.

Since the wrist joint motor (fourth joint in the *BioRob's* kinematic chain) is placed on the upper arm, the torques needed for actuation have to be transmitted through the elbow joint. This is done by wiring the tendon over a deflection pulley in the elbow with radius r_{4d3}. This coupling has to be regarded in the computation of the equilibrium position, where the motor and joint

position produces no torque according to the elastic coupling. The kinematic equation describes that the amount of cable wrapped around the deflection pulley in the third joint must be equal to the amount of cable that unwinds from the motor pulley driving the fourth joint

$$\begin{aligned} {}^{e}\theta_4 r_4 &= q_4 R_4 + q_3 r_{4d3} \\ \Leftrightarrow {}^{e}\theta_4 &= q_4 \frac{R_4}{r_4} + q_3 \frac{r_{4d3}}{r_4}, \end{aligned}$$

indicating that the motor position of the wrist joint after reflection through the gear box ${}^{e}\theta_4$ depends on both, the joint position of joint three and four.

This tendon related dependency can be represented by a transmission coupling matrix $\boldsymbol{J_t}$. For the four tendon driven joints of the *BioRob* arm, this results to

$$ {}^{e}\boldsymbol{\theta} = {\boldsymbol{J_t}}^{-1}\boldsymbol{q} = \begin{pmatrix} \frac{R_1}{r_1} & 0 & 0 & 0 \\ 0 & \frac{R_2}{r_2} & 0 & 0 \\ 0 & 0 & \frac{R_3}{r_3} & 0 \\ 0 & 0 & \frac{r_{4d3}}{r_4} & \frac{R_4}{r_4} \end{pmatrix} \boldsymbol{q} \quad \Leftrightarrow \quad \boldsymbol{q} = \boldsymbol{J_t}\,{}^{e}\boldsymbol{\theta} = \begin{pmatrix} \frac{r_1}{R_1} & 0 & 0 & 0 \\ 0 & \frac{r_2}{R_2} & 0 & 0 \\ 0 & 0 & \frac{r_3}{R_3} & 0 \\ 0 & 0 & -\frac{r_3}{R_3}\frac{r_{4d3}}{r_4} & \frac{r_4}{R_4} \end{pmatrix} {}^{e}\boldsymbol{\theta}, \tag{3.9} $$

with the motor pulley radii r_i and joint pulley radii R_i. The influence of the elastic tendon coupling on further reflected variables is presented in detail in [88]. The gear transmission can be represented using a diagonal matrix $\boldsymbol{J_g}$ containing the gear transmission ratio $n_{g,i}$.

This definition of the tendon Jacobian and coupling matrix ${\boldsymbol{J_t}}^{-1}$ can be complemented with the definition of a separate matrix that only contains the off-diagonal coupling relations ${\boldsymbol{J_c}}^{-1}$. In the considered case of the *BioRob* arm, one obtains

$$ {\boldsymbol{J_c}}^{-1} = \begin{pmatrix} 0 & 0 & 0 & 0 \\ 0 & 0 & 0 & 0 \\ 0 & 0 & 0 & 0 \\ 0 & 0 & \frac{r_{4d3}}{r_4} & 0 \end{pmatrix}. \tag{3.10} $$

This coupling information has to be regarded for example to compute the reflected motor positions according to the given joint position and transmission torques, which is relevant in the later introduced state space controller.

3.2 Challenges in Human-Robot Collaboration for Tendon Driven SEA

An ultra lightweight tendon driven series elastic robot device can be realized in various ways and for several purposes, e.g., for industrial automation, manipulation on a mobile platform or unmanned aerial vehicle, service robotics, or even miniaturized in grippers. Besides the decision where to locate the actuators in the mechanical structure to realize an appropriate reduced effective mass or how to wire the tendons, one is facing some characteristic challenges regarding this technology.

As already motivated, in addition to the inherent safety properties of a specific system, it should be possible to detect intended or undesired contacts with the environment or a human. Since torque sensors with a practically sensor range are large and heavy, the motor and joint side position encoders for joint torque estimations (2.3) are used to fit the needs of small-sized and ultra lightweight structures. Using the reflected motor and joint side position sensor to estimate the spring elongation can be interpreted as series elasticity as presented in [115].

In order to identify the challenges of tendon driven elastic actuation, one has to analyze the properties of the involved components and their changes over the lifetime. Because of the small size structures, only pulleys with a small diameter can be used to guide the tendons. Here, cables or belts are often not applicable due to size and force requirements. However, the evolution of synthetic fibers in the last decades yield to ropes with impressing breaking force to weight (diameter) ratio, suitable to be used as force transmission component. But these materials elongate in a certain range during lifetime and further show elasticities based on the molecular structure of the specific fiber used to braid the rope. For joints consisting of flexible elements with linear spring characteristic, the overall joint stiffness consists of both, the joint stiffness introduced by the springs k_{spring} (e.g., computed via (3.2)) and joint stiffness resulting from the tendon k_{tendon} (e.g., computed as in [87]) for a single joint i

$$k_{e,i} = \left(\frac{1}{k_{spring}} + \frac{1}{k_{tendon}} \right)^{-1},$$

whereas the tendon stiffness may change because of the changed molecular structure after tension.

Since the space and maximum weight of a rotary position encoder has high limitations to keep the mechanical structure as lightweight as possible, using magnetic encoders based on the hall effect is, to the best of the author's knowledge, the common approach to capture the joint position. These sensors show a systematic sinusoidal error depending on the mounting tolerance and the sensor calibration quality. This is especially the case if the magnet and sensor are mounted separately without housing and pre-calibration. Looking at the opposite side of the drive train, the reflected motor position encoder values can contain offsets caused by an incorrect pulley ratio n_t used to reflect the position data. In contrast to the gear ratio n_g, that can be looked up from the gear's data sheet, the pulley ratio depends on the radius of actuation pulley r and joint pulley R, measured from the rotational axis to the center of the wired rope. Since the diameter of the rope changes during its lifetime, because of elongation or different loads, the pulley ratio n_t does also change, which causes incorrect motor position reflection to joint space. Additionally, the motor zero position has to be synchronized with the joint zero position, which will result in a position offset if this initialization is not done properly in an equilibrium position, because of acting disturbances as friction, backlash, or loads. In order to overcome these uncertainties, one should identify the various parameters like joint stiffness, tendon elongation, or pulley ratio. But the estimation accuracy is limited especially without direct joint torque measurement and in particular because of the time-dependent characteristic of the parameters as explained above. The schematic drawing of an elastic tendon actuation is shown in Figure 3.3 that gives an overview of the most relevant uncertainties described in this section.

Among all mechanisms that have to work properly to create a dependable robotic system (conceptually depicted in Figure 2.1), the challenges of the considered actuation concept particularly

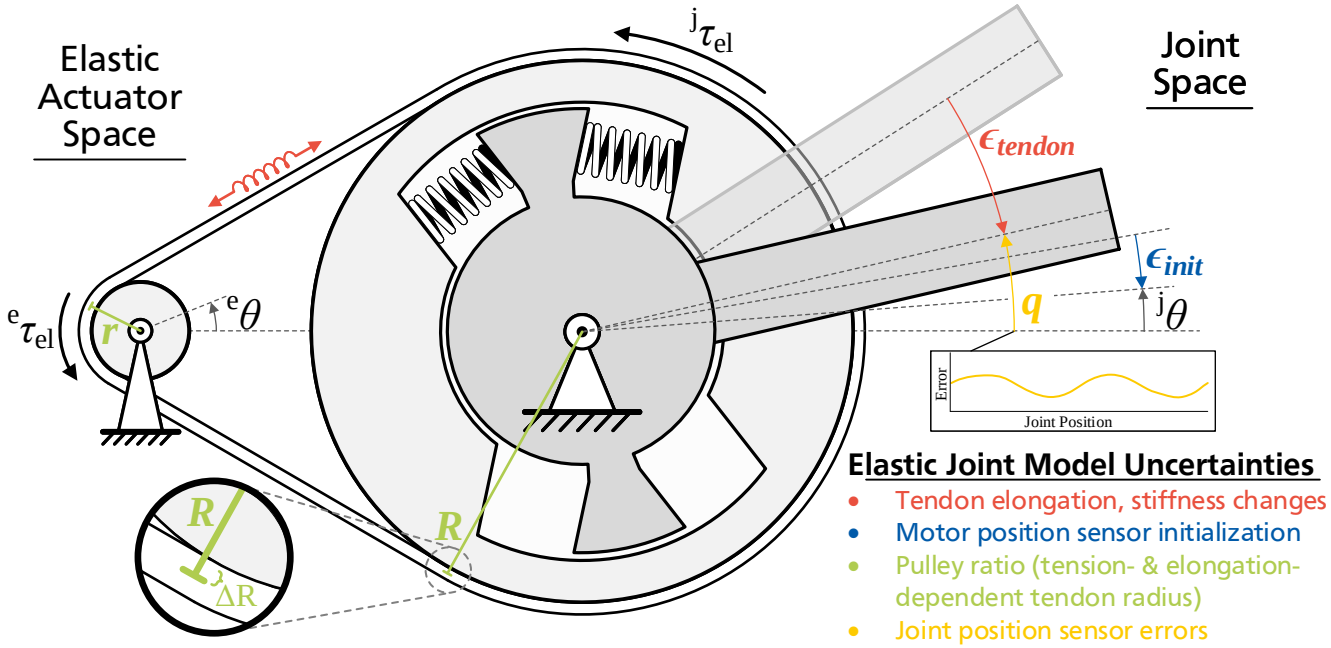

Figure 3.3.: Schematic overview of an elastic tendon actuation including uncertainties that affect joint torque estimation and control accuracy.

influence the reliability in the field of control, safety, and data processing, which in turn affects the human-robot collaboration capabilities. As already mentioned, an accurate velocity estimation is crucial for safety, control or to apply model-based approaches. For systems with high elasticities, fast movements and oscillations (because of the limited damping and stored energy) can occur. This brings up the need for a velocity estimation that performs accurately even with low-resolution position signals containing a large bandwidth of frequencies and velocities. In particular, the control performance highly depends on correct drive train information in such a way that computations, as the joint torque estimation based on uncertain model parameters, leads to unsatisfactory motion results and makes it rather impossible to realize control strategies for contact situations. Further, wear in the drive train, as tendon elongation, and external disturbances cannot be detected accurately. Not every error source presented can be isolated separately, because of the similar effects observed and the limited sensing capabilities. This makes it challenging to provide a fault tolerant system. Concerning this, different approaches and investigations are presented in the next chapters, providing new insights and analysis regarding the dependability of ultra lightweight tendon driven series elastic robots. Moreover, the collaboration and fault detection abilities of this kind of robots are investigated, also containing a preliminary user study regarding the information provision of the robot's internal state to improve the user's situation awareness and facilitating communication during collaboration tasks.

3.3 Safety Capabilities of Collaborative Robots Regarding ISO/TS 15066

As described in Section 2.1.1, at least one of the presented safety methods has to be included in collaborative operations. Besides stopping, hand guiding or keeping the robot at a certain

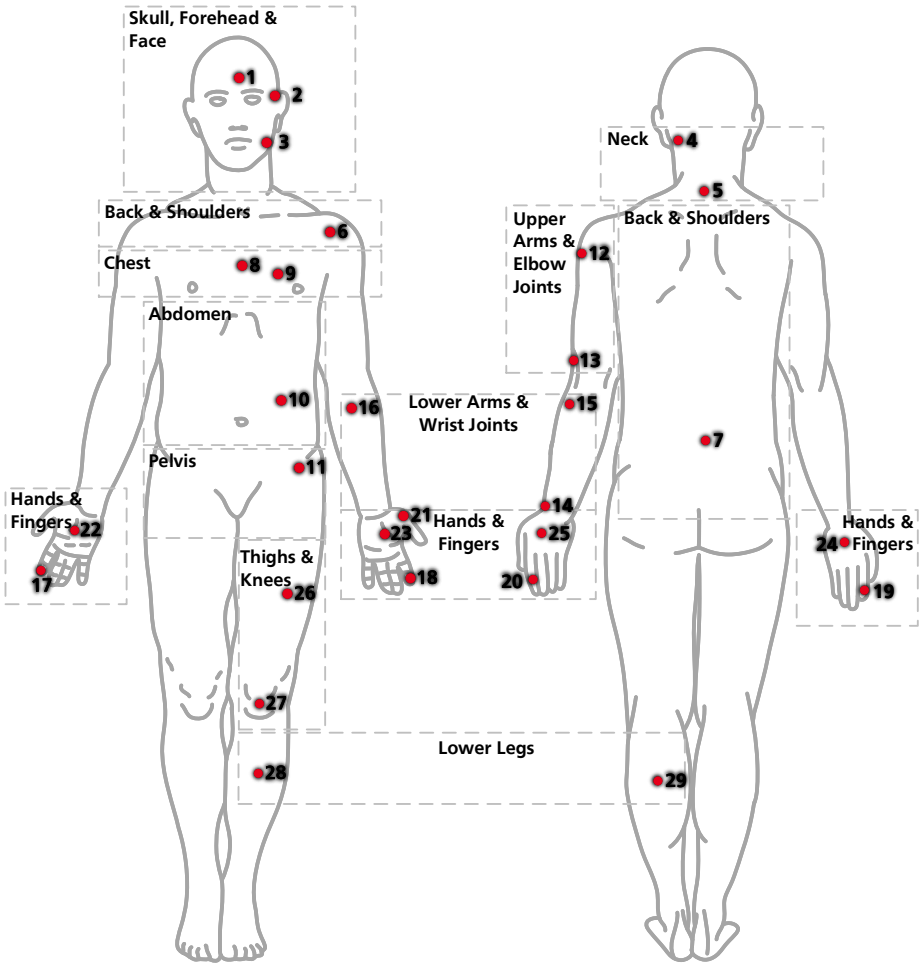

Figure 3.4.: Map of the body regions for which force and pressure limits have been determined (adopted from [102]) and regarded in ISO/TS 15066.

speed according to the distance between the robot and human, the method of power and force limiting seems to be most advantageous to obtain a productive human-robot collaboration. An insight of the effectiveness of tendon driven robotic arms regarding inherent safety to realize the *power and force limiting* method can be obtained by risk assessment according to the ISO/TS 15066 [68].

A general statement regarding the safety properties of a robot arm during undesired collisions is challenging, because different factors as collision type (free or constraint), tool (blunt or sharp), or affected body region are influencing the severity. The relevant case of free transient contacts can be evaluated as mentioned in the ISO/TS 15066. Using the relationship between the transferred energy and robot speed, as well as the human's biomechanical limits, one is able to estimate the maximum permissible end-effector velocity. The biomechanical limits have been determined for the body regions shown in Figure 3.4 [102]. In Figure 3.5 the speed limits regarding the pressure and force limits of different body regions for three robot types including payload is depicted to emphasize the differences between the tendon driven and downscaled cobots, with regard to collaboration. As the estimation of the theoretical maximum acceptable speed, a robot with no mass is assumed. Further, the speed function of a kinematically down-

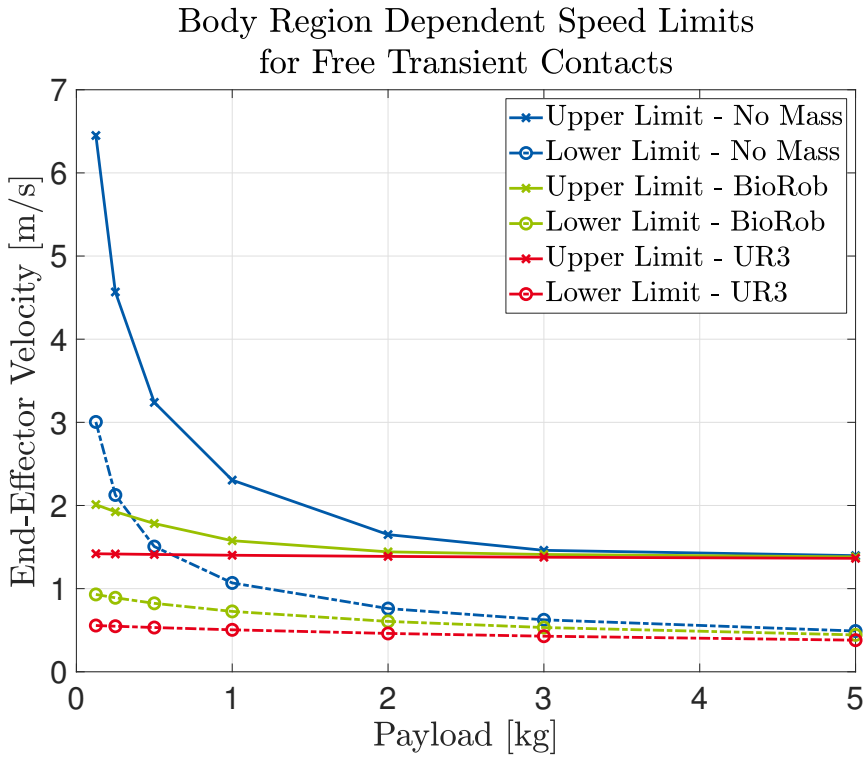

Figure 3.5.: The payload-dependent end-effector velocity range according to the biomechanical force and pressure limits from ISO/TS 15066. Permissible velocity ranges for an ideal robot without mass and the smallest currently available industrial cobot, as well as the tendon driven *BioRob X5* arm, based on the limits of body region 4 to 29 is shown.

scaled, stiff robot (*UR3*) and a tendon driven robot (*BioRob X5*) have been computed[1]. Since the effective mass estimation mentioned in ISO/TS 15066 is very simplified, it does not regard the possibility of a center of mass relocation that can be achieved using tendons. Further, the robot's effective mass highly depends on the current joint configuration and force or rather collision direction. To overcome this, an average effective mass for the whole relevant configuration space is computed, resulting in the effective end-effector mass estimations $\bar{m}_{\mathrm{UR3}} = 3.38\,\mathrm{kg}$ and $\bar{m}_{\mathrm{BioRob}} = 1.13\,\mathrm{kg}$. See Section A.1 for details.
The solid lines represent the upper and the dash-dotted lines the lower speed bounds according to the body regions 4 to 29, for which transient pressure and force limits have been specified. Comparing the small size industrial robot with the tendon driven one, the raise of the velocity bounds at identical payload illustrate that the effective mass reduction by using tendons has great inherent safety potential. This potential is especially relevant in the low payload range. On the other hand, it is possible to manipulate higher payloads at the same speed. This exemplary comparison is in general meaningful because the *UR3* seems to be in the lower end of useful kinematic downscaling. Even if the robot's weight is further reduced by using alternative materials, e.g., carbon fiber (see *Jaco²*) relocation of the motors with tendons would still improve safety potential.

[1] The dynamics parameters of the *UR3* robot have been taken from the *Universal Robots* website [131] (frequently asked questions section).

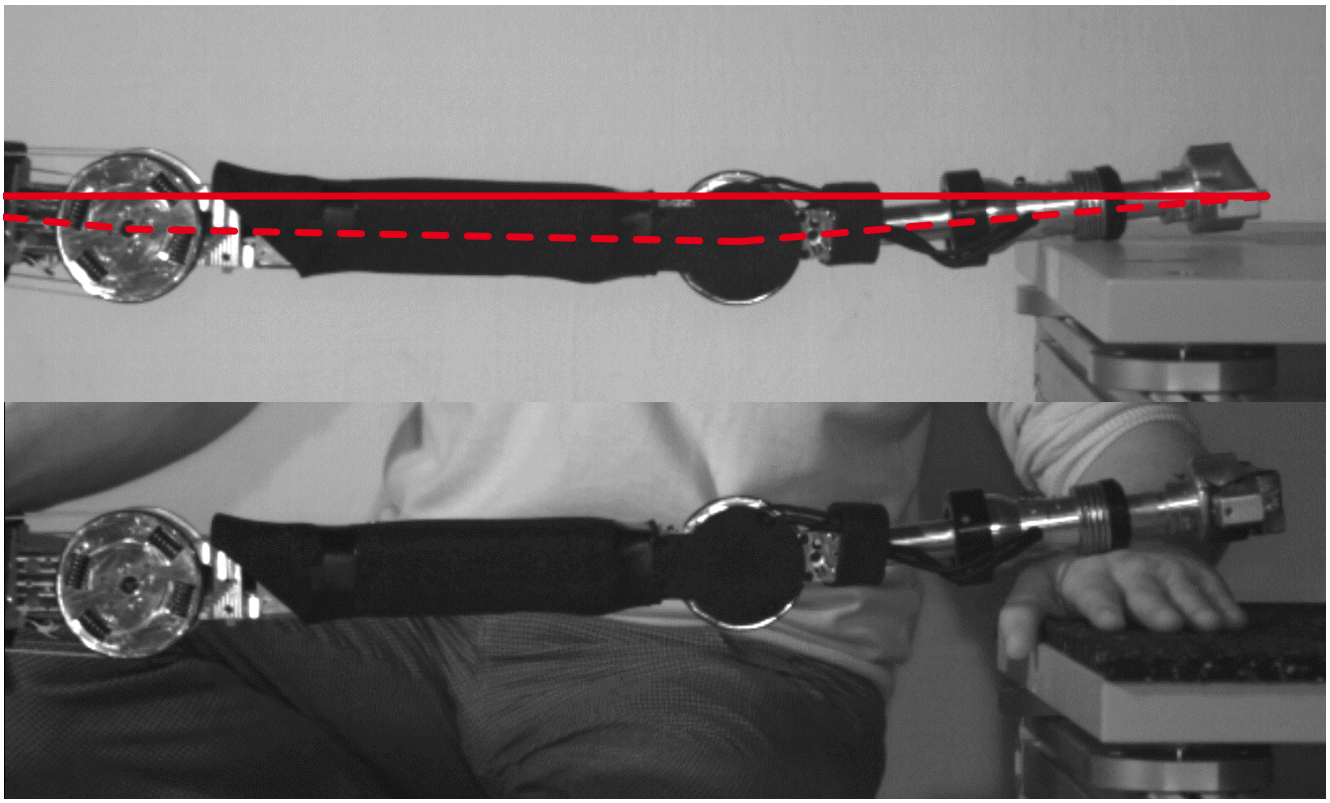

Figure 3.6.: Pictures of the collision tests with hard force plate (top) and human hand (bottom), performed with the highly elastic robot arm *BioRob X5* recorded with a high-speed camera. The bending characteristic as an immediate reaction to the contact is shown.

In the context of inherent safety, joint elasticities are of special interest. Intrinsic joint compliance is typically motivated by the goal of achieving intrinsic safety for humans. As discussed in [47], the fundamental work regarding collision tests of [13] and [141] showed that an increased joint compliance can drastically reduce the impact characteristics of the HIC. These results stay in contrast to the results of [50], where collision tests with the *DLR LWR-III* showed that a joint stiffness reduction below the intrinsic joint elasticities introduced by the gear box and joint torque sensor could not attenuate the rigid and fast impact characteristics.

In [47] these contradictory statements have been analyzed, in particular, the assumptions made about the relation between the mass and stiffness. In both works, it has been assumed for the different test setups, that the reflected motor inertia is larger than the reflected link inertia, as well as the reflected joint stiffness is significantly smaller than the regarded collision body region stiffness (head). But the assumptions differ in the relation between the reflected link inertia and collision body region mass. During the tests in [13] and [141] the reflected link inertia has been significantly smaller than the investigated body region (head), whereas in the tests with the *DLR LWR-III* the reflected link inertia has been in the same order of magnitude as the body region. It was stated that the latter case seems to be very realistic because it is valid even for a lightweight robot arm with human-like inertia properties, thus, a further stiffness reduction is unnecessary. Considering an ultra lightweight tendon driven robot arm, the resulting reflected link inertia can be changed from being in the same order of magnitude as the body region mass to the case of being significantly smaller. Consequently, a decreased joint stiffness can be used to reduce

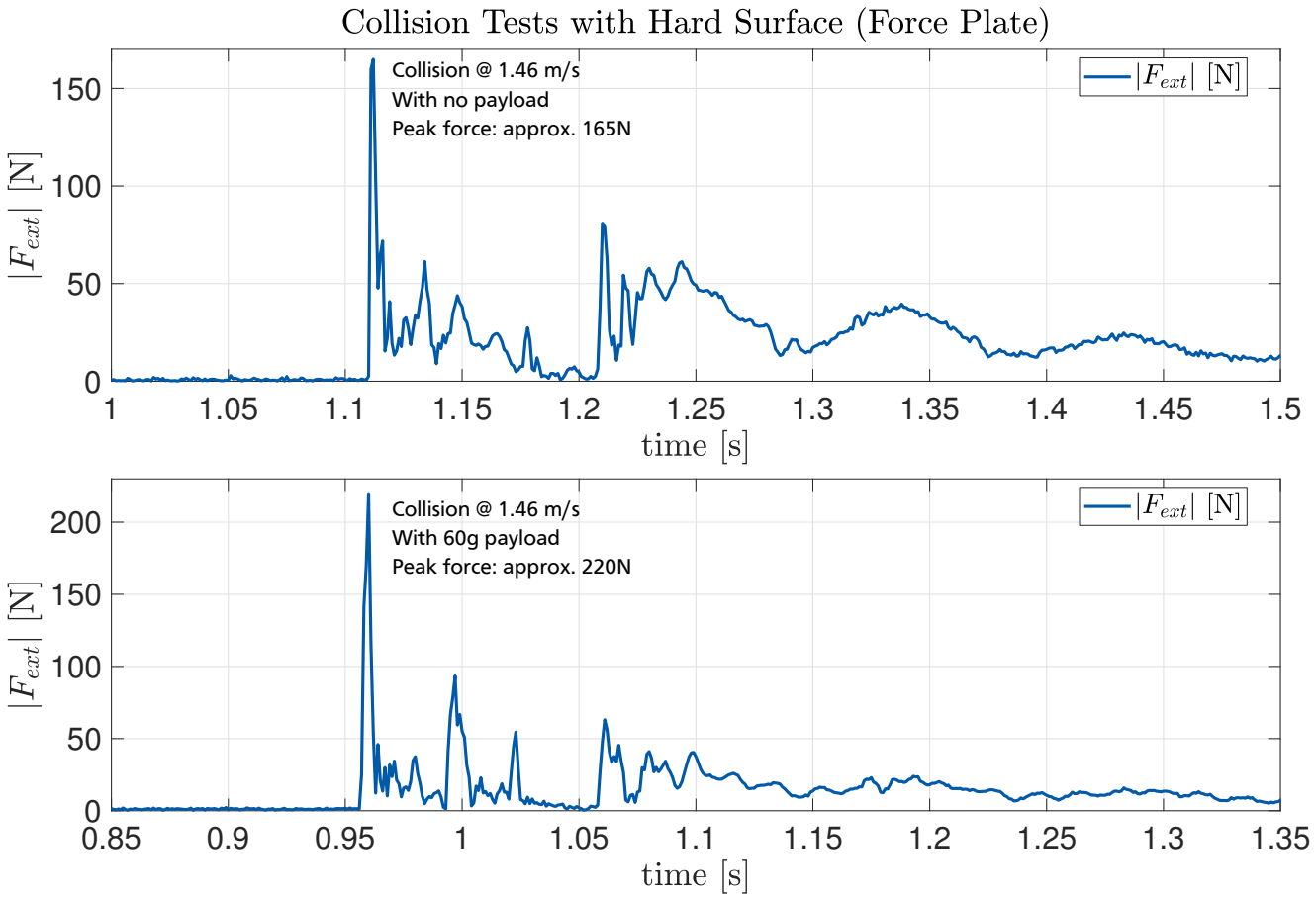

Figure 3.7.: Absolute collision forces recorded from collision tests of the *BioRob X5* (with gripper) and a force plate, without (top) and with additional load (bottom) of 60 g. Both tests are performed with the robot stretched out and maximum velocity of the shoulder joint.

the impact characteristics. Collision tests have confirmed this in simulation for elastic tendon actuated robots with different stiffness parameters in [88].

In addition to the influence of elasticities to the impact forces, their property as a mechanical low-pass filter of the external contacts is also very useful to protect the gears against high force peaks. This is especially beneficial in the case of constraint collisions because a part of the collision force is immediately used for deformation of the elastic joints and mitigates the clamping situation. Most of the cobots listed in Table 2.1 can be assumed as compliant because of the used intrinsically elastic *Harmonic Drive* gears, which are suitable for the inertial actuator and link decoupling [50]. But these elasticities are not comparable with the investigated flexible joints in this work. For instance, the *DLR LWR-III* (predecessor of the *KUKA LBR iiwa*) joint stiffness vary between 6000 Nm/rad – 15 000 Nm/rad [30], which is up to two orders of magnitude larger than the joint stiffness of the *BioRob* arm that are in the range of approximately 70 Nm/rad - 270 Nm/rad.

In order to illustrate the effect of a highly compliant robot, a collision test with the *BioRob X5* arm has been performed and filmed using a high-speed camera with 1000 fps. The test results show that the stretched robot immediately bends like an elastic rod starting with the beginning

of the contact. The collision tests with a hard surface (force plate) and a human hand are shown in Figure 3.6.

In addition to the illustration of the high compliance, the collision tests also show the practical relevance of the actuation principle with regard to safe physical human-robot interaction. The recorded absolute collision force values from the force plate are depicted in Figure 3.7. Two collision tests have been performed, with the robot stretched out, moving at the maximum velocity in the shoulder joint, and no immediate deactivation of the controller after the collision. In the first test (see Figure 3.7 top) a maximum collision force peak of about approximately 165 N has been recorded. In the second test (see Figure 3.7 bottom), an additional load of 60 g has been attached to the end-effector. Here, the force peak increased to approximately 220 N. Both recorded force peaks are below the biomechanical limits for transient contacts defined in ISO/TS 15066, which shows that high joint elasticities with tendon driven actuation are a suitable approach to build an inherent safe robot.

In this section, the great potential of a tendon driven robot with high joint elasticities to form an inherent safe robot arm has been discussed, including the possible performance according to the determined human biomechanical limits in ISO/TS 15066. Further, high elasticities introduce inherent joint impedance, which is beneficial in contact situations since position errors are immediately compensated. But on the other hand, low joint stiffness enables to store and release potential energy in the elastic elements, thus, causing joint velocities that are far beyond the motor velocities. This drastically increases the injury risk if not handled appropriately by monitoring the potential energy, ensuring safe limitation of the maximum velocities by software, damping unwanted oscillations and detect collisions [47]. These safety influences are only partially included in the ISO/TS 15066 by setting the end-effector velocity limits.

4 Velocity Estimation for Highly Joint Elastic Robots

A condensed version of this chapter has been presented at the IEEE/RSJ International Conference on Intelligent Robots and Systems 2017 and has been published in the IEEE Robotics and Automation Letters [79]

4.1 Introduction

One challenge for joint elastic robots is to reduce or even eliminate undesired swinging or oscillating motions. A damped motion would enable higher precision and increase the acceptance of such robots because safety and performance have to be in the right balance. In order to damp oscillations in a robot controller, an accurate velocity estimation is crucial. But velocity estimation is not only related to control issues. Also, observer-based methods, e.g., for friction estimation, joint stiffness estimation or collision detection, need accurate velocity estimations.

In the last decades, several velocity estimation approaches for different sensors have been developed based on numerical or statistical principles (see Section 4.2). The applicability of these approaches highly depends on the considered robotic system. Because of the lightweight structure and small size, robots for safe human-robot interaction cannot always be equipped with high-resolution position sensors. Moreover, for joint elastic systems, the application relevant range of possible velocities and oscillations can be very large. Thus, the adaptability of the desired velocity estimation method has to be appropriate. Further, the produced velocity estimation should be smooth and without a large time delay, to avoid instabilities if used for robot control.

The main contribution in this chapter is the optimization based analysis of the kinematic Kalman filter's measurement noise variance regarding velocity estimation that revealed basic properties for optimal filter performance, and on this basis, the development of a novel measurement noise variance update rule. The introduced method has been compared with a velocity estimation filter showing the best performance, according to the filter comparison of [116]. The filter performance is evaluated in simulation experiments and based on data of an ultra lightweight tendon driven series elastic *BioRob X4* arm (see Figure 4.1). During the experiments, the proposed filter approach shows higher adaptability to different filter scenarios than the compared filter. Furthermore, it is simple to adjust for use on various sensors. The accurate performance proves that the presented approach is suitable for the new class of highly elastic robots.

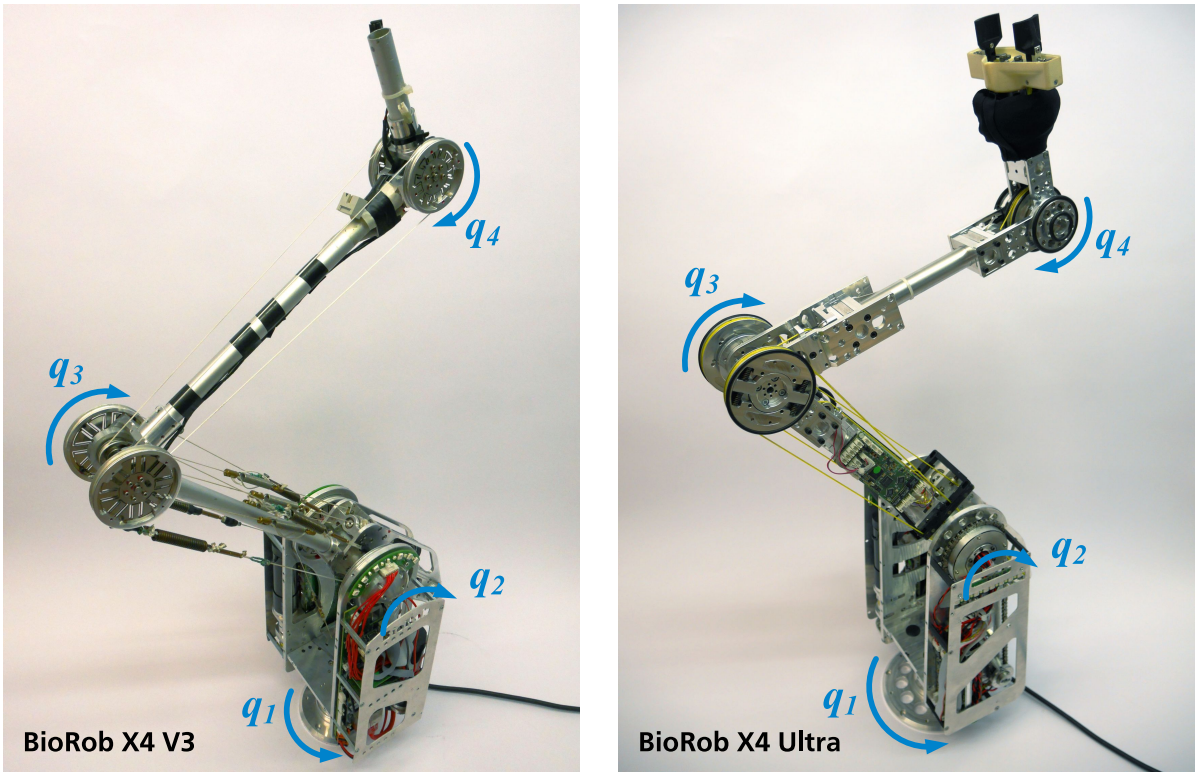

Figure 4.1.: Hardware implementation of the *BioRob X4* arm with four elastically actuated joints. The Version *BioRob X4 Ultra* (right) is an evolution of the *BioRob X4 V3* (left).

4.2 Related Work

In order to estimate the velocity from time-discrete data provided by a position encoder, one can choose between many well-studied approaches. If position encoders with finite resolution are used to estimate velocity or even acceleration, two categories of data recording have to be distinguished: encoder-driven and clock-driven [12]. Encoder-driven means, that the position reading is performed on every encoder pulse, whereas in clock-driven approaches the encoder position is recorded at fixed time intervals.

One basic approach for velocity estimation is to use a Euler-based method that computes the finite differences [15] from sampled position data. As stated in [12], the velocity resolution (encoder resolution divided by sampling time) and thus the estimation accuracy gets unacceptable at short sampling times (which is a common case in robotics), especially if the velocity is below the resulting velocity resolution. In this case, the estimation result can be improved according to the approach proposed in [92] for incremental encoders, which varies the skipped encoder positions before computing backward differences based on the maximum encoder accuracy. Such adaptive windowing techniques have also been proposed in [74] and [71]. Velocity and acceleration estimation from the pulse train of accurate optical encoders have been proposed in [84] and [113]. Another approach to reducing the noise of the finite difference outcome is to subsequently low-pass filter the result [71], which introduces a certain time delay according to the selected cut-off frequency. Alternatively, the finite differences can be computed not on

every acquired encoder position data, but only if the encoder position data changes for at least a minimum value, a so-called encoder event [103].

Another possibility to create a velocity estimation is to fit a polynomial through a number of past positions [15] or encoder events [103]. The challenge of using this approach is to find the appropriate polynomial order and number of passed samples.

Since estimating velocity from uncertain position information can be interpreted as state estimation, Kalman filtering [72] can be applied to this problem. The Kalman filter implements a Bayes filter for prediction of linear Gaussian systems [34]. It consists of a state prediction step based on a state transition probability and a correction step. A Kalman filter for optical shaft encoders based on a combination of encoder-driven and clock-driven acquired encoder data has been proposed in [12] using a third order process model. Based on the pulse train of optical encoders a single dimensional Kalman filter with adaptive noise variance is used in [125] to compute velocity and acceleration estimations. One advantage of the Kalman filter is that it can be used for sensor fusion. This has been done in [19] to estimate the joint state of an industrial robot equipped with an accelerometer for robot end-effector sensing.

The major velocity estimation approaches that can be used on digital position data have been compared in detail in [116]. This includes finite differences with subsequent filtering or computed from encoder events, polynomial fitting, Kalman filter estimation, and sliding mode differentiation approaches [23]. In the analyzed velocity range, the Kalman filter approach with a third order model and adaptive measurement variance provided the best results.

On ultra lightweight robots with elastic joints, optical encoders with high accuracy are typically too large and heavy to be used. Thus, a velocity estimation approach is needed, that can handle low-resolution position data that contains additional noise besides quantization. The filter performance during oscillations caused by the elastic drive train is of special interest. The adaptive Kalman filter velocity estimation approach proposed in this chapter is developed based on clock-driven acquired position data. Since the experimental environment in [116] also consists of low-resolution encoders with clock-driven data, evaluated on different oscillating motions, our approach is compared to the best in [116].

The proposed method only uses a kinematic process model, which keeps the computational effort low and enables to implement it on low-level controllers. Since the computational effort for integrating dynamics knowledge is high, especially for dynamic decoupled drive trains with typically no joint torque measurements, an alternative solution is preferred here.

4.3 Velocity Estimation Analysis

For using a Kalman filter for velocity estimation in the environment of elastically driven robots, one first has to choose the appropriate system model. Afterward, it is possible to investigate the filter performance in an ideal world with no sensor noise and known ground truth signal. Using this information, it is further possible to optimize the filter's parameters to discover the correlation between the parameters and the desired filter behavior. This is described in the following subsections.

4.3.1 Kalman Filtering

Using a Kalman filter is a common technique to estimate the state of a system from uncertain information and was first published in 1960 [72]. The Kalman filter produces a state estimation that minimizes the mean squared estimation error based on a given observation sequence [34]. Its time-discrete version estimates the state based on a linear stochastic difference equation [138]:

$$\begin{aligned} \boldsymbol{x}_k &= \boldsymbol{A}\boldsymbol{x}_{k-1} + \boldsymbol{B}\boldsymbol{u}_k + \boldsymbol{w}_{k-1}, \\ \boldsymbol{z}_k &= \boldsymbol{H}\boldsymbol{x}_k + \upsilon_k, \end{aligned}$$

with the state vector $\boldsymbol{x} \in \mathbb{R}^L$, the state transition matrix $\boldsymbol{A} \in \mathbb{R}^{L\times L}$, the matrix $\boldsymbol{B} \in \mathbb{R}^{L\times M}$ that relates the control input vector $\boldsymbol{u} \in \mathbb{R}^M$ to the state, the matrix $\boldsymbol{H} \in \mathbb{R}^{O\times L}$ that relates the state to the measurement $\boldsymbol{z} \in \mathbb{R}^O$ and the random variables $\boldsymbol{w} \in \mathbb{R}^L$ and $\upsilon \in \mathbb{R}^L$ that represent the process and measurement noise respectively, as well as L being the state dimension, M being the control input dimension, and O being the measurement dimension.

The system state is estimated iteratively from one time step to the next using the following equations ([138]) for the prediction (Time-Update):

$$\begin{aligned} \hat{\boldsymbol{x}}_k^- &= \boldsymbol{A}\hat{\boldsymbol{x}}_{k-1} + \boldsymbol{B}\boldsymbol{u}_k \\ \boldsymbol{P}_k^- &= \boldsymbol{A}\boldsymbol{P}_{k-1}\boldsymbol{A}^T + \boldsymbol{Q} \end{aligned}$$

with predicted state vector $\hat{\boldsymbol{x}}_k^-$ and estimation covariance matrix $\boldsymbol{P}_k^-$. For the correction (Measurement-Update):

$$\begin{aligned} \boldsymbol{K}_k &= \boldsymbol{P}_k^-\boldsymbol{H}^T\left(\boldsymbol{H}\boldsymbol{P}_k^-\boldsymbol{H}^T + \boldsymbol{R}\right)^{-1} \\ \hat{\boldsymbol{x}}_k &= \hat{\boldsymbol{x}}_k^- + \boldsymbol{K}_k\left(\boldsymbol{z}_k - \boldsymbol{H}\hat{\boldsymbol{x}}_k^-\right) \\ \boldsymbol{P}_k &= \left(\boldsymbol{I} - \boldsymbol{K}_k\boldsymbol{H}\right)\boldsymbol{P}_k^- \end{aligned}$$

where $\boldsymbol{K}_k$ is the Kalman gain that minimizes the estimated error covariance, the corrected state estimation $\hat{\boldsymbol{x}}_k$, and error covariance matrix $\boldsymbol{P}_k$. The matrix $\boldsymbol{Q}$ represents the process noise covariance and $\boldsymbol{R}$ represents the measurement noise covariance.

In order to estimate the system state, one can use various models according to the considered filter problem, e.g., a third order kinematic model [116]. Especially for elastic robots with possible human-robot interaction, sudden position changes, e.g., caused by collisions can occur. Since these collisions expose acceleration changes with a large but limited jerk, a kinematic

model for highly maneuvering targets with a constant jerk as presented in [101] is assumed to provide an appropriate system model representation:

$$\boldsymbol{A} = \begin{bmatrix} 1 & T & T^2/2 & T^3/6 \\ 0 & 1 & T & T^2/2 \\ 0 & 0 & 1 & T \\ 0 & 0 & 0 & 1 \end{bmatrix},$$

$$\boldsymbol{Q} = \sigma^2 \begin{bmatrix} T^7/252 & T^6/72 & T^5/30 & T^4/24 \\ T^6/72 & T^5/20 & T^4/8 & T^3/6 \\ T^5/30 & T^4/8 & T^3/3 & T^2/2 \\ T^4/24 & T^3/6 & T^2/2 & T \end{bmatrix},$$

with σ^2 the system process variance, the sample time period T, and the system state vector $\boldsymbol{x} = (q, \dot{q}, \ddot{q}, \dddot{q})^T$ containing the position q, the velocity $\dot{q}$, the acceleration $\ddot{q}$ and the jerk $\dddot{q}$ of the system. In the application presented here, this represents the state of one elastic robot joint. Using this model $\boldsymbol{H} = (1, 0, 0, 0)^T$ and $\boldsymbol{R}$ reduces to a scalar measurement noise variance R.

4.3.2 Analysis of Optimal Measurement Noise Variance

An appropriate velocity estimation has to perform well within a broad frequency bandwidth. Besides the different frequencies a robot can move with, the maximum velocity can also vary in a wide range. Thus, the optimal filter settings are investigated during simulation experiments with increasing position signal frequencies and amplitudes. To simulate the real world scenario, where position changes are measured via a digital encoder with limited resolution, the position signal q is quantized into a series of discrete position values q_m:

$$q_m = \left\lfloor \frac{q}{\left(\frac{2\pi}{N}\right)} \right\rfloor \cdot \left(\frac{2\pi}{N}\right),$$

with the position signal q, the resulting measured position signal q_m and the encoder ticks per rotation N.

The objective function used to evaluate the filter performance computes the error between the estimated system state $\hat{\boldsymbol{x}}$ and the real state $\boldsymbol{x}$. Here, the root mean square error is computed individually for the position, velocity, and acceleration and then added together:

$$\min_{R \in \mathbb{R}} \sqrt{\frac{\sum_{i=1}^{n} (\epsilon_{q_i})^2}{n}} + \mu_{\dot{q}} \sqrt{\frac{\sum_{i=1}^{n} (\epsilon_{\dot{q}_i})^2}{n}} + \mu_{\ddot{q}} \sqrt{\frac{\sum_{i=1}^{n} (\epsilon_{\ddot{q}_i})^2}{n}}, \tag{4.1}$$

with the position error $\epsilon_{q_i} = \hat{q}_i - q_i$, the velocity error $\epsilon_{\dot{q}_i} = \hat{\dot{q}}_i - \dot{q}_i$, the acceleration error $\epsilon_{\ddot{q}_i} = \hat{\ddot{q}}_i - \ddot{q}_i$, the number of samples n, and the weights $\mu_{\dot{q}} = 1\,\mathrm{s}$ and $\mu_{\ddot{q}} = 1\,\mathrm{s}^2$. Since the velocity and acceleration deviations are typically higher than the position deviations, these have a larger

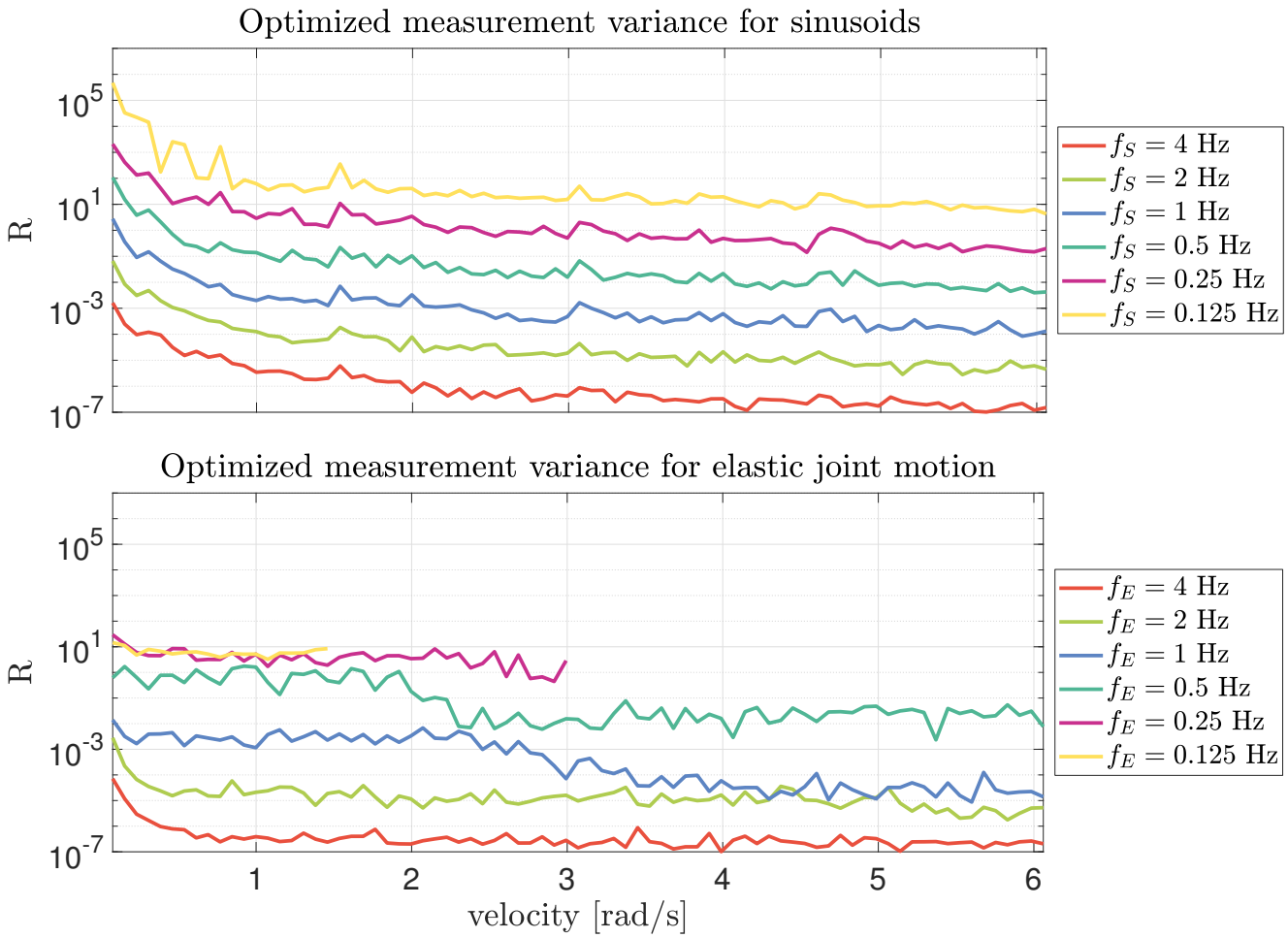

Figure 4.2.: Result of measurement variance optimization for a kinematic Kalman filter according to the objective function (4.1). The optimization has been performed on a sinusoidal position signal with various frequencies and velocities. Assuming a 12 Bit encoder ($N = 2^{12}$) the velocities changed between $\dot{q}_{max} = 0.001 \cdot \Delta v$ rad/s and $\dot{q}_{max} = 4.001 \cdot \Delta v$ rad/s in 0.05 rad/s steps, with a position sampling time $T = 1$ ms.

influence on the optimization criterion, which results in a smoother filter result. During optimization, only the measurement noise variance R is optimized, whereas the process covariance matrix $\boldsymbol{Q}$ is kept constant.

For optimization, the MATLAB Optimization Toolbox has used with the *fmincon* algorithm, suitable for minimization of nonlinear functions. The values of R are constrained to the range of $[10^{-15}, 10^{15}]$. The optimization procedure is performed for different position signal frequencies. For each frequency, the maximum velocity amplitude and, thus, the maximum acceleration amplitude is varied from a slow to a fast motion. The maximum velocity value $\dot{q}_{max} = \alpha\Delta_v$ is computed according to the velocity resolution Δ_v of the encoder for varying $\alpha \in \mathbb{R}$. The velocity resolution is computed according to $\Delta_v = (2\pi/N)/T$ with the encoder ticks per rotation N and sampling time T. Using these equations, the signals for a chosen frequency f can be obtained from:

$$\omega = 2\pi f \qquad \bar{\dot{q}} = \dot{q}_{max}/\omega \qquad q = \bar{\dot{q}} \cdot \sin(\omega t) \tag{4.2}$$

$$\dot{q} = \omega\bar{\dot{q}} \cdot \cos(\omega t) \quad \ddot{q} = -\omega^2\bar{\dot{q}} \cdot \cos(\omega t) \tag{4.3}$$

The optimization has been performed with the frequencies $f = 4, 2, 1, 0.5, 0.25, 0.125\,\text{Hz}$ and within each frequency with a velocity scaling factor between $\alpha = 0.001$ and $\alpha = 4.001$ with factor steps of 0.05. The resulting values of the optimized measurement variances R with process model variance $\sigma^2 = 10^8$ assuming a 12 Bit encoder and a third order model are depicted in Figure 4.2 (top). The R-axis is plotted in logarithmic scale. Three observations concerning the measurement variance R can be made from this analysis:

- R decreases exponentially with increasing velocity
- R depends on velocity and frequency
- R is exponentially related to changing frequencies

The signal produced by a real robotic system especially with elastic joints will not be perfectly sinusoidal and superimposed by multiple frequencies. Repeating the optimization based on position data acquired from controlling sinusoidal motions with an elastic joint result in the variance values shown in Figure 4.2 (bottom). Here, one can observe that the variance values drop even faster to the final value and also tend to reach a lower value if the signal additionally contains higher frequencies as the case for $f_E = 1, 0.25, 0.125\,\text{Hz}$. This seems reasonable in general since the filter has to be reactive for these additional frequencies. Because of the joint position limits, values for $f_E = 0.25, 0.125\,\text{Hz}$ are only available for maximum $\alpha = 2.0, 1.0$ respectively. Repeating both experiments with an order four model resulted in very similar results.

4.4 Measurement Noise Variance Update Rule

As shown in the Section 4.3.2, the choice of an appropriate measurement variance R depends on the current velocity and frequency. This has to be taken into account to achieve an optimized filter performance for velocity estimation.

A filter for velocity estimation based on position measurements needs to fulfill the following criteria:

- The filter result has to be mostly smooth.
- The velocity estimation delay has to be small.
- The filter has to be reactive within a broad bandwidth.
- The filter has to be easily adjustable.

In order to fulfill the first criterion, R should be chosen as large as possible to achieve an appropriate smooth signal without a large filter delay. To keep the filter reactive to velocity changes, R should be decreased if the filter cannot follow the measured position signal.

The proposed filter adjustment rule is based on enlarging or shrinking the current value of R, according to the observations made in the previous section. This is realized by defining an

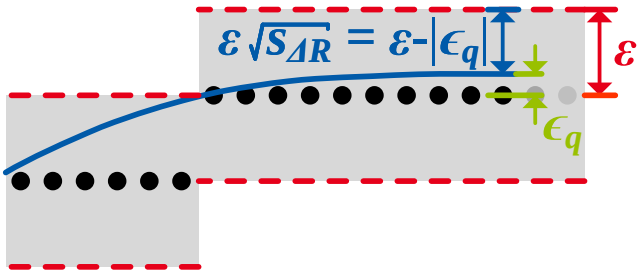

Figure 4.3.: Visualization of quantities used in update rule for measurement variance R, with accuracy region ε (gray regions with red dashed border), position estimation error ϵ_q and update step size factor $s_{\Delta R}$. The measured positions are represented by the black dots, the filter position estimation by the blue line.

accuracy region ε around the measured position. As long as the position estimation stays within this region, R is increased, otherwise, it is decreased:

$$R = \exp(\log(R) + \Delta R \cdot s_{\Delta R}), \tag{4.4}$$

with the update step size ΔR and scaling factor $s_{\Delta R}$.

As observed in the optimization experiments (see Figure 4.2), R is exponentially related to changing frequencies. Thus, before updating R with an update step size having the same scale for all frequencies, its current value is logarithmized. The update rule in (4.4) is inspired by the gradient descent method with variable step size. Transferred to the scaling of R, the distance between the estimated position and the accuracy region border ε determines scaling of the update step size ΔR, with ΔR being a user-defined constant value determining the reactiveness of the update rule. If the estimation is within the accuracy region and far away from the border, R is increased (smoother filtering). If the estimation error approaches the border, the update step $\Delta R \cdot s_{\Delta R}$ should get smaller to prevent overshooting. In the remaining case, where the estimation error is larger than the accuracy region, R must be decreased to guarantee an accurate filter result.

The step size scaling factor $s_{\Delta R}$ is calculated by

$$s_{\Delta R} = ((\varepsilon - |\epsilon_q|)/\varepsilon)^2, \tag{4.5}$$

with the position estimation error $\epsilon_q = \hat{q} - q$, where $\hat{q}$ the estimated and q the measured position, and the user-defined accuracy range ε. The meaning of the variables is depicted in Figure 4.3. The scaling factor $s_{\Delta R}$ increases quadratically with the distance of the position signal from the accuracy border. To regard the update direction, the sign of $s_{\Delta R}$ has to be set negative in case $|\epsilon_q| > \varepsilon$.

Since position encoders can produce noisy signals (additional to the quantization noise), it should be possible to adjust the filter according to this behavior. For this purpose, a heuristic to compute ε is defined. If a position variation in the sensor's position signal can be observed while the joint is in rest or slowly moving, one can use the number of position variation resolution ticks n_n (or noise factor), to approximate the noise limits similar to an estimation of the 3σ interval that covers 99.7% of the noise, in the heuristic:

$$\varepsilon = \max(0.5, n_n \cdot 0.5) \cdot 2\pi/N.$$

This heuristic assumes normally distributed noise and defines the accuracy region as half of the position variation region, with at least one half of the sensor resolution. One is free to reduce this region further, but this will result in a more noisy filter result.

Since the update rule modifies R without limitations, this has to be done afterward. Based on the optimization results (see Figure 4.2), the limits are set to a range of $[10^{-20}, 10^{20}]$. Further, the scaling factor $s_{\Delta R}$ also needs to be limited as described in Section 4.5.1.

4.5 Experimental Evaluation of Adaptive Kalman Filter-Based Velocity Estimation

In [116], an adaptive Kalman filter (AKF) with a third order process model is proposed for velocity estimation, which outperforms commonly used approaches in a sophisticated comparison, showing fewer filter errors according to different performance indices for a broader frequency bandwidth. This makes it very suitable for use with elastic joint robots, where velocity estimation has to be performed on position signals typically containing a broad spectrum of velocities and oscillation frequencies, and is, thus, used as reference filter for the proposed approach in this chapter. As for performance measures, the root mean square ϵ_{RMS}, the maximum relative ϵ_{MAX} and average relative ϵ_{AVG} errors are used

$$\epsilon_{RMS} = \sqrt{\frac{1}{n}\sum_{i=1}^{n}\left(\hat{\dot{q}}_i - \dot{q}_i\right)^2} \qquad \epsilon_{MAX} = \max_{i=1}^{n}\left|\frac{\hat{\dot{q}}_i - \dot{q}_i}{\dot{q}_i}\right| \qquad \epsilon_{AVG} = \frac{1}{n}\sum_{i=1}^{n}\left|\frac{\hat{\dot{q}}_i - \dot{q}_i}{\dot{q}_i}\right|$$

with the number of samples n.

The adaptive Kalman filter in [116] is based on the knowledge that the noise caused by encoder quantization is significant at low and neglectable at high speeds [38]. Regarding this, the measurement noise variance R_v (subscript v denotes the velocity dependency) can be recomputed using the current velocity estimation according to

$$R_v = 10R_b\left(1 + \hat{\dot{q}}\right)^{-1} \tag{4.6}$$

with the application-dependent base measurement variance R_b and the estimated velocity $\hat{\dot{q}}$. This and the proposed filter are compared first in simulation experiments to investigate the characteristic behavior and further evaluated in experiments on an elastic, tendon driven ultra lightweight robot.

4.5.1 Evaluation in Simulation Experiments

The first experiment concerns the adaptability of the filters. The filters have been evaluated on sinusoidal motions according to (4.2), (4.3) with varying frequencies $f = 0.125, 1.0, 4.0\,\text{Hz}$ and slow to moderate velocities according to maximum velocity amplitudes with $s_v = 0.01, 0.5, 1.0$. As filter parameters, the system noise variance $\sigma^2 = 10^8$ and the initial respectively base measurement variance $R = 10^{-1}$ and $R_b = 10^{-1}$ for the corresponding update rule has been set. The

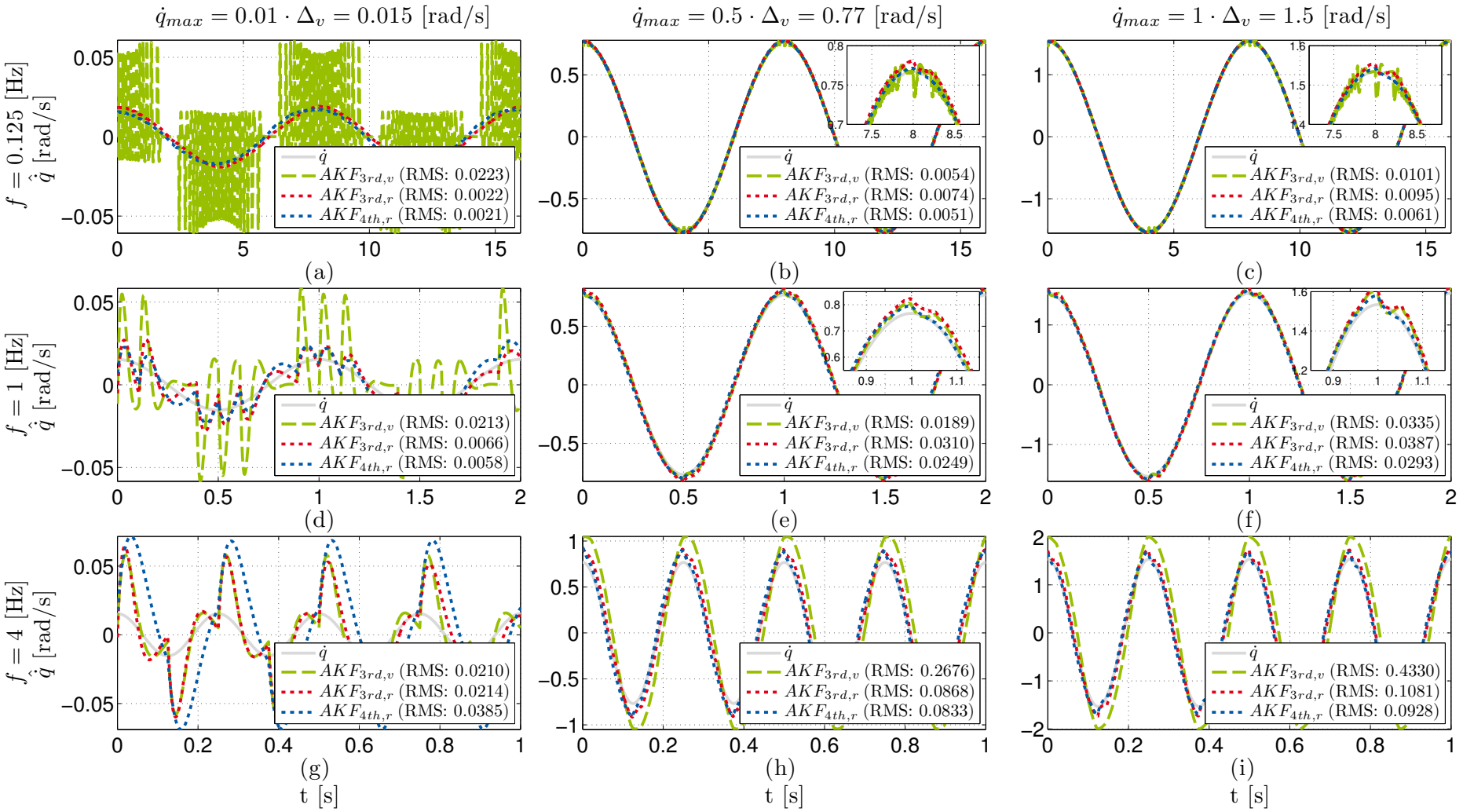

Figure 4.4.: Filter performance evaluated on sinusoidal motions with frequencies $f = 0.125, 1.0, 4.0$ Hz (rows) and maximum velocity amplitudes $\dot{q}_{max} = s_v \Delta_v$ with $s_v = 0.01, 0.5, 1.0$ (columns). The gray solid lines represents the reference velocity signal $\dot{q}$, the green dashed lines the adaptive Kalman filter based on velocity estimation $AKF_{3rd,v}$ and the dotted red and blue line the proposed adaptive Kalman filter $AKF_{3rd,r}$ and $AKF_{4th,r}$ respectively.

measurement variance has been taken from the optimization results (see Figure 4.2 top), approximately representing the optimal value for the mean frequency and velocity in the regarded range. Concerning the update Rule (4.6) and the characteristics of the optimal measurement variance, adjustments of R_b would shift the optimal filter results to another frequency and velocity range.

The results of the performed experiments for the proposed Kalman filter $AKF_{3rd,r}$ and compared Kalman filter $AKF_{3rd,v}$ are shown in Figure 4.4 with the performance indices listed in Table 4.4. The filter performance at low frequency and slow velocity (Figure 4.4 (a)) shows that the proposed filter produces smaller estimation errors for all indices. These results can also be observed for high frequency and medium to high velocity (Figure 4.4 (h), (i)) with $AKF_{3rd,v}$ showing more overshooting and a considerable signal time delay. In the case depicted in Figure 4.4 (b), (c) the ϵ_{RMS} is not sufficient to distinguish the performance. Here, ϵ_{MAX} and ϵ_{AVG} are smaller for the $AKF_{3rd,r}$ filter, thus, produce a better filter result also visualized in the close-ups. In Figure 4.4 (e), (g) the compared filter $AKF_{3rd,v}$ performs better. Whereas in case Figure 4.4 (f) both filters perform comparably well. For medium frequency and low velocity $AKF_{3rd,r}$ shows smaller errors except for ϵ_{MAX} indicating that the estimation error close to zero crossing is larger, but the small error ϵ_{RMS} is more relevant if looking at the large peaks produced by $AKF_{3rd,v}$.

Overall, the proposed filter outperforms the compared one in low frequency for the whole velocity range, mid frequency with slow velocity, and high frequency with mid and high velocity. In the remaining cases the $AKF_{3rd,v}$ performs better or equal. Adjusting R_b would shift this improved performance to another frequency range. As shown in Table 4.4 (gray values), increasing the filter's order ($AKF_{4th,r}$) mostly reduces ϵ_{RMS} compared to $AKF_{3rd,r}$ but increases the relative errors resulting from an increased phase shift.

Besides the performance evaluation in oscillation motions, another insight into to the filter properties can be gained from a step response, as shown in Figure 4.5. Here, the two relevant step signals in case of velocity filtering are shown, with a position measurement sampling time of $T = 1\,\text{ms}$ and $N = 2^{12}$ sensor ticks per turn. In the left column, a step of $\pi/50\,\text{rad}$ is introduced in the position signal, where in the right column the velocity signal contains a step of $\pi\,\text{rad/s}$. In all experiments, the proposed filters show lower overshooting. Whereby, $AKF_{3rd,r}$ and $AKF_{4th,r}$ are quite reactive since they show a small settling time of 3 ms. Considering the velocity step, $AKF_{3rd,v}$ follows the velocity signal faster but shows a larger overshoot. The step experiments further showed for the encoder with $N = 2^{12}$ ticks that the overall update value $\Delta R \cdot s_{\Delta R}$ of R should not get larger than 10. Otherwise, the filters $AKF_{3rd,r}$ and $AKF_{4th,r}$ produced a continuous oscillating velocity estimation.

The bandwidths of the filters are evaluated via a frequency analysis of a sinusoidal motion with an amplitude of a multiple of the sensor resolution. The filter result is then analyzed regarding the amplitude amplification and phase shift in comparison to the input signal using a Fourier transformation. The result is shown in Figure 4.6 using a Bode diagram. The filter input signal has an amplitude of $20 \cdot \Delta_p$ (amplitude of approximately 1.75 °) using a sensor with a resolution of $N = 2^{12}\,\text{Bit}$. The frequency analysis from 0.125 Hz to 480.0 Hz shows that the resonance frequency of the proposed filter update rule of $AKF_{3rd,r}$ and $AKF_{4th,r}$ is much higher than for the alternative filter $AKF_{3rd,v}$. Even for the investigated small motion, a filter performance for $AKF_{3rd,r}$ and $AKF_{4th,r}$ with low amplitude amplification and phase shift up to approx. 100.0 Hz

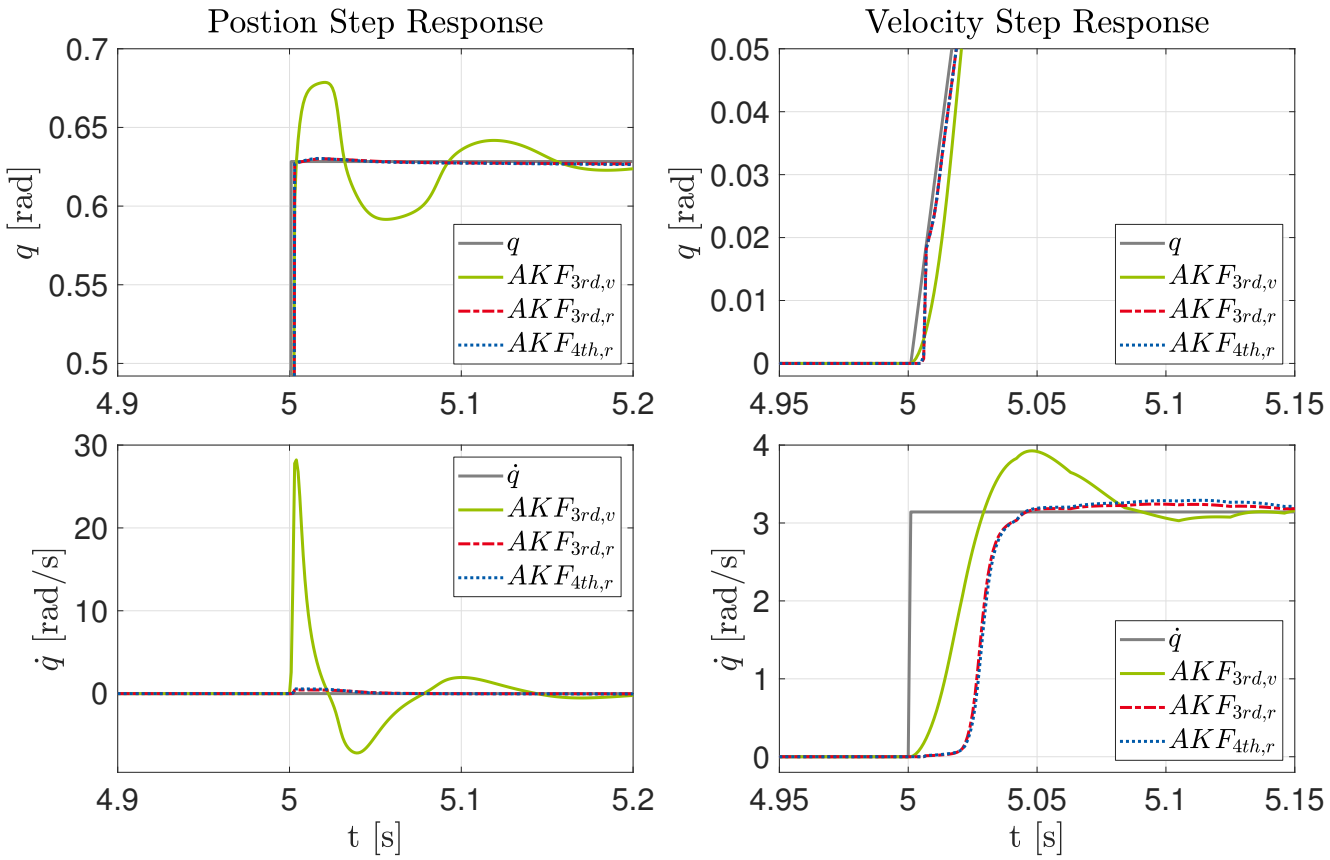

Figure 4.5.: Step response behavior of the investigated adaptive Kalman filters for a position step of $\pi/50$ rad (left column) and a velocity step of $\pi/10$ rad (right column).

is obtained. The detail plots for 0.2 Hz and 8.0 Hz show the time domain filter results, which is less noisy for the proposed filters especially for a low frequency (which is not immediately evident using only the Bode diagram) and has a small phase shift for mid to high frequencies. Both filters with the proposed update rule behave quite similar in the case without noise but with the $AKF_{3rd,r}$ filter showing a smaller resonance peak.

Performing the same analysis with noise in the position signal ($n_n = 2.0$) showed that the filter performance of $AKF_{4th,r}$ still has low noise, amplitude amplification and phase shift for low frequencies and only a slightly higher amplitude amplification for high frequencies, compared to the performance with no noise. This also holds for $AKF_{3rd,r}$, except that the phase shift is increased, what makes the higher order filter more suitable in this case. The filter results are shown in Figure A.2

4.5.2 Evaluation in Robot Experiments

In order to investigate the filter behavior on real-world data, the filter's performance has been evaluated using the *BioRob* arm [89]. This ultra lightweight (approximately 7.8 kg mass) tendon driven robot is highly elastic because of the used springs. The arm is equipped with rotary position encoders on the motor and joint side. Since the elasticities decouple the motor from

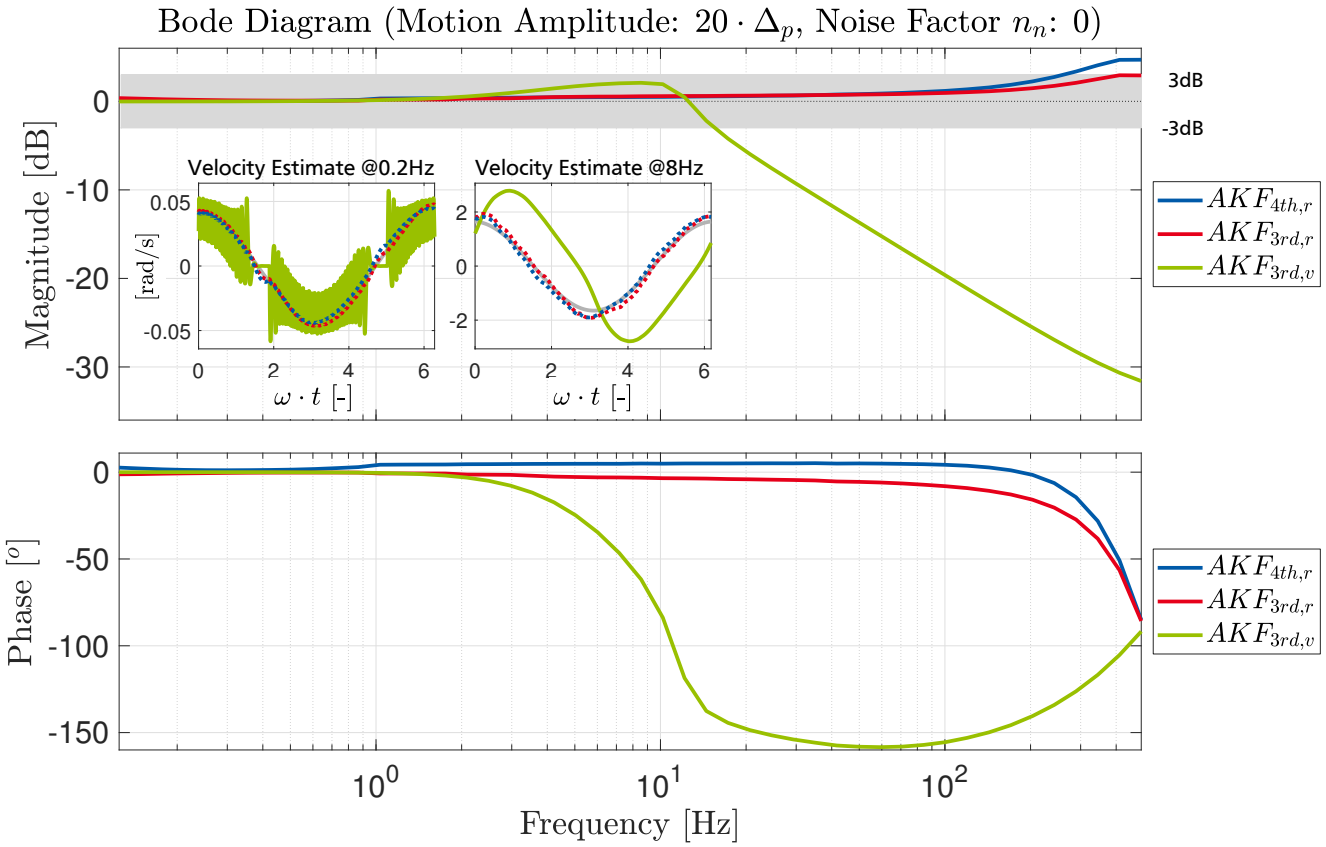

Figure 4.6.: Bode diagram for the adaptive Kalman filters. Analyzed amplitude amplification and phase shift of velocity estimation resulting from a sinusoidal motion with an amplitude of $20 \cdot \Delta_p$ sensor resolution steps. Gray area represents the 3 dB region. Detail plots show the time domain velocity estimation according to 0.2 Hz and 8 Hz motion with true velocity in gray.

joint actuation, a robust velocity estimation on the joint side is crucial for good control performance. Due to the lightweight structure, only small and light sensors can be used. Magnetic encoders based on the Hall effect can fulfill these requirements and are used in the *BioRob* arm. The position values are acquired clock-driven each $T = 1$ ms according to the control frequency of 1 kHz.

The filter performance has been evaluated using experiments that cover the common scenarios, as slow to fast motions with oscillations, sudden changes of the end-effector load and point to point motions (pick and place). In order to visualize the velocity resolution and noise behavior of the sensors, the finite backward differences (FD) are shown. The velocity estimation reference signals have been computed offline with a two-sided Savitzky-Golay smoother (linear polynomial with manually tuned window length) that is well suited to reproduce the signal from sampled data.

In the first robot experiment, the adaptability of the filters is investigated. For this, a sinusoidal motion with an amplitude of approximately 2.5 ° and increasing frequency starting from $f = 0.05$ Hz to $f = 4.05$ Hz in 10 steps is executed on the *BioRob X4 V3*, with a sensor resolution of $N = 2^{12}$ ticks per revolution. Here, a simple motor side P-Controller is used to actuate the robot. To regard noise, the base measurement variance is set to $R_b = 10^0$ and, since with the considered

encoder hardware the positions varied one to two ticks with the joint in rest, the noise factor is set to $n_n = 1$. The filter results are depicted in Figure 4.7 and performance measures listed in Table 4.1. Analog to the simulation experiment, $AKF_{3rd,v}$ shows a noisy velocity estimation at low velocities and a remarkable overshoot with a time delay at high velocity and frequency. According to the experimental evaluation, the proposed filters $AKF_{3rd,r}$ and $AKF_{4th,r}$ barely show noise at low speed and only little overshooting at high-speed motions, resulting in overall smaller estimation errors.

Sudden changes of the end-effector load can strongly alter the motion behavior of elastic systems. This has been investigated during placing and releasing an object (500 g) with the *BioRob X5 Ultra* (16 Bit sensor with low noise) that causes oscillations after the place motion. The velocity estimations are shown in Figure 4.8 ($R_b = 10^{-1}$, init $R = 10^{-1}$, $n_n = 1$) and the estimation errors of both phases (place motion, release object) are listed in Table 4.2. According to the estimation errors, all filter show a rather similar performance during the place motion, whereas the proposed filter is more accurate during the oscillation phase.

A typical task for robots consists of part handling with a pick and place motion. This kind of motion has been performed with the *BioRob X4 Ultra* arm to show the adjustability of the proposed filters. Velocity estimation has been performed on different position signals, with a separate filter for each signal. After only adaption of the sensor resolution and noise factor parameters for $AKF_{3rd,r}$ and $AKF_{4th,r}$ according to the measurement (see finite differences in Figure 4.9), the filters estimated the velocities as depicted in Figure 4.9 (only half a cycle shown) and with the estimation errors listed in Table 4.3. Even at signals with high noise, the filters produce an accurate performance, with nearly similar accuracy in a subsequently repeated second cycle.

4.6 Conclusion

In this chapter, the Kalman filter based velocity estimation using low-resolution encoders has been investigated for ultra lightweight tendon driven elastic robots. For this, the measurement variance characteristics regarding a wide range of signal velocities and frequencies have been analyzed. Based on these observations, a novel adaptive measurement noise variance update rule has been introduced that is easy to adjust to other encoders. This rule uses the filter's position estimation error (residual) to decide whether the velocity estimation should be smoothed or is not accurate enough.

The proposed filter has been compared to the most promising alternative based on the analysis of [116]. It has been shown in simulation and robot experiments that the new adaptive Kalman filter approach adapts better to the investigated application scenario of an ultra lightweight tendon driven elastic robot with low time delay. Furthermore, it produces a smooth and accurate velocity estimation over a wide bandwidth, which is promising with regards to using for control purposes. Additionally, the general filter concept is not limited to be used on highly elastic robots and also provides an acceleration estimation that should be investigated in further studies.

Table 4.1.: Estimation errors of recorded motion according to Figure 4.7.

Filter	ϵ_{RMS}	ϵ_{MAX}	ϵ_{AVG}
$AKF_{3rd,v}$	0.2611	38.9285	0.6860
$AKF_{3rd,r}$	**0.0643**	**8.9916**	**0.2372**
$AKF_{4th,r}$	0.0688↑	11.9324↑	0.2543↑

Table 4.2.: Estimation errors of recorded motion according to Figure 4.8.

Motion	Filter	ϵ_{RMS}	ϵ_{MAX}	ϵ_{AVG}
Place Object	$AKF_{3rd,v}$	0.0470	1.4721	0.3459
	$AKF_{3rd,r}$	0.0467	1.4633	0.3481
	$AKF_{4th,r}$	0.0468	1.5575	0.3441
Object Released	$AKF_{3rd,v}$	0.0533	2.4545	0.5494
	$AKF_{3rd,r}$	0.0442	1.4607	0.5028
	$AKF_{4th,r}$	0.0443	1.4793	0.5274

Table 4.3.: Estimation errors of recorded motion according to Figure 4.9, for motor velocity in the shoulder joint ($\dot{\theta}_s$), and the joint velocity in the shoulder ($\dot{q}_s$) and elbow joint ($\dot{q}_e$).

Signal	Cycle	Filter	ϵ_{RMS}	ϵ_{MAX}	ϵ_{AVG}
$\dot{\theta}_s$	One	$AKF_{3rd,r}$	0.0176	1.1400	0.0656
		$AKF_{4th,r}$	0.0224	1.3903	0.0850
	Two	$AKF_{3rd,r}$	0.0187	1.0549	0.0650
		$AKF_{4th,r}$	0.0228	1.2256	0.0733
$\dot{q}_s$	One	$AKF_{3rd,r}$	0.0320	1.3416	0.1165
		$AKF_{4th,r}$	0.0358	1.5757	0.1268
	Two	$AKF_{3rd,r}$	0.0315	1.5378	0.1054
		$AKF_{4th,r}$	0.0339	1.5296	0.1046
$\dot{q}_e$	One	$AKF_{3rd,r}$	0.0863	3.1109	0.2823
		$AKF_{4th,r}$	0.0939	2.5239	0.2842
	Two	$AKF_{3rd,r}$	0.0873	3.3753	0.2964
		$AKF_{4th,r}$	0.0936	3.5369	0.3281

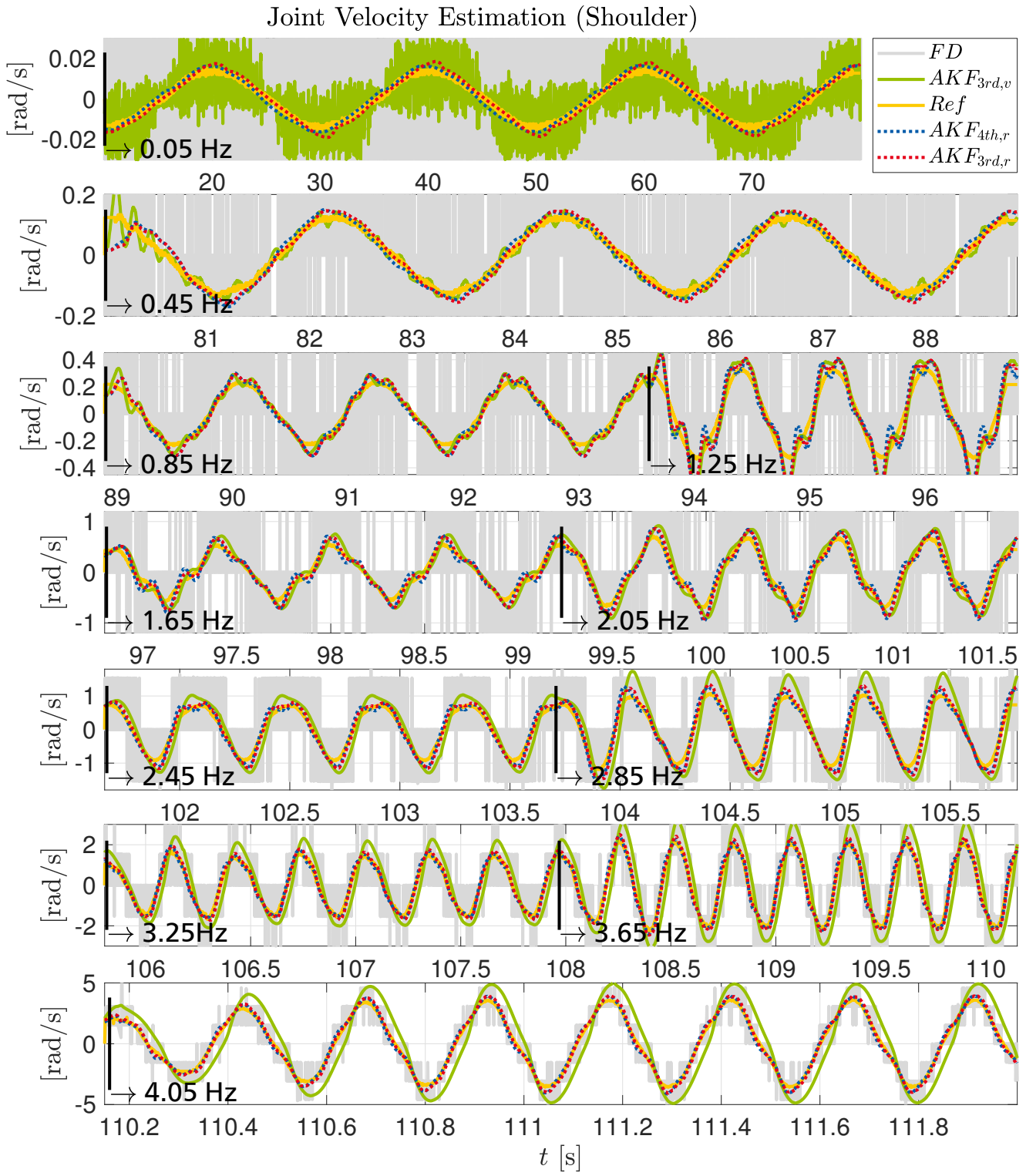

Figure 4.7.: Filter performance of a sinusoidal motion with increasing frequencies recorded from the robot experiment with the *BioRob X4 V3* arm.

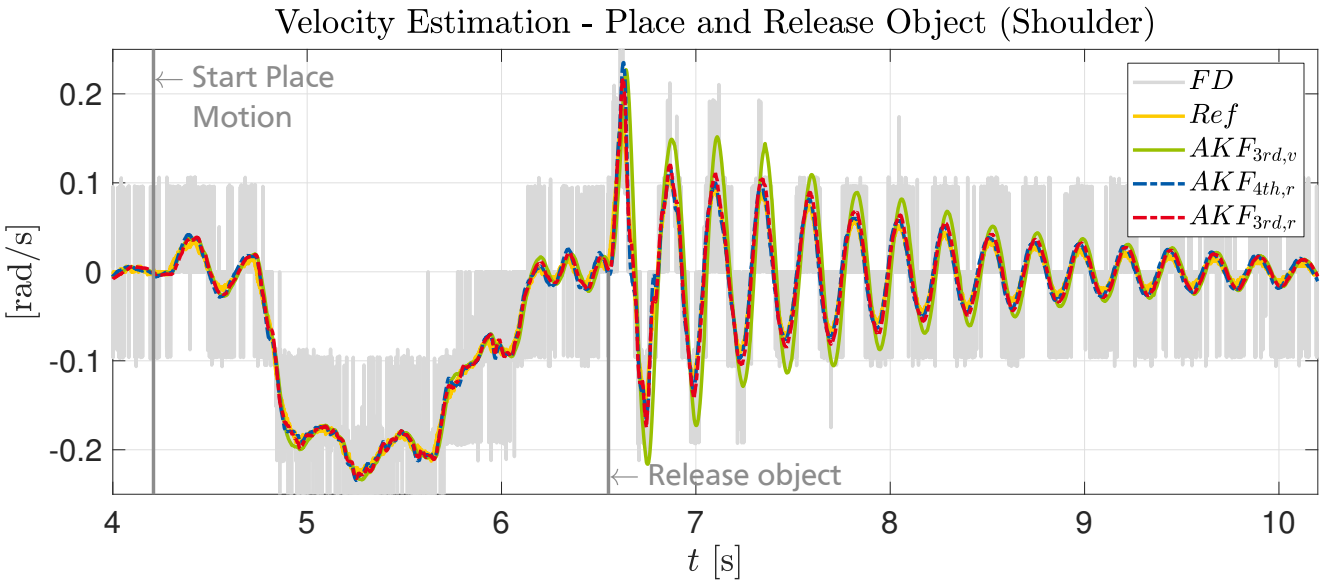

Figure 4.8.: Velocity estimation during object (500 g) placing and releasing with the *BioRob X5 Ultra* arm.

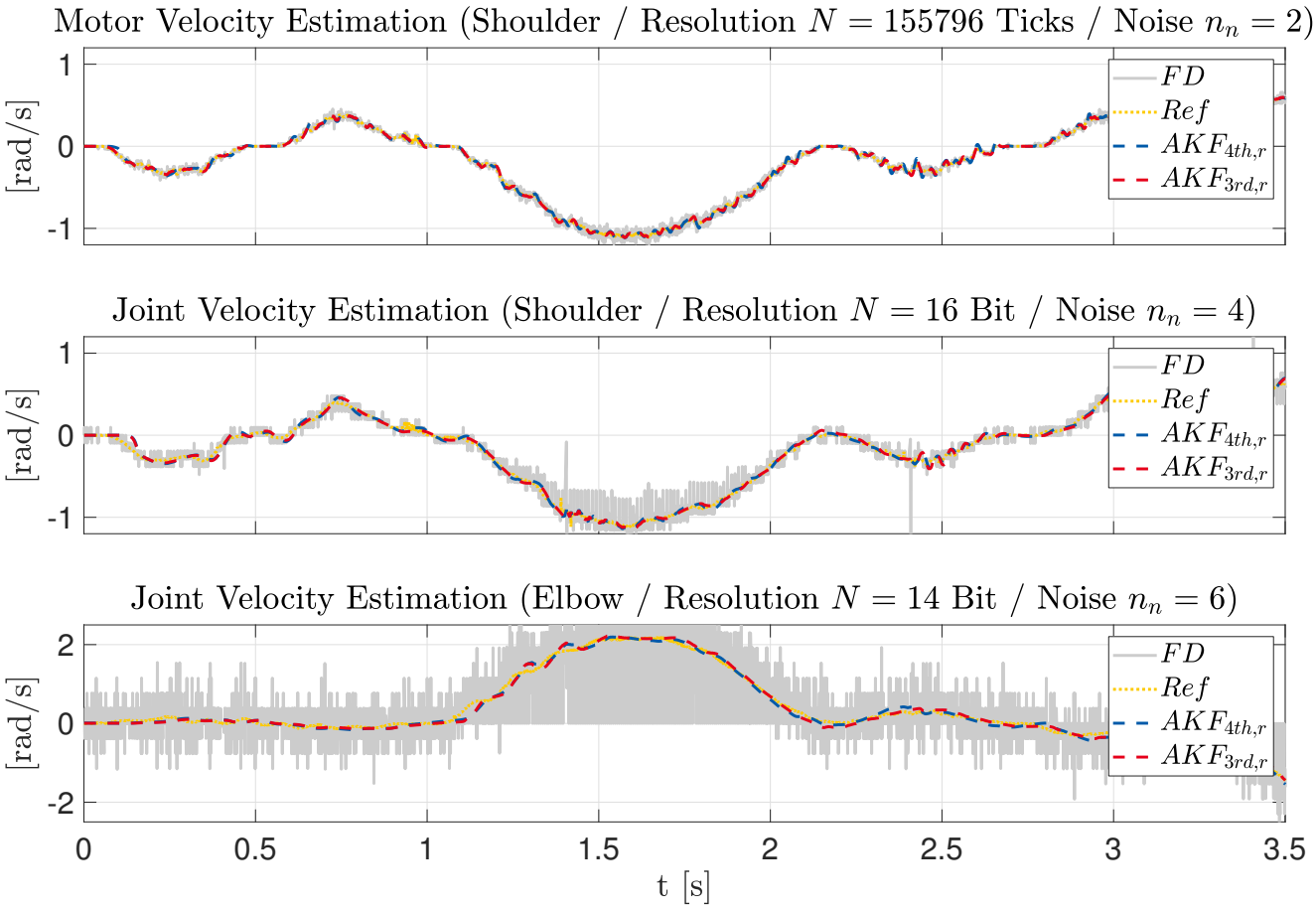

Figure 4.9.: Velocity estimation during a pick-and-place motion with the *BioRob X4 Ultra* arm in shoulder and elbow joint. The motor resolution is reflected through the gear to the joint, creating a high-resolution, low noise signal.

Table 4.4.: Estimation errors of simulated sinusoidal signals according to Figure 4.4.

		$\dot{q}_{max} = 0.01\Delta_v$			$\dot{q}_{max} = 0.5\Delta_v$			$\dot{q}_{max} = 1.0\Delta_v$		
	Filter	ϵ_{RMS}	ϵ_{MAX}	ϵ_{AVG}	ϵ_{RMS}	ϵ_{MAX}	ϵ_{AVG}	ϵ_{RMS}	ϵ_{MAX}	ϵ_{AVG}
	$AKF_{3rd,v}$	0.0223	10.8689	1.8739	**0.0054**	11.076	0.0444	0.0101	16.4375	0.0395
$f = 0.125$ Hz	$AKF_{3rd,r}$	**0.0022**	**0.9554**	**0.1941**	0.0074	**1.5983**	**0.0199**	**0.0095**	**2.9077**	**0.0153**
	$AKF_{4th,r}$	0.0021↓	2.7270↑	0.2811↑	0.0051↓	5.6780↑	0.0388↑	0.0061↓	5.6363↑	0.0240↑
	$AKF_{3rd,v}$	0.0213	**4.5651**	1.9639	**0.0189**	**1.6306**	**0.0549**	**0.0335**	**2.2612**	**0.0558**
$f = 1.0$ Hz	$AKF_{3rd,r}$	**0.0066**	8.9505	**0.7019**	0.0310	2.7000	0.0896	**0.0387**	**2.2519**	**0.0576**
	$AKF_{4th,r}$	0.0058↓	7.8055↓	0.7320↑	0.0249↓	6.1141↑	0.1400↑	0.0293↓	2.7718↑	0.0743↑
	$AKF_{3rd,v}$	**0.0210**	**3.5214**	**1.6973**	0.2676	30.2556	1.4333	0.4330	25.5303	1.1989
$f = 4.0$ Hz	$AKF_{3rd,r}$	**0.0214**	17.2821	2.0267	**0.0868**	**2.7127**	**0.1914**	**0.1081**	**0.7184**	**0.1037**
	$AKF_{4th,r}$	0.0385↑	39.1094↑	5.4942↑	0.0833↓	12.0087↑	0.4702↑	0.0928↓	7.1051↑	0.2779↑

5 Synthetic Fiber Rope Elongation and Detection

A condensed version of this chapter has been presented at the IEEE/ASME International Conference on Advanced Intelligent Mechatronics 2017 [78].

5.1 Introduction

Besides industrial automation, tendons can also be relevant for other fields of human near applications. Reproducing human or animal-like walking can benefit from the use of tendons. Even if their use is only passive without actuation, it is possible to realize a joint coupling more similar to the biomechanical mechanisms which help to synchronize the joints and facilitates the control task [124]. Also for wearable robots, e.g., to support elderly people performing a motion or new types of orthoses, tendons can help to create a more comfortable and lightweight structure.

Independent of the specific application, tendons can be implemented in different ways. For instance belts or steel cables can be used to move joints, as done in some industrial robots. But these solutions are not necessarily suitable for structures where pulleys with small radii are used, and high forces have to be transmitted. In these cases, synthetic ropes should be considered. In the last decade the evolution of synthetic fiber materials and production processes led to products with impressing strength (see Table 5.1).

Since safety and weight limit the scale of robots in the vicinity of humans, also the used pulleys and thus rope diameter is limited. Synthetic ropes with small diameters are typically used in the area of sailing and sports activities that use kites or parachutes. Here, the relevant parameters are the rope's diameter, breaking strength and weight. But these are not always suitable to decide about the utilization potential in a complex mechatronic system where a rope is wound around multiple pulleys. Especially, the irretrievable rope elongation characteristic (creep) is a relevant factor that should be known and continuously monitored because of the negative influence on the joint position control performance.

The contribution in this chapter consists of

- new comparative creep experiments regarding different fiber materials, manufacturers, and diameters,
- the experimental evaluation of the influence of a different amount of pulleys on commonly used HMPA fiber,

- and an observer-based approach for tendon elongation detection to monitor wear for quality assurance.

The performed experiments give new insights into the rope elongation characteristics, which are typically not provided by the rope manufacturers.

5.2 Related Work and Background

Using ropes as tendons in robotic systems provides the opportunity of small scale mechanical design, because of the high flexibility, high strength to weight ratio, and possible small bending radius. That is the reason why they are used for example in systems like anthropomorphic hands [69], [94], [22], bipedal robots [100], [117], small size ultra lightweight robot arms [18], [62], [85] or novel actuation approaches [105].

Synthetic ropes can be braided in different ways using different fibers. These fiber materials have evolved in the last decades improving the strength to weight ratio and reducing creep effects. A comparison of rope constructions and fiber characteristics can be found in [122]. For the application of tendon driven robots, ropes need to have high strength at low elongation and be resistant to abrasion. The ropes regarded in this chapter meet these requirements and consists of High Modulus Polyethylene (HMPE), Liquid Crystal Polymer (LCP) and Aromatic Polyamide (Aramid). As presented in [122], the Polybenzoxazole (PBO) fiber shows the lowest elongation at break but has low abrasion resistance [128] and is therefore not regarded.

Besides general fiber characteristics, it is important to investigate the rope's application-dependent performance. To abstract from the specific scenario, different experiments can be performed, as a tensile creep test where a constant force is exerted to the rope and the elongation over time at a certain temperature is measured, a bending fatigue test where a rope is cycled over a sheave under a constant tension, or winding the rope to investigate the contact effects. The test results of such tests are typically not provided by the specific rope manufacturer. Recent investigations regarding the fundamental mechanical behavior of synthetic fiber ropes, in particular consisting of HMPE and Aramid fibers, have been performed for example in [24], [93], [91], and [134].

Since the production process and braid can influence the rope's characteristics, a comparative evaluation of different ropes using a tensile creep test and a test similar to a bending fatigue test is performed. The bending fatigue test is modified according to the application of tendon driven robots, in particular, by winding the rope and additionally investigating the influence of the number of guiding pulleys that stress the rope. To the author's knowledge, such analysis has not yet been performed but is required for the design process of tendon driven robots. Further, an observer-based approach will be presented to estimate the rope elongation during its life cycle.

Table 5.1.: List of evaluated ropes produced by various manufacturers in a diameter range from 1.22 mm to 2.05 mm, a breaking load of at least 200 daN produced with usually utilized fibers. All information have been provided by the manufacturers.

Manufacturer	Product	Fiber	Material	Diameter	Breaking Load	Plait	Weight
Gottifredi Maffioli	SK99 Ultra	Dyneema SK99	HMPE	2.00 mm	560 daN	-	2.50 g/m
Liros	Aramid Braided Cord	Aramid	Aramid	2.00 mm	250 daN	16-plaited	-
Liros	DC000-0301	Dyneema SK99	HMPE	1.50 mm	445 daN	12-plaited	1.45 g/m
Liros	DC000-0701	Dyneema SK99	HMPE	2.00 mm	700 daN	12-plaited	3.05 g/m
Ockert	Climax Combat	Dyneema SK75	HMPE	1.22 mm	210 daN	-	-
Teufelberger	FL-32.NG	Dyneema DM20	HMPE	1.50 mm	350 daN	8-plaited	1.80 g/m
Teufelberger	FL-9.NG	Dyneema SK75	HMPE	2.05 mm	650 daN	12-plaited	3.30 g/m
TU Chemnitz	-	Technora Black	Aramid	1.80 mm	-	-	-
TU Chemnitz	-	Vectran	LCP	1.80 mm	-	-	-

5.3 Investigation of Rope Elongation Characteristics

As described in Section 5.1, the creep characteristics of ropes are a relevant factor if they are used to move parts that have to be accurately position controlled. In order to compensate for the irreversible tendon elongation, the actuator position has to be adjusted appropriately. Thus, a rope with less creep is desirable for the specific application. Since information about the creep characteristics is typically not available for the end products but only qualitative characteristics for the raw fibers [122], these have to be identified by experiment.

In this chapter, the two types of performed experiments are described. The First experiment has been carried out in cooperation with the State Materials Testing Institute (MTI) Darmstadt (area of expertise plastics and composites) comparing ropes of different manufacturers, fibers, and diameters at a specific operating point. In the second experiment, a rope is fixed in a test setup to move a revolute joint via different types and numbers of pulleys. This experiment aims to be closer to the usage in a real mechatronic system.

5.3.1 Evaluated Ropes

The set of ropes used in the experiments results from market research of ropes with a diameter of 1.22 - 2.05 mm and a breaking load of at least 200 daN. These values are determined by the development experience with tendon driven robots ([85], [117]) where small pulley radii are limiting the upper diameter range and also causing high rope forces when used in the drive shaft. Further, only ropes have been chosen for which at least a minimum number of parameters (fiber type, diameter, breaking load) are provided. The selected manufacturers are mainly from Germany but using customary fibers. For additional fiber comparison, two ropes from the TU Chemnitz provided by the MTI are considered in the test set. All ropes are listed in Table 5.1.

5.3.2 Tensile Creep Experiments

The tensile creep experiments are performed following [64] under standard atmosphere 23/50 [65]. A force of 60 N is applied to the rope pieces of 350 mm length during 85 min. The applied force is kept constant over the whole experiment while simultaneously measuring the rope elongation. The same force has been used for all ropes to compare their elongation characteristic according to one defined operating point since this is typically necessary if a rope for a specific application has to be chosen. This experiment has been repeated for a subset of ropes in a heating cabinet with 60 °C.

The experimental results of the tensile creep experiment under 23 °C are depicted in Figure 5.1 and discussed in this paragraph. The parameter m_E shown in the legend represents the slope of the curve starting at 20 min created by fitting a linear polynomial. Only looking at the rope's diameter and breaking load, one could expect that the 2 mm ropes (except the Aramid fiber because of the low breaking load) will outperform the other ones. But this is not the case, as

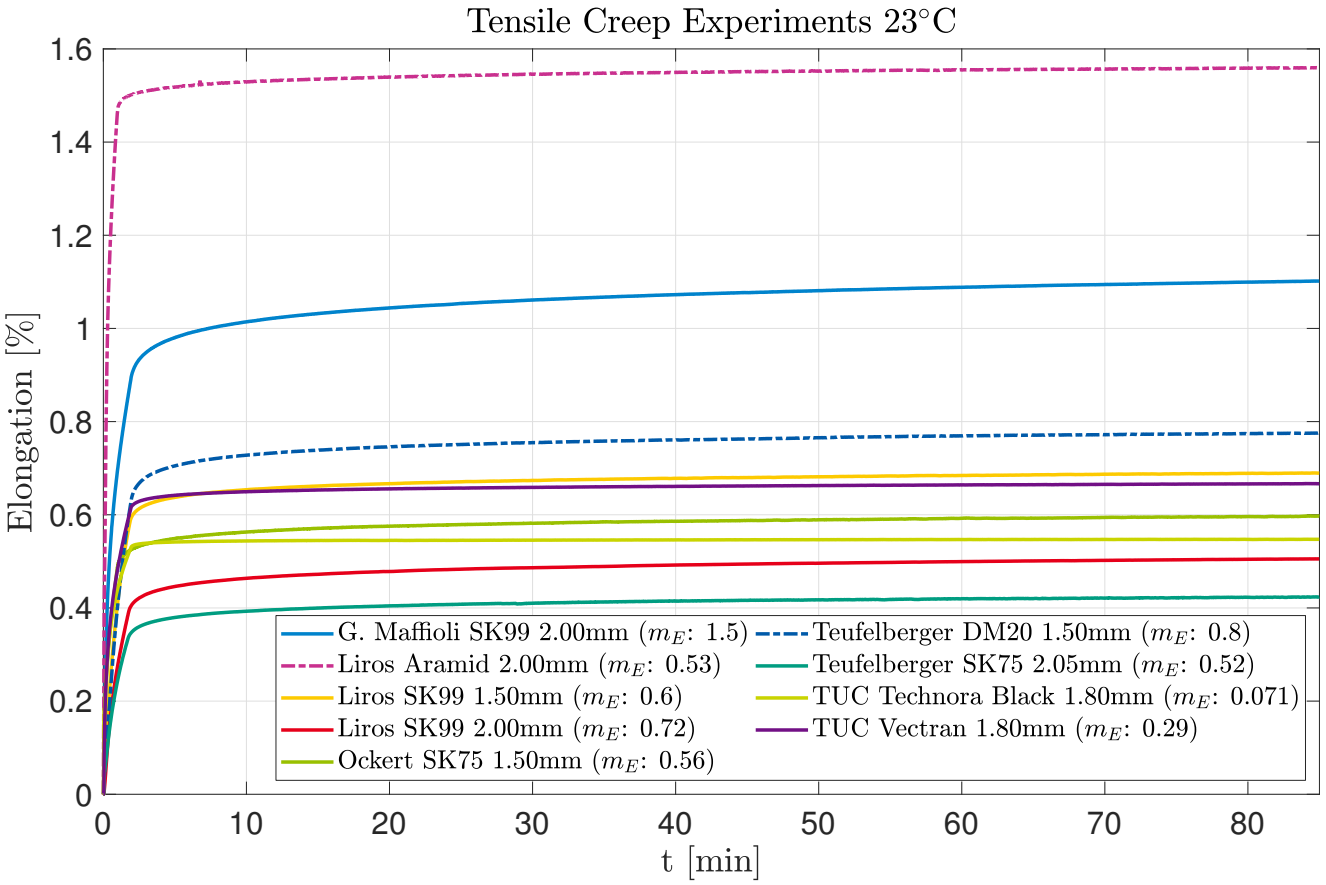

Figure 5.1.: Elongation results of the tensile creep experiments exerting a constant force of 60 N to the ropes with 350 mm length at 23 °C.

can be seen with the *Gottifredi Maffioli SK99 Ultra* rope, although it consists of a new generation of the *Dyneema* fiber *SK99*. Among the HMPE ropes on can observe that, the newer fiber in *LIROS SK99* rope performs not better than the predecessor fiber in *Ockert SK75*. Comparing the *Aramid* fiber rope with the *Ockert Climax Combat* that has a rather similar breaking load shows a final elongation that is more than half as large as smaller diameters. The elongation slopes of these ropes are almost the same. The final elongation of the set of ropes with a diameter smaller that 2 mm is within a range of almost 0.2 %. Besides this, the two fibers *Technora Black* and *Vectran* provided by the MTI show less elongation slope than the other ropes.

In the second tensile creep test setup, the environment temperature has been increased to 60 °C. The experiments were performed for the four different fibers *DM20* (HMPE), *SK99* (HMPE), *Technora Black* (Aramid) and *Vectran* (LCP). Since *SK75* and *SK99* are evolutions of HMPE fibers, only one rope consisting of *SK99* is regarded. The results, as illustrated in Figure 5.2, show that all ropes except the *Liros SK99* reaches an elongation similar to 23 °C. Further, the *Technora Black* and *Vectran* fiber present only a low incrementation of the elongation slope. In contrast to this, the *SK99* and *DM20* fiber largely decrease the elongation slope. It is noticeable that the elongation of the *Liros SK99* rope finally reaches a value that is only half of the value measured at 23 °C. One possible explanation for this behavior is that the increased temperature facilitates the fiber molecules to reach a state of higher entropy, which acts against the elongation. This

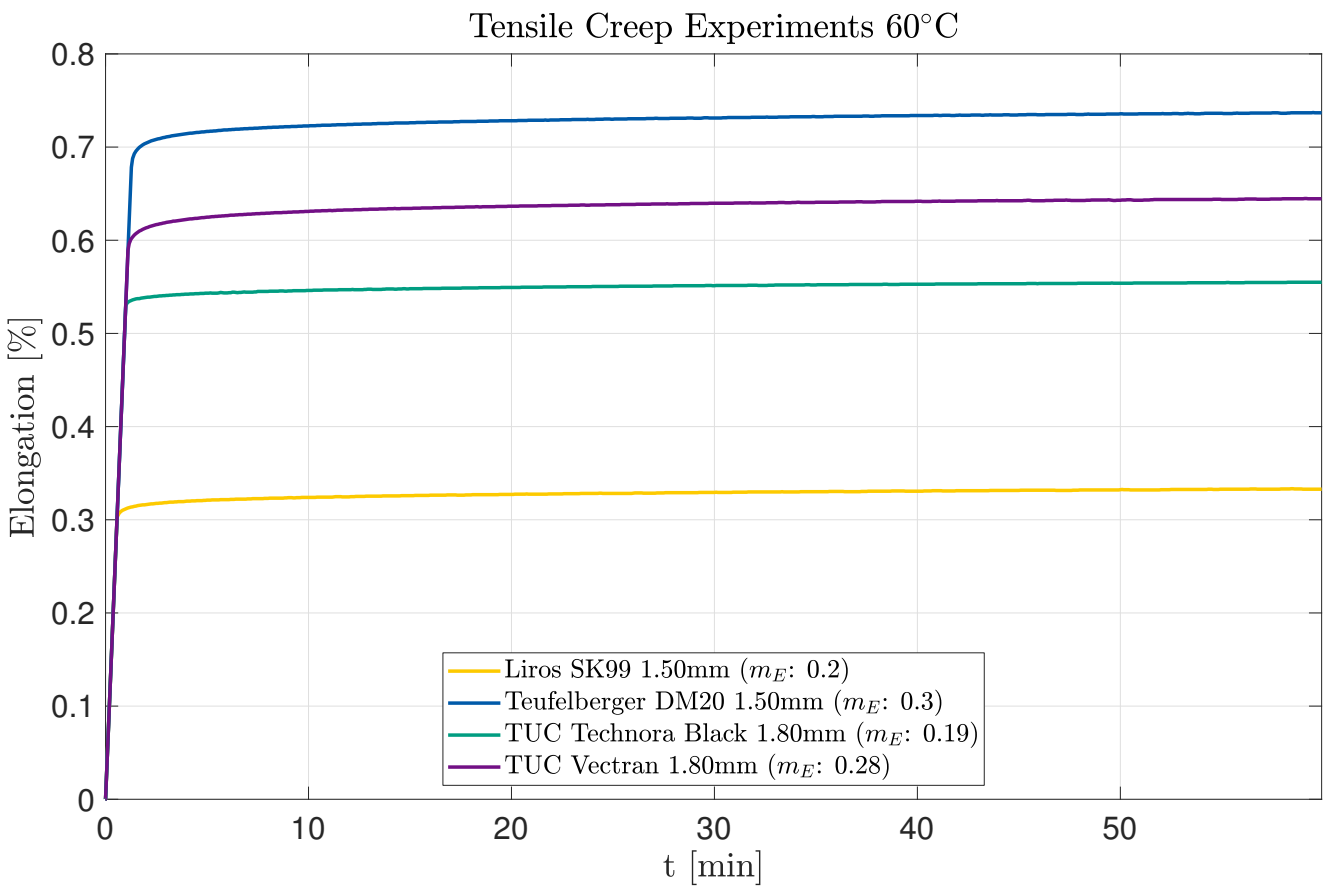

Figure 5.2.: Elongation results of the tensile creep experiments exerting a constant force of 60 N to the ropes with 350 mm length at 60 °C.

meets the statement in [122] that HMPE fibers show degradation at a temperature higher than 65 °C.

Summarizing the tensile creep experiments, all ropes show an asymptotic saturation in elongation with a low but not neglectable elongation slope. Further, the production process and the way how a rope is braided changes the elongation behavior more than can be represented by the commonly provided breaking force, especially if the operating point is far below. The difference between the *Aramid* ropes is remarkable high, whereas the *Technora Black* and *Vectran* fibers are really promising in particular because of the low elongation slope.

5.3.3 Bending Experiments

Using ropes in the drive train of an actuated system introduces further influences regarding the rope's elongation behavior. Typically, a rope is guided by pulleys to transmit a force. These guiding pulleys exert a force on the braided rope structure that is orthogonal to the transmitted force. In order to investigate the influence of these guiding pulleys on the elongation characteristics, the test bench as shown in Figure 5.3 is used.

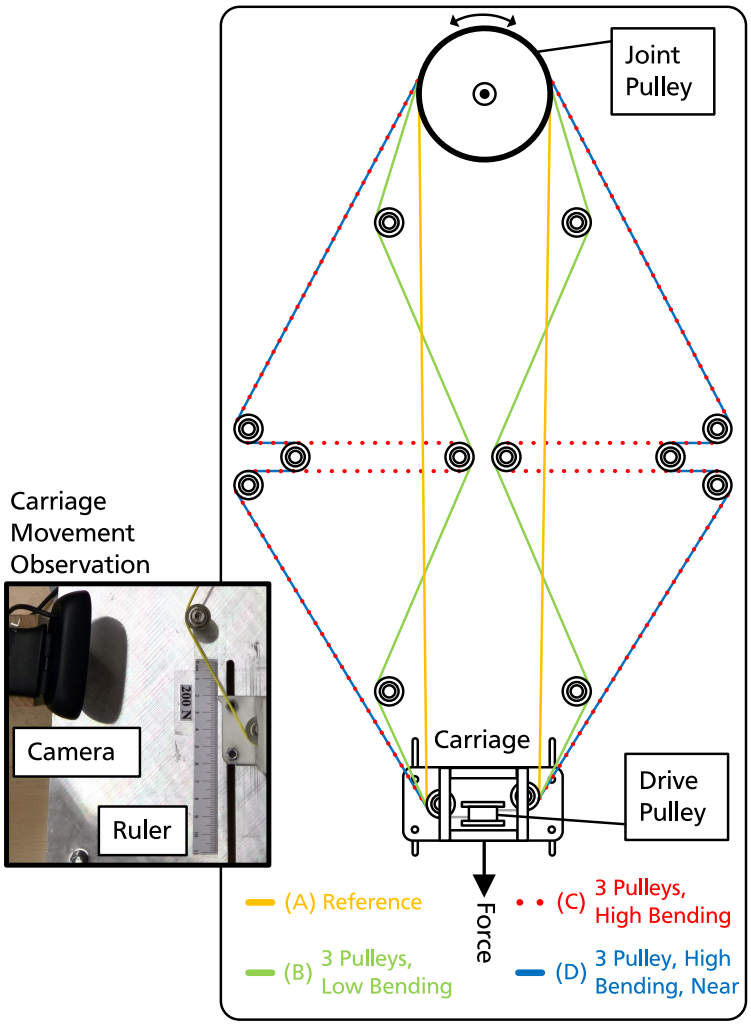

Figure 5.3.: Test bench for bending test execution. The movement of the carriage is recorded using the camera for four different rope routings (A)-(D), while the rope is periodically moved rotating the joint pulley, with a constant force pulling the carriage.

The test bench consists of the electrical part to actuate the drive pulley comprising of the power supply, power electronics, DC motor, and bus communication, as well as the mechanical part to guide the rope in different ways from the drive pulley to the rotary joint pulley, see Figure 5.3. The motor is mounted on a movable carriage that can be pulled with a defined force. The rope elongation is measured via the movement of the carriage using a half millimeter scale and a camera. Four different rope routings (A)-(D) are examined. As a reference experiment, the rope connects the drive pulley with the joint pulley without additional guiding. After this, three guiding pulleys in different arrangements from low to high rope bending (wrap angle) are introduced.

During the experiments, the motor rotates in a sinusoidal motion in a way that a length of approximately 10 cm of the rope is repeatedly unrolled. A force of 200 N continuously pulls the carriage that ideally results in a force of 100 N in each rope. Experiment (B) only slightly bends the rope and consists of a small wrap angle in each guiding pulley. The distance between the pulleys is larger than the unrolled rope length, thus, the stressed rope segments are distinct. In experiment (C) one guiding pulley is placed in a way that the rope is bent more than 180 °,

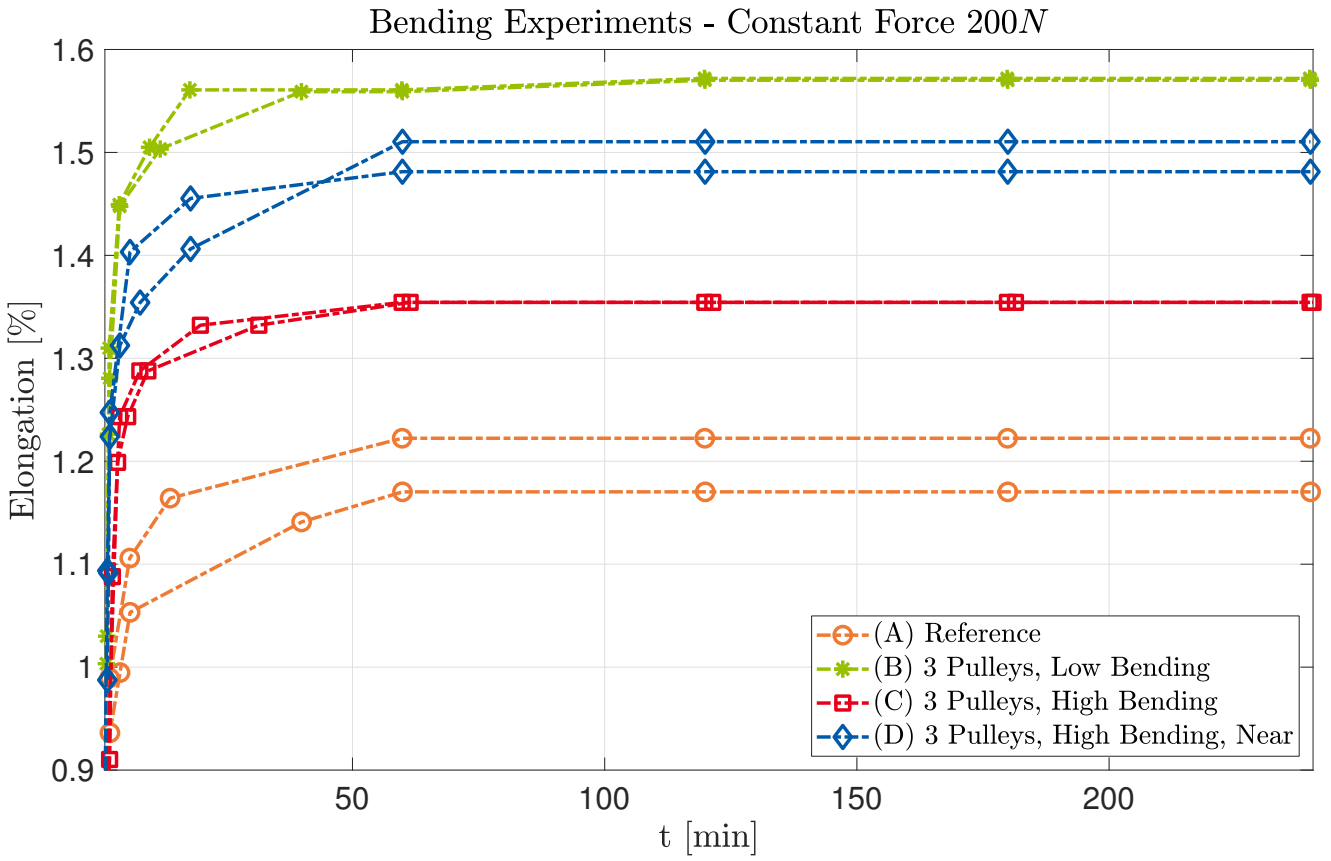

Figure 5.4.: Elongation results of the bending experiments exerting a constant force of 200 N to the ropes during 240 min. Each experiment is performed two times (same line color).

with again distinct stressed rope segments. This is changed in experiment (D). Here, the three guiding pulleys are placed nearby, so that a portion of the rope moves around each pulley. The experiments are performed for four hours, two times each.

During the bending experiments, the *Liros SK99* with commonly available HMPE fiber is used. The determined elongation characteristics are shown in Fig 5.4. As expected, the reference experiment (A) causes the lowest elongation. Surprisingly, experiment (B), containing the lowest rope bending, reaches the highest elongation. Concerning the high bending experiments (C) and (D), one can see that stressing a rope portion more than once with a guiding pulley, results in a higher elongation. The high elongation of experiment (B) could be explained with the low wrap angle at each pulley that also reduces the influence of the rope friction which keeps the rope forces almost unchanged, but additionally, every pulley stresses the braided structure. Analog to the experiments without any bending in the previous chapter, the characteristics asymptotically approach an elongation value over time.

Since in a real robotic system the forces exerted on the ropes are dynamically changing, the rope elongation under changing force is investigated in a basic manner. For this purpose, two experiments were performed with a force of 200 N followed by a reduced force of 120 N pulling at the carriage (E), and vice versa (F). The forces changed after 80 min. The elongation results are shown in Figure 5.5. Two characteristics for HMPE fiber ropes can be observed here. Decreasing the force in experiment (E) leads to a reduction in elongation, but preserving an

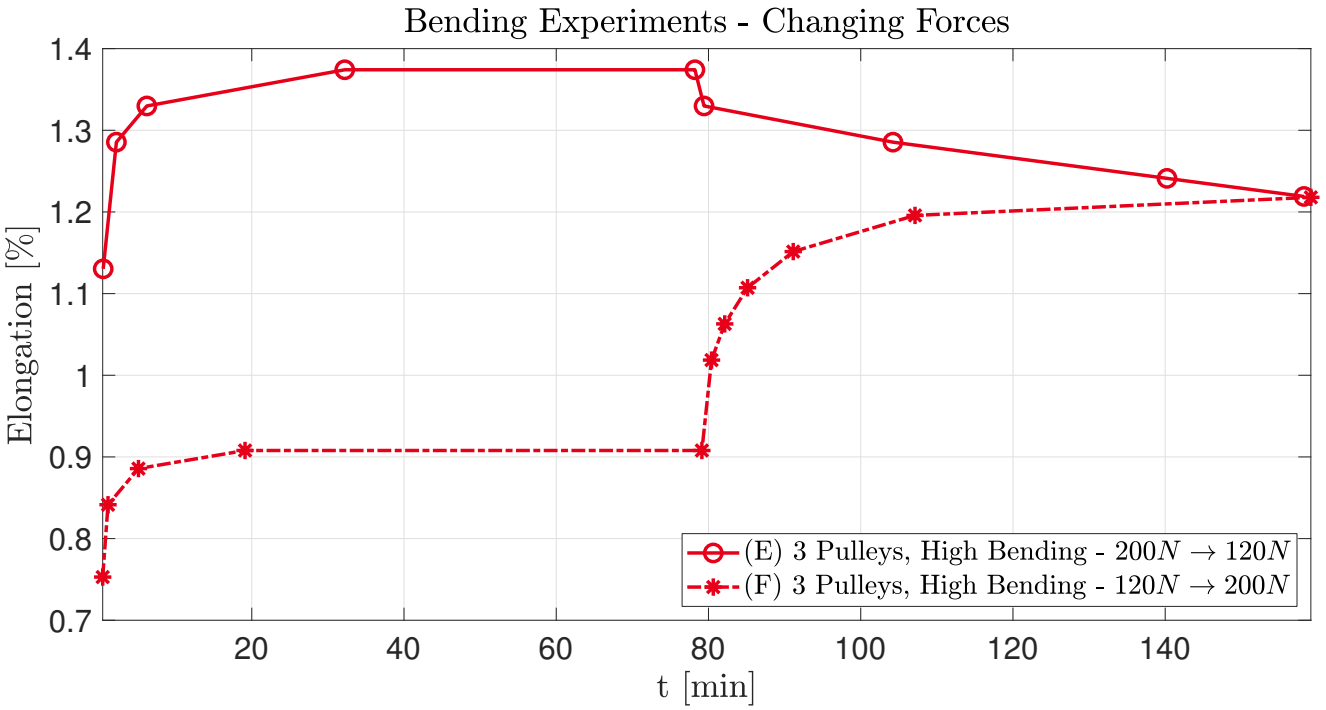

Figure 5.5.: Elongation results of the bending experiments with changing forces from 200 N to 120 N and vice versa. Each force is applied for 80 min.

irreversible elongation. Increasing the force (see experiment (F)) will also increase elongation but during a longer time period.

This investigation makes it reasonable to pretension the ropes according to the typical workload. In this way, one should be able to reduce the effect of elongation. Further, dynamic forces that are higher than the regular workload seems to be at least partially compensated if the force reduces again.

5.4 Tendon Elongation Estimation for Wear Detection

In tendon driven joint elastic ultra lightweight robotic systems, the rope elongation has a crucial influence on the control performance, since the elongation has to be compensated using an appropriate desired motor position to reach the targeted joint position. Further, the long-term elongation information is needed to detect the need of maintenance, e.g., to replace the rope before it breaks. In this chapter a general elongation estimation scheme is presented that only needs the motor and joint position sensor information.

5.4.1 Tendon Elongation Estimation Approach

The reduced dynamics model [127] of a joint elastic robot arm can be represented as:

$$\boldsymbol{M}(\boldsymbol{q})\ddot{\boldsymbol{q}} + \boldsymbol{C}(\boldsymbol{q},\dot{\boldsymbol{q}})\dot{\boldsymbol{q}} + \boldsymbol{g}(\boldsymbol{q}) + \boldsymbol{\tau}_{f,j} = \boldsymbol{\tau}_{el} + \boldsymbol{\tau}_{ext} \tag{5.1}$$

$$\boldsymbol{I}_m\ddot{\boldsymbol{\theta}} + \boldsymbol{\tau}_f + \boldsymbol{\tau}_{el} = \boldsymbol{\tau}_m \tag{5.2}$$

$$\boldsymbol{K}(\boldsymbol{\theta} - \boldsymbol{q}) = \boldsymbol{\tau}_{el} \tag{5.3}$$

with the joint positions $\boldsymbol{q} \in \mathbb{R}^N$, its time derivatives $\dot{\boldsymbol{q}}$ and $\ddot{\boldsymbol{q}}$, the motor position $\boldsymbol{\theta} \in \mathbb{R}^N$ and acceleration $\ddot{\boldsymbol{\theta}}$, the mass matrix $\boldsymbol{M} \in \mathbb{R}^{N\times N}$, the matrix $\boldsymbol{C} \in \mathbb{R}^{N\times N}$ of the centrifugal and Coriolis term, the gravity torque vector $\boldsymbol{g} \in \mathbb{R}^N$, the elastic joint torque vector $\boldsymbol{\tau}_{el} \in \mathbb{R}^N$, the external disturbance torque vector $\boldsymbol{\tau}_{ext} \in \mathbb{R}^N$, the drive train friction vector $\boldsymbol{\tau}_f \in \mathbb{R}^N$, the joint friction vector $\boldsymbol{\tau}_{f,j} \in \mathbb{R}^N$, the motor torque vector $\boldsymbol{\tau}_m \in \mathbb{R}^N$, the diagonal motor and gear inertia matrix $\boldsymbol{I}_m \in \mathbb{R}^{N\times N}$, the diagonal elastic transmission stiffness matrix $\boldsymbol{K} \in \mathbb{R}^{N\times N}$, and N being the degree of freedom.

If the tendon elongates, a motor position offset $\boldsymbol{\Delta}_e \in \mathbb{R}^n$ is introduced changing the elastic joint torque estimation to

$$\hat{\boldsymbol{\tau}}_{el} = \boldsymbol{K}(\underbrace{\boldsymbol{\theta} + \boldsymbol{\Delta}_e}_{\hat{\boldsymbol{\theta}}} - \boldsymbol{q}), \tag{5.4}$$

with $\hat{\boldsymbol{\theta}}$ being the measured motor position including the position offset.

As the elongation increases during the lifetime of the rope, the estimated joint torque increases as well (see (5.4)). In order to realize an accurate control performance, the control approach presented in [77] can be used. Besides the control performance, also the physical interaction is negatively influenced by an incorrect joint torque estimation, since the estimation of external torques based on the dynamics model ([26], [29]) deviates from the real torque.

If the system is equipped with a joint torque sensor, this information can be used to compute the position offset term caused by the tendon elongation using (5.3) and (5.4)

$$\boldsymbol{\theta} = \boldsymbol{\tau}_{el} \cdot \boldsymbol{K}^{-1} + \boldsymbol{q} \tag{5.5}$$

$$\boldsymbol{\Delta}_e = \hat{\boldsymbol{\theta}} - \boldsymbol{\theta}. \tag{5.6}$$

Kinematic coupling effects, introduced by the tendons guided through multiple joints, have to be regarded in (5.5). According to the defined coupling matrix $\boldsymbol{J}_c$, the motor position computation results in

$$\boldsymbol{\theta} = \boldsymbol{\tau}_{el} \cdot \boldsymbol{K}^{-1} + \boldsymbol{q} - \boldsymbol{J}_c{}^{-1}\boldsymbol{q}.$$

In the case of no direct joint torque sensing, a model-based estimation can be done based on the motor dynamics (5.2) or rigid body dynamics (5.1) like in [37] for joint stiffness estimation. The drive train friction of tendon driven robots is hard to model and identify because of the load dependency and absence of joint torque sensing, thus, an observer-based approach as in [82] is not applicable. So, the elastic joint torque estimation based on the motor dynamics that needs friction information is not regarded here.

Inspired by [26] and [37], the robot's rigid body dynamics and the generalized momentum can be used alternatively. Using (5.1) and a stable, first order low-pass filter leads to the elastic joint torque observer

$$\boldsymbol{\tau}_{el} = \boldsymbol{K_I}\left(\boldsymbol{p} - \int_0^t (\boldsymbol{\tau}_{ext} + \boldsymbol{\alpha}(\boldsymbol{q}, \dot{\boldsymbol{q}}) + \boldsymbol{\tau}_{el})dt\right) \tag{5.7}$$
$$\boldsymbol{\alpha}(\boldsymbol{q}, \dot{\boldsymbol{q}}) = \boldsymbol{C}(\boldsymbol{q}, \dot{\boldsymbol{q}})^T\dot{\boldsymbol{q}} - \boldsymbol{g}(\boldsymbol{q}) - \boldsymbol{\tau}_{f,j}$$

with the positive diagonal matrix $\boldsymbol{K_I} \in \mathbb{R}^{N\times N}$ that determines the filter's reactivity and the generalized momentum $\boldsymbol{p} = \boldsymbol{M}(\boldsymbol{q})\dot{\boldsymbol{q}} \in \mathbb{R}^N$.

Using the equations (5.7), (5.5) and (5.6), one obtains an estimation of the position offset $\hat{\boldsymbol{\Delta}}_e \in \mathbb{R}^N$ that is caused by the tendon elongation. If the external forces are not known, the position offset is overestimated. This has to be regarded if the estimation is used for wear analysis.

5.4.2 Experimental Evaluation of Tendon Elongation Estimation

In order to evaluate the capability of the proposed tendon elongation estimation, experiments in simulation and with a real robot have been performed. The elongation position offset Δ_e is added to the real motor position θ if the position is larger than Δ_e and zero otherwise, to simulate the tendon elongation. Additionally, the influence of inaccuracies in the spring stiffness coefficient and the dynamics model are regarded. For the robot experiments, the ultra lightweight tendon driven series elastic *BioRob* is used.

The elongation position offset estimations are depicted in Figure 5.6 showing the results during a motion of the shoulder joint from zero to 90 ° in four position steps. First, only a position offset $\Delta_{e,s}$ in the shoulder is present and increased from 0.01 rad to 0.015 rad. Figure 5.6 (top) shows that the estimation is accurate except at the beginning, which is caused by the implementation of the position offset as described in the previous paragraph.

The offset estimations with errors in the shoulder spring stiffness coefficient $\epsilon_{k_{e,s}}$ of 20 % (overestimation) and with 10 % (underestimation) for each dynamics matrix/vector ϵ_{dyn} are shown in in Figure 5.6 (middle) and (bottom). The absolute position offset value is no longer correct. Nevertheless, the proposed estimation is able to estimate the position offset changes accurately (see $\hat{\Delta}_{e,s}$ Difference).

The same motion as in simulation but for the elbow joint has been performed on the *BioRob X5* arm. Since the tendon elongation is not precisely adjustable, it is realized as in simulation by adding the position offset in the elbow $\Delta_{e,e} = 0.01$ rad to the measured motor position. In the joint torque estimation (5.7) the unknown friction torques $\boldsymbol{\tau}_{f,j}$ are set to zero. The results in Figure 5.7 (top) show similar estimation characteristics as in simulation with model errors (Figure 5.6 bottom), but with decreasing tendency. This is caused by an overestimated joint torque (resulting from model inaccuracies), underestimated spring stiffness, or a combination of both in (5.5). Nevertheless, the estimation is able to detect the absolute degradation (Figure 5.7 middle), but with increased noise and oscillation caused by the real sensors and elasticities.

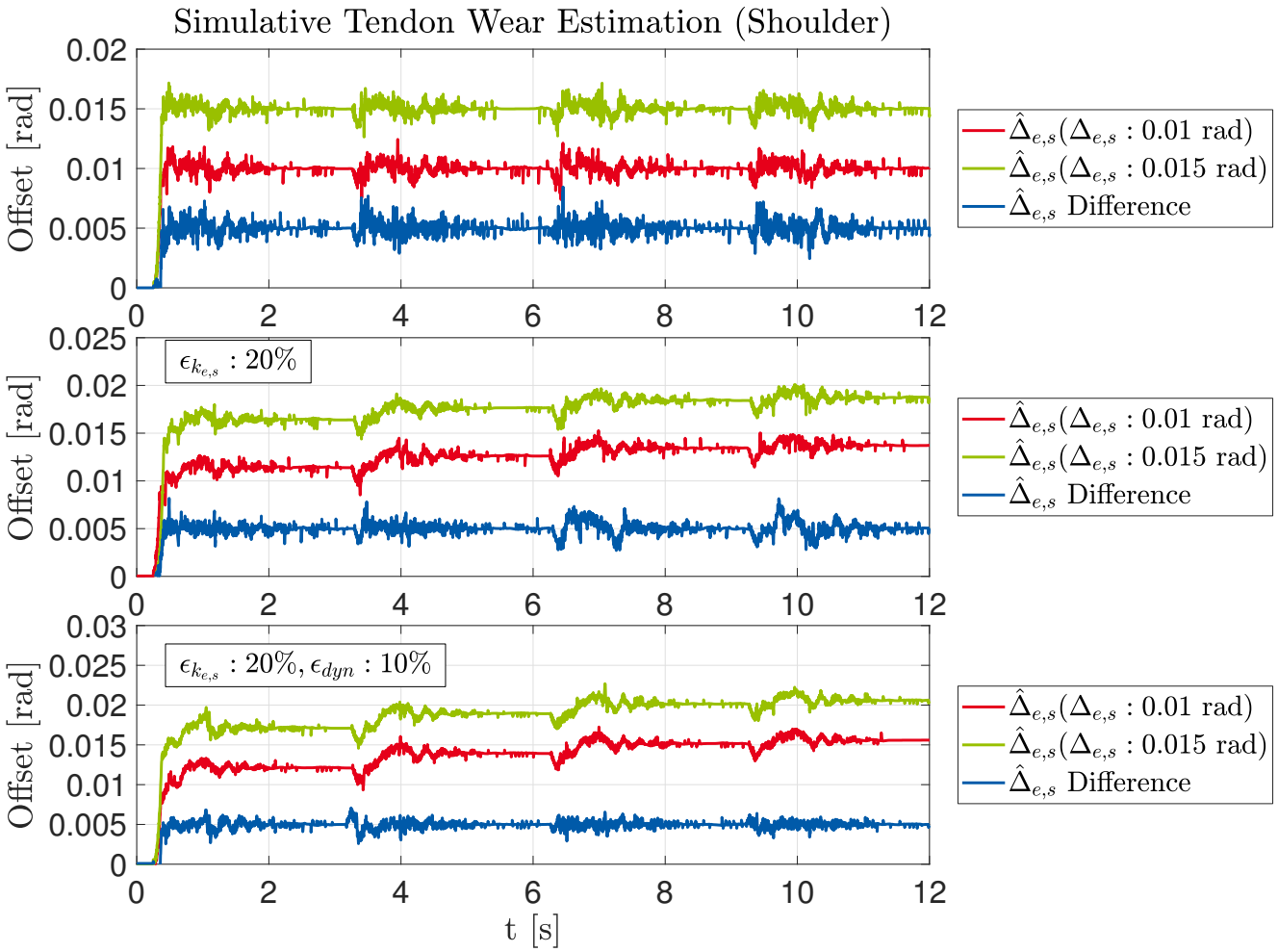

Figure 5.6.: Tendon wear estimation results in simulation estimated as motor position offset with different model errors.

In the second robot experiment, the position offset is introduced by relaxing the rope with the existing rope tensioner by approximately 0.5 mm. The estimation results in Figure 5.7 (bottom) show that the position offset does not start from zero, as expected, and after re-tensioning the rope, the initial estimation is reached again.

The presented evaluation shows that the proposed estimation mechanism is well suited for long-term monitoring of the position offset caused by tendon degradation for quality assurance and to avoid failures.

5.5 Conclusion

The selection of ropes for tendon driven actuation systems is a challenging task because of the variety of possible materials and the absence of detailed characteristics of a specific rope. In this chapter a new comparative evaluation of ropes consisting of the state-of-the-art synthetic fibers in a diameter range from 1.22 mm to 2.05 mm from different manufacturers suitable for use in lightweight tendon driven actuation has been presented. The results show that the rope elonga-

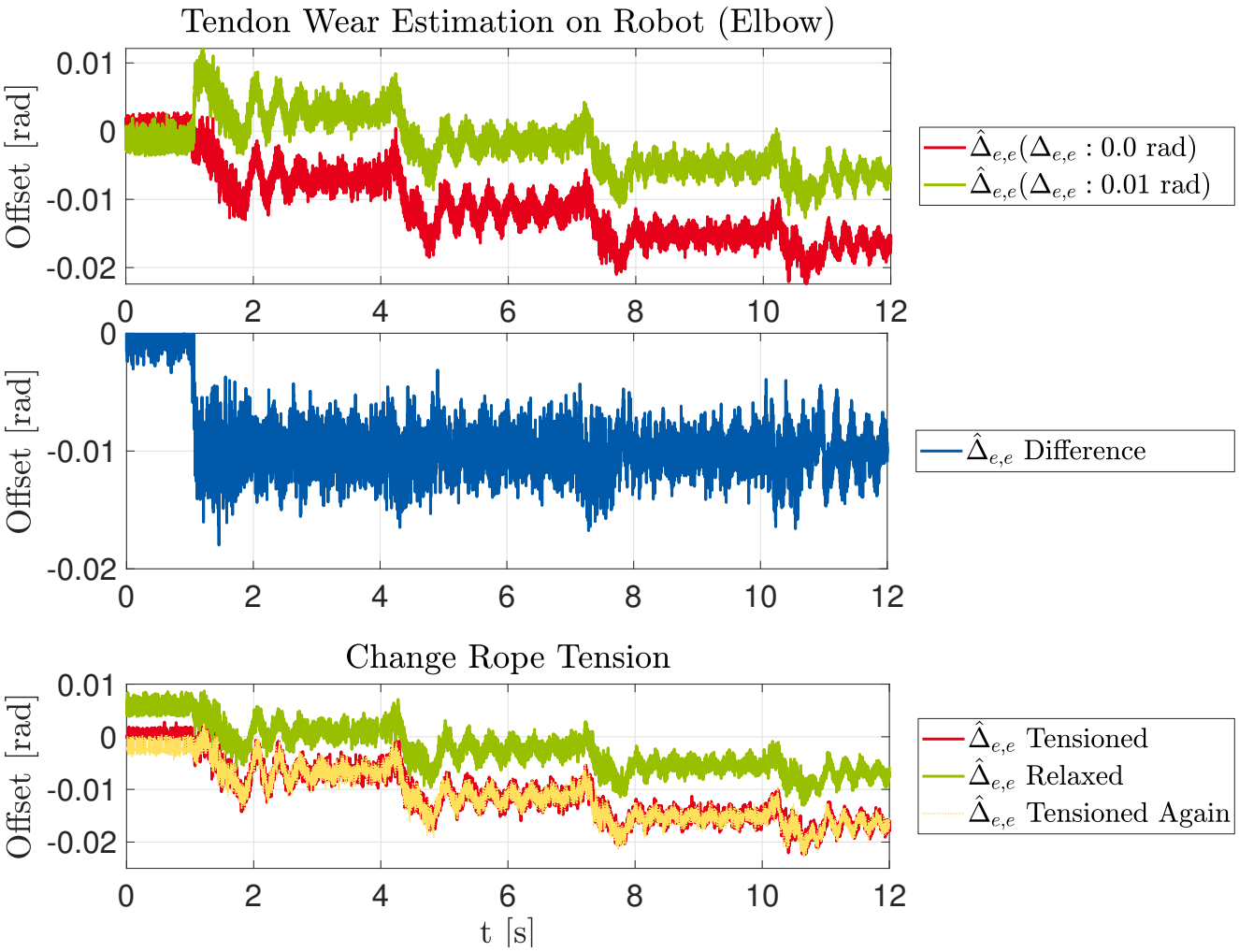

Figure 5.7.: Tendon wear estimation results on Robot, estimated as motor position offset.

tion does not only depend on the fundamental characteristic of the used high-performance fiber, but also on the braiding and production process. An observation, relevant for practical use is that a larger diameter does not necessarily mean a smaller elongation regarding the same rope force. Among the examined ropes, the not commonly used fibers Technora Black and Vectran showed the less elongation slope in the experiment, which is interesting regarding long-term behavior. In case of temperature changes only for the HMPE fiber ropes, changes in the elongation behavior appeared. Hence, the degradation effects, caused by high temperature, depends on the specific HMPE fiber.

Further, the elongation characteristics of a rope, made of the commonly used HMPE fiber readily available on the market, has been investigated during bending experiments with constant and changing forces. It was shown in several general arrangements of guiding pulleys, that redirecting the rope does influence the bending characteristics. Especially, stressing a portion of the rope more than once, or a low wrap angle results in a higher elongation. The elongation behavior at different forces suggests that an appropriate pretension of the ropes can reduce the elongation effects.

The knowledge gained from the performed rope analysis strongly supports the design process of tendon driven robots.

In order to detect the tendon elongation for tendon driven joint elastic robot arms, an observer-based approach has been introduced. This approach does only need motor and joint position measurements and is also able to detect wear in the presence of model errors for quality assurance, thus, avoid failures and increase reliability. The detection performance has been evaluated in simulation and via robot experiments.

6 Trajectory Tracking Control under Uncertain Joint Torque Estimation

A condensed version of this chapter has been presented at the IEEE/ASME International Conference on Advanced Intelligent Mechatronics 2016 [77].

6.1 Introduction

Control of an elastic tendon driven, ultra lightweight robot poses some particular challenges. The lightweight design limits the number of additional sensors used to capture the robot's internal state. Gripping heavy objects, in comparison to the robot's weight, drastically changes the dynamics and the acting friction forces. If the motor position sensors are relative, their zero position can vary after each initialization. Tasks with contacts, where elastic robots are well suited for, have to be regarded to protect the robot's structure and tendons.

The novel control approach presented in this chapter considers the special needs of ultra lightweight elastic tendon driven robots, equipped with motor and joint position sensors. As mentioned in [7], an accurate joint torque value is crucial for controller performance, and its estimation using only position information leads to unsatisfactory results in the presence of model or position errors. Highly accurate robot dynamics models for ultra lightweight tendon driven series elastic arms are difficult to obtain and maintain. Therefore, control approaches are desirable which are robust against changes in model and parameters. This chapter introduces a control approach that is suitable for trajectory tracking, robust against model inaccuracies in the drive train, robot dynamics, and offsets in position sensing. Furthermore, it includes a control torque limitation mechanism to realize safe interaction with the environment.

In more detail, the proposed controller

- contains state feedback with few model dependencies,
- integrates a friction observer [82] in order to enable the use without explicit joint torque measurements,
- is robust against inaccurate initialization of the relative motor sensors, elastic transmission ratios, and stiffness coefficients,
- compensates for changes in robot dynamics by equilibrium controlled stiffness,
- contains a contact mode based on an external torque observer [26], [29] without explicit measurement of the joint torques, to enable contact tasks.

6.2 Related Work

This chapter investigates robotic systems with an open serial kinematic chain and highly elastic joints. The joints are driven by electrical actuators using tendons and a series elasticity in the drive train. In contrast to Series Elastic Actuators (SEA) [115], the spring elongation is estimated using the position difference between reflected motor and joint position and is not directly measured.

Control concepts for tendon driven mechanisms with elasticities, actuated in an antagonistic manner have been described in [70]. Further, the authors in [114] developed a control strategy for compliant and noncompliant antagonistic drives based on the biologically inspired puller-follower concept, regarding gravity compensation.

In order to realize trajectory tracking for robots with elastic joints, first it has to be investigated which sensor data are provided by the robot. If only the motor positions $\boldsymbol{\theta} \in \mathbb{R}^N$ are measurable, as typically the case for industrial robots, a PD control approach can be used as presented in [130], with the motor velocities $\dot{\boldsymbol{\theta}} \in \mathbb{R}^N$ estimated by an appropriate filtered numerical differentiation. The desired motor positions $\boldsymbol{\theta_d} \in \mathbb{R}^N$ can be computed with the reduced dynamics model [127] using the desired joint positions $\boldsymbol{q_d} \in \mathbb{R}^N$, its time derivatives $\dot{\boldsymbol{q}}_{\boldsymbol{d}}$ and $\ddot{\boldsymbol{q}}_{\boldsymbol{d}}$, the diagonal elastic transmission stiffness matrix $\boldsymbol{K} \in \mathbb{R}^{N\times N}$, the mass matrix $\boldsymbol{M} \in \mathbb{R}^{N\times N}$, the matrix $\boldsymbol{C} \in \mathbb{R}^{N\times N}$ of the centrifugal and Coriolis term and the gravity torque vector $\boldsymbol{g} \in \mathbb{R}^N$, as presented in equation (2.5), N being the number of joints.

The dynamics of an elastic joint actuated by an electric motor can be expressed as four first order differential equations, which determines the length of the corresponding state space vector. If the motor and joint positions ($\boldsymbol{q} \in \mathbb{R}^N$) are measurable, one representation of the state space vector is $(\boldsymbol{\theta}, \dot{\boldsymbol{\theta}}, \boldsymbol{q}, \dot{\boldsymbol{q}})^T$. This definition is beneficial in case each joint and motor is equipped with a position sensor since the velocities can be derived from the position measurement by numerical differentiation and an appropriate filter.

Feeding back the above robot state enables control strategies like Feedback Linearization [25]. For both, only motor position measurements and additional joint position measurements, one can add a feedforward term to compensate dynamic effects like gravity [31] or the whole dynamics [30].

If direct joint torque sensing is available, the above mentioned state space vector can be replaced by $(\boldsymbol{\theta}, \dot{\boldsymbol{\theta}}, \boldsymbol{\tau}, \dot{\boldsymbol{\tau}})^T$, with the measured joint torque $\boldsymbol{\tau} \in \mathbb{R}^N$. Control concepts using this information have been developed for robots with flexible joints (e.g., [7], [83], [107], [141] and [96]) to realize torque control, impedance control, and safe human-robot interaction.

Joint torque estimation and further model inaccuracies (e.g., gravity compensation, spring stiffness, unmodeled tendons), can drastically decrease control performance [7] of the mentioned control laws for robots with elastic joints. This motivates the research for a control law that is suitable for the challenges of tendon driven robots, with flexible joints.

The proposed control concept in this chapter can be classified according to [137] as *passive compliant motion* control with *fixed passive compliance*. This classification further can be refined to *passive equilibrium-controlled stiffness* [133], since the equilibrium position of the springs can be changed by adjusting the desired motor position. This exerts a desired force or stiffness

according to the position adjustment which results in a position-control problem instead of a force-control problem.

6.3 Trajectory Tracking for Tendon Driven Robots with Elastic Joints

A control design for tendon driven robots with elastic joints is to be developed that enables trajectory tracking and can handle contact situations. For this purpose, only motor and joint position information are available. The control structure has to be robust against system changes that are not modeled.

The controller's performance is influenced by the accuracy of the modeled system behavior. If the motor position sensors are relative, their position can vary between each initialization. Nevertheless, the trajectory tracking performance should not. Friction forces constitute another crucial performance influence. Especially for lightweight robot arms, high friction forces can drastically increase the time required to fulfill a planned motion. Additionally, load-dependent friction effects are hard to model and to identify. At least if heavy pieces, in comparison to the robot's weight, have to be lifted, the model-based desired motor position computations result in wrong values.

Contact tasks are of special interest. Besides the possibility to define contact forces in the trajectory, the controller should contain a basic contact behavior. The reason for this is, if contact situations are not regarded, the controller, probably designed with integral components, continuously increases the control torque resulting in damages to the environment or the robot's lightweight structure itself.

6.3.1 Approach

In the next sections, the basic state space controller for position control will be introduced that constitutes the starting point of the investigations. It is shown that for good performance various assumptions are made. These assumptions need to be significantly relaxed in the environment of the investigated tendon driven lightweight robot arm, with joint elasticities.

In order to improve the controller's robustness against not modeled or changing friction effects, a friction observer is introduced and it is investigated how it can be used if explicit joint torque measurements are not available. This represents one component of the aimed state space controller.

Since changes in the robot's rigid body dynamics model have to be regarded, the method of equilibrium controlled stiffness is introduced to include the current robot dynamics into the position control law.

Since the estimated joint torque (3.1) is used in both the equilibrium controlled stiffness and the friction observer, the torque limitation is described in the context of the whole controller design.

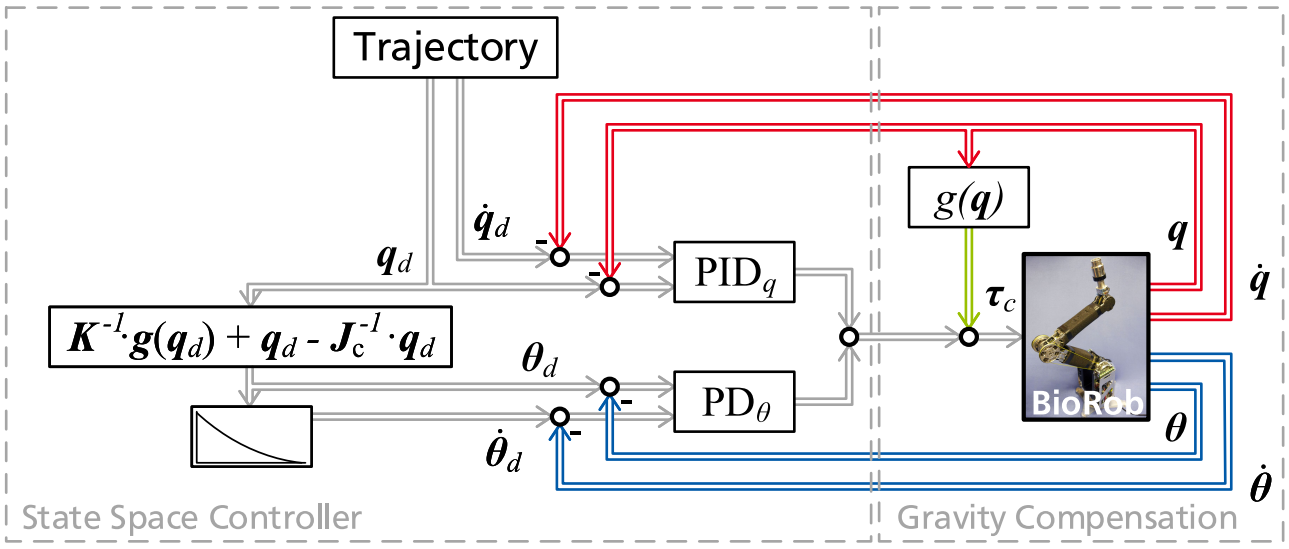

Figure 6.1.: State space controller with feedback of whole robot state $(\boldsymbol{q}, \dot{\boldsymbol{q}}, \boldsymbol{\theta}, \dot{\boldsymbol{\theta}})^T$, desired motor position $\boldsymbol{\theta_d}$ and velocity $\dot{\boldsymbol{\theta}}$ computation, as well as model-based gravity compensation producing the control torque τ_c.

6.3.2 State Space Controller

One possibility to realize a controller with state feedback for trajectory tracking is shown in Figure 6.1. The controller is based on the PD controller described in [130] and extended to a full state feedback controller with state vector $(\boldsymbol{q}, \dot{\boldsymbol{q}}, \boldsymbol{\theta}, \dot{\boldsymbol{\theta}})^T$. The desired motor position is computed according to (2.5), but only using the gravity vector of the desired joint position $\boldsymbol{g(q_d)}$ and regarding the kinematic joint coupling with the coupling matrix J_c^{-1}. In order to get the desired motor velocity, the numerical differences of $\boldsymbol{\theta_d}$ are computed with subsequent low pass filtering. As online gravity compensation, the torques produced by the model-based gravity compensation at the current joint position are added to the control torque. To reduce position overshooting at the target point, the integrational term is activated on arrival at a certain Cartesian position accuracy.

The position accuracy of the state space multiple-input multiple-output controller in Figure 6.1 is limited, because of multiple assumptions that are made:

- All gravity effects can be computed by the gravity torque vector model $\boldsymbol{g(q)}$.
- The joint equilibrium position equals the reflected motor position.
- The elastic tendon transmission is accurately modeled.
- The modeled actuator friction is a close representation of the real friction.
- Aging of the system or the gripping of objects does not change any system parameters.

Even if, e.g., the gravity effort vector, the elastic transmission, or the friction effects can be modeled, these models are often simplifications of the real system behavior with more or less accurate identified model parameters.

In the control structure in Figure 6.1, all deviations from the assumptions made, are compensated by the joint side PID controller. Significant errors in the model for gravity compensation leads to an over- or under-compensation that has to be compensated by other controller components. Errors in the elastic transmission model (e.g., in joint stiffness $\boldsymbol{K}$) result in deviations for the computed desired motor position $\boldsymbol{\theta_d}$. In this case, the motor side PD controller goal differs from the joint side PID controller. If the modeled friction torques are smaller than the real friction torques, the robot only starts moving if the control signal exceeds the friction torques. Model parameter changes caused by aging effects or gripped objects have to be regarded. Motor position initialization errors lead to deviations between the desired motor position and the actually needed motor position.

All these adverse effects on the joint position accuracy can be reduced by increasing the PID controller's proportional and integrational term. Here, the size of the proportional term is limited by system stability. Further, using a high integrational term during trajectory tracking limits the controller's performance because of possible overshooting at the target point and thus long settling time. The proposed control approach in this chapter addresses these effects to provide a robust trajectory tracking.

6.3.3 Joint Torque Estimation Based Friction Compensation

Elastic joint robots with only motor and joint position sensors, as described above, do not have the possibility to measure joint torques directly. The control approach presented in this chapter integrates the friction observer structure presented in [82] for robots with joint torque sensing and adapts it to tendon driven, elastic robotic arms with indirect motor and joint position-based joint torque estimation. The resulting controller structure only needs little model knowledge. This allows coping with effects that are hard to model and to identify, e.g., load-dependent friction effects.

The friction observer is inspired by the momentum-based observer described in [26] and [29] that estimates the torques produced by external forces acting on the rigid body dynamics. Since only the drive train friction is estimated and the (indirectly measured) elastic joint torque represents the robot arm structure dynamics, only the linear actuator dynamics is regarded in the observer. The actuator dynamics for the case of one degree of freedom can be described by

$$\tau_m = I_m \ddot{\theta} + \tau_{el} + \tau_f, \tag{6.1}$$

with motor torque τ_m, motor acceleration $\ddot{\theta}$, motor inertia I_m, elastic joint torque τ_{el} (including visco-elastic effects of the transmission) and friction torque τ_f. Considering (6.1), the observer dynamics can be described by

$$\tau_m = I_m \ddot{\hat{\theta}} + \tau_{el} + \hat{\tau}_f \tag{6.2}$$

$$\hat{\tau}_f = -L I_m \left(\dot{\theta} - \dot{\hat{\theta}} \right), \tag{6.3}$$

with $L > 0$, $\hat{\tau}_f$ friction estimation, $\ddot{\hat{\theta}}$ reflected motor acceleration estimation, and $\dot{\hat{\theta}}$ the estimated reflected motor velocity.

Combining (6.1) with (6.2) and (6.3) shows that the friction is effectively estimated using a first order low-pass filter

$$\hat{\tau}_f = \frac{1}{L^{-1}s + 1}\tau_f,$$

where s is the Laplace operator, and L the reciprocal of the filter's time constant. Finally, the estimated friction can be compensated by simply adding $\hat{\tau}_f$ to the control torque τ_c:

$$\tau_m = \tau_c + \hat{\tau}_f. \tag{6.4}$$

As input, the observer only requires the computed controller torque, the motor velocity, and the measured joint torque.

Since the required joint torques cannot be measured, as done in [82], it has to be investigated how the inaccuracies in the estimated joint torque $\hat{\tau}_{el}$ alter the behavior of the observer. For this purpose, the friction torque estimation is considered after the introduction of an error ϵ. This error represents the inaccuracies in the joint torque estimation $\hat{\tau}_{el}$, computed with (3.1). The friction observer should represent the real actuator dynamics, which leads to the following equation

$$I_m\ddot{\theta} + \tau_{el} + \tau_f = I_m\ddot{\hat{\theta}} + \hat{\tau}_{el} + \hat{\tau}_f$$

Introducing the joint torque estimation error leads to

$$\begin{aligned} &I_m\ddot{\theta} + \tau_{el} + \tau_f = I_m\ddot{\hat{\theta}} + \tau_{el} + \epsilon + \hat{\tau}_f \\ &\Leftrightarrow I_m\left(\ddot{\theta} - \ddot{\hat{\theta}}\right) = \epsilon + \hat{\tau}_f - \tau_f \end{aligned} \tag{6.5}$$

After transformation into Laplace space and subsequently dividing Eq. (6.5) by (6.3), one obtains the filtered friction estimation with

$$\frac{I_m s^2\left(\Theta - \hat{\Theta}\right)}{-LI_m s\left(\Theta - \hat{\Theta}\right)} = \frac{\epsilon + \hat{\tau}_f - \tau_f}{\hat{\tau}_f} \tag{6.6}$$

$$\Leftrightarrow \hat{\tau}_f = \left(\tau_f - \epsilon\right)\frac{1}{L^{-1}s + 1} \tag{6.7}$$

Equation (6.7) shows that the introduction of ϵ also causes an error in the friction torque estimation.

Another observer property concerns its steady state, where the estimated motor acceleration is $\ddot{\hat{\theta}} \stackrel{!}{=} 0$. Then, the observer dynamics (6.2) becomes

$$0 = \tau_m - \tau_{el} - \hat{\tau}_f.$$

Using the estimated friction $\hat{\tau}_f$ for friction compensation as proposed in (6.4) leads to the requirement

$$0 = \tau_c - \tau_{el} \Rightarrow \tau_c \stackrel{!}{=} \tau_{el}. \tag{6.8}$$

Since the control torque τ_c is computed using a model-based gravity compensation, and τ_{el} is estimated according to the transmission model, errors in both models will violate the requirement of (6.8). In this case, the observer will adjust its friction estimation $\hat{\tau}_f$, and thus τ_m, until (6.8) holds. Depending on the model errors, this will lead to a friction compensation in (6.4) acting against the control torque τ_c resulting in an over- or undercompensation, which leads to static position errors.

The two investigated properties lead to the following conclusions that are of special relevance for tendon driven robots with joint elasticities. Errors in joint torque estimation yield to errors in friction estimation. Further, at steady-state, the control torque should equal the estimated joint torque to avoid undesired over or under compensation.

6.3.4 Equilibrium Controlled Stiffness

Besides the control errors introduced by insufficiently modeled friction, inaccurate elastic transmission ratio, joint stiffness, or motor initialization error, and the error in the computation of the desired motor position $\boldsymbol{\theta_d}$ as done in (2.5), negatively influences the control performance. Especially using the inverse dynamics model in the desired motor position computation poses special challenges. These arise because the current joint position, velocity, and accelerations are needed, the dynamics parameters have to be identified, and the gripped object's physical parameters have to be included.

In order to avoid these difficulties, one can benefit from the joint torque estimates. Feedback of the estimated joint torques into the calculation of the desired motor trajectory cancels out most of the joint torque measurement errors described in Section 6.3.2. The resulting feedback controller structure is depicted in Figure 6.2, where the feedback of the estimated joint torque is highlighted in green.

6.3.5 State Space Controller with Friction Compensation

The final controller structure combines different controller components to achieve robustness against the possible model errors discussed in the previous sections. The control error is reduced by a linear control law containing the motor side PD and joint side PD controller. The next step contains the gravity compensation. Here, the estimated and filtered elastic joint torque is used as the compensation value. This enables the usage of the presented friction observer since now requirement (6.8) is met. As described in Section 6.3.3, the friction observer receives the control torque value, the current motor velocity, and the estimated elastic joint torque to

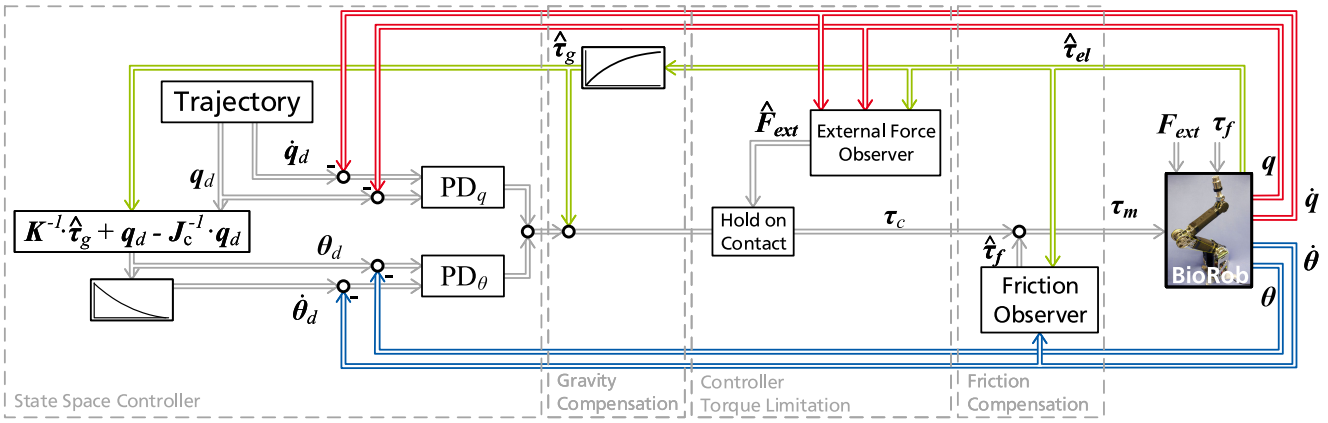

Figure 6.2.: State space controller extended with friction compensation $\hat{\tau}_f$, torque limitation based on external force estimation $\hat{F}_{ext}$ and feedback of estimated joint torque $\hat{\tau}_{el}$ for gravity compensation and equilibrium controlled stiffness.

compute the friction estimation, which is subsequently added to the control torque as friction compensation.

In the case of contacts, feeding back the estimated joint torques to compute the desired motor position results in an equilibrium controlled stiffness that acts into the contact. Thus, the estimated joint torque, as well as the resulting controller torque will further increase and raise the contact force. In order to avoid unwanted damages of the robot and the environment because of the increased contact forces, the disturbance torque observer presented in [26], which estimates the external joint torques $\hat{\tau}_{ext,L}$, can be applied. The subscript L indicates that the observer uses the link side rigid body dynamics. A more detailed description of the observer dynamics is given in Chapter 7.

Limiting the end-effector force is done by first transforming the estimated disturbance torques into operating space using the pseudoinverse of the linear velocity related submatrix of the manipulator Jacobian $\boldsymbol{J}_v$

$$\hat{\boldsymbol{F}}_{\boldsymbol{ext}} = \left(\boldsymbol{J}_v{}^T\right)^+ \cdot \hat{\boldsymbol{\tau}}_{\boldsymbol{ext,L}}. \tag{6.9}$$

The transition between contact and free controller mode is based on the force $\hat{\boldsymbol{F}}_{\boldsymbol{ext}} \in \mathbb{R}^3$. If its norm exceeds a tunable threshold, the portion of the force vector that is needed to comply with this threshold is computed and subtracted from the control torque after transforming into joint space, to keep the control torque $\boldsymbol{\tau_c}$ constant. This alters the behavior of the controller that keeps the contact force constant and thereby protects the robot itself and its environment.

Elastically actuated systems show the effect of oscillations during motions, which have to be damped. This can be achieved with appropriate damping components in the control law. But depending on the velocity estimation phase shift and time lacks of the power electronics in realizing the commanded control signals, this is limited to a certain extent and can even amplify the oscillations. If it is not possible to implement a hardware damping solution, the physical operation of the used DC motor can be used.

As introduced in Chapter 2, each motor's motion induces a velocity dependent voltage u_{ind} that acts against the current rotation. This can be interpreted as the viscous friction that damps the

motion. This counter-electromotive force (EMF) can be compensated during the computation of the control voltage u_c that is applied to the motor according to the control torque τ_c, using the current motor velocity $\dot{\theta}_r$ in

$$u_c = \frac{\tau_c}{z \cdot k_t} \cdot R_a + \dot{\theta}_r \cdot k_v. \tag{6.10}$$

Instead of using the current motor velocity, the desired joint velocity q_d reflected to the motor as the estimation of the motor velocity $\hat{\dot{\theta}}_r = q_r \cdot z$ could be used. This partially compensates the counter EMF and damps oscillations that create velocities that differ from the desired one. This approach is used in the following experiments to compute the control voltages.

6.4 Experimental Control Performance Evaluation

The presented basic and extended controller designs are evaluated by experiments in simulation and with the robot. First, the controller behavior is investigated in simulation, which offers the ability to change model accuracies and compare both controllers. Furthermore, it is possible to simulate contact situations without damaging a real robot.

The first experiment compares both controllers regarding the influence of different model inaccuracies on the joint control error. During the experiment, the robot executes a pick trajectory that simulates gripping of an object with subsequent vertical lifting.

The next experiment investigates the control torque in case of contact. In order to simulate the contact situation, the same pick trajectory as before is executed but with the lower pick position being placed purposely inside the obstacle (e.g., a table).

The next two experiments are executed on the real *BioRob X5* arm. This time, the robot has to pick an object. The object changes the robot's physical dynamics parameters and, thus, the model-based gravity compensation and the desired motor position computation is no longer accurate for the basic state space controller. The performance of both controllers for tracking the same reference trajectory is compared regarding the Cartesian error in the target position (Euclidean norm), as well as execution time till the target point is reached.

Finally, the Cartesian accuracy and overall execution time of a benchmark diagonal Inch-Foot-Inch trajectory are investigated. The planned pick trajectory and Inch-Foot-Inch trajectory can be seen in Figure 6.7.

The controller parameters are tuned for both controllers by experiment based the procedure presented in [139], first for the motor side till good performance is reached, then for the joint side with subsequent manual tuning to regard the influence of the kinematic coupling of the *BioRob X5* arm.

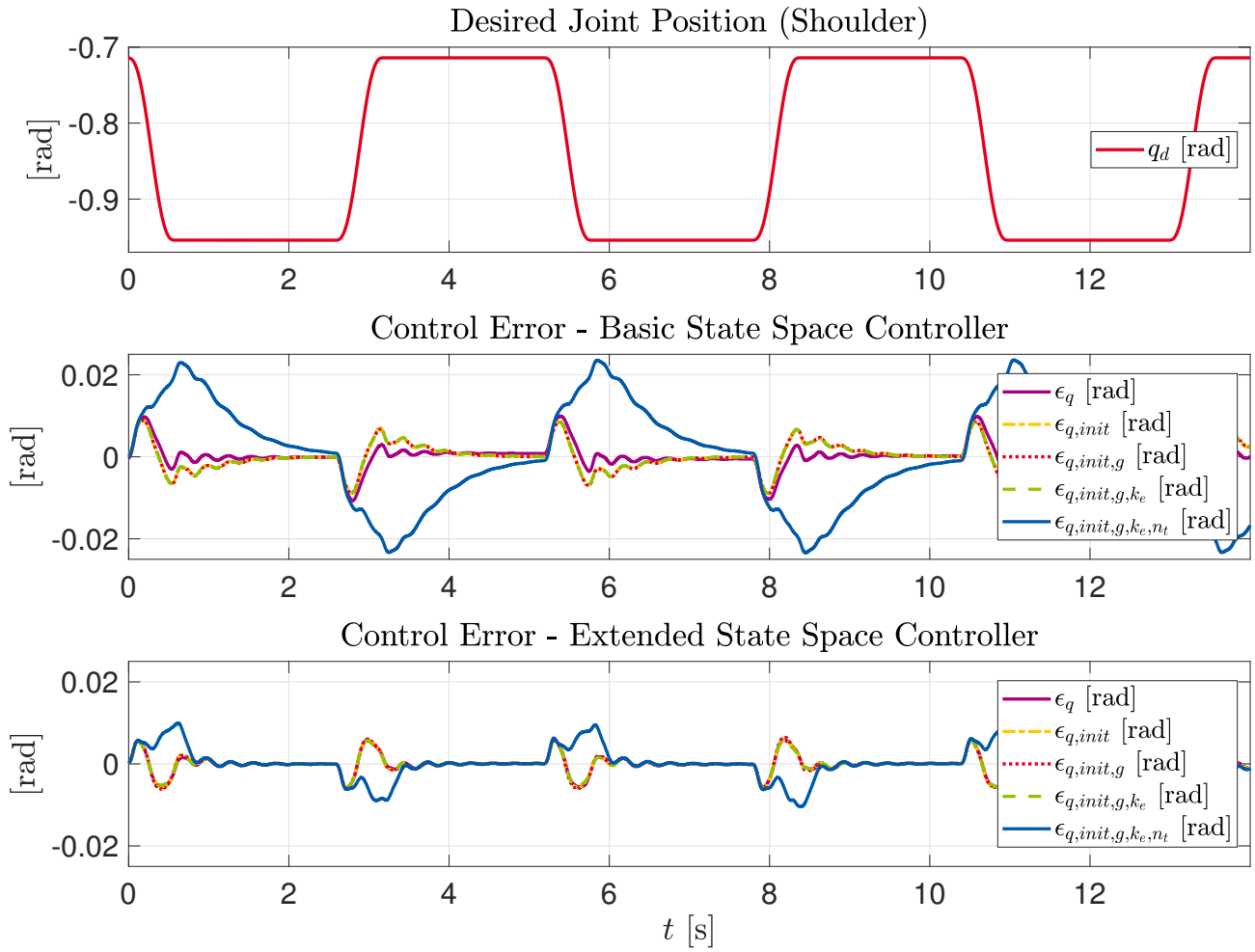

Figure 6.3.: Desired shoulder trajectory q and the resulting control position error containing the various model inaccuracies for the basic state feedback controller with gravity compensation as well as for the extended state feedback controller with friction compensation, equilibrium controlled stiffness and feedback of the estimated elastic torque, executed in simulation.

6.4.1 Evaluation in Simulation Experiments

First a pick motion with 10 cm vertical lift is executed. In order to investigate the influence of possible model inaccuracies, a motor position offset of 2.0 ° is introduced for both controllers, simulating an initialization error (including gear backlash), a gravity torque error of 20 %, a spring stiffness error of 20 % and an elastic transmission ratio error of 20 %, marked in Figure 6.3 with the subscripts $init$, g, k_e, and n_t, respectively.

Regarding the basic state space controller (see Figure 6.3 center plot), all added errors negatively influence the position accuracy. One can observe that the control error slowly diminishes. Especially the elastic transmission ratio model error results in a large control error.

Considering the extended state space controller, the first three model inaccuracies do not increase the joint position error. Solely the elastic transmission ratio model error increases the

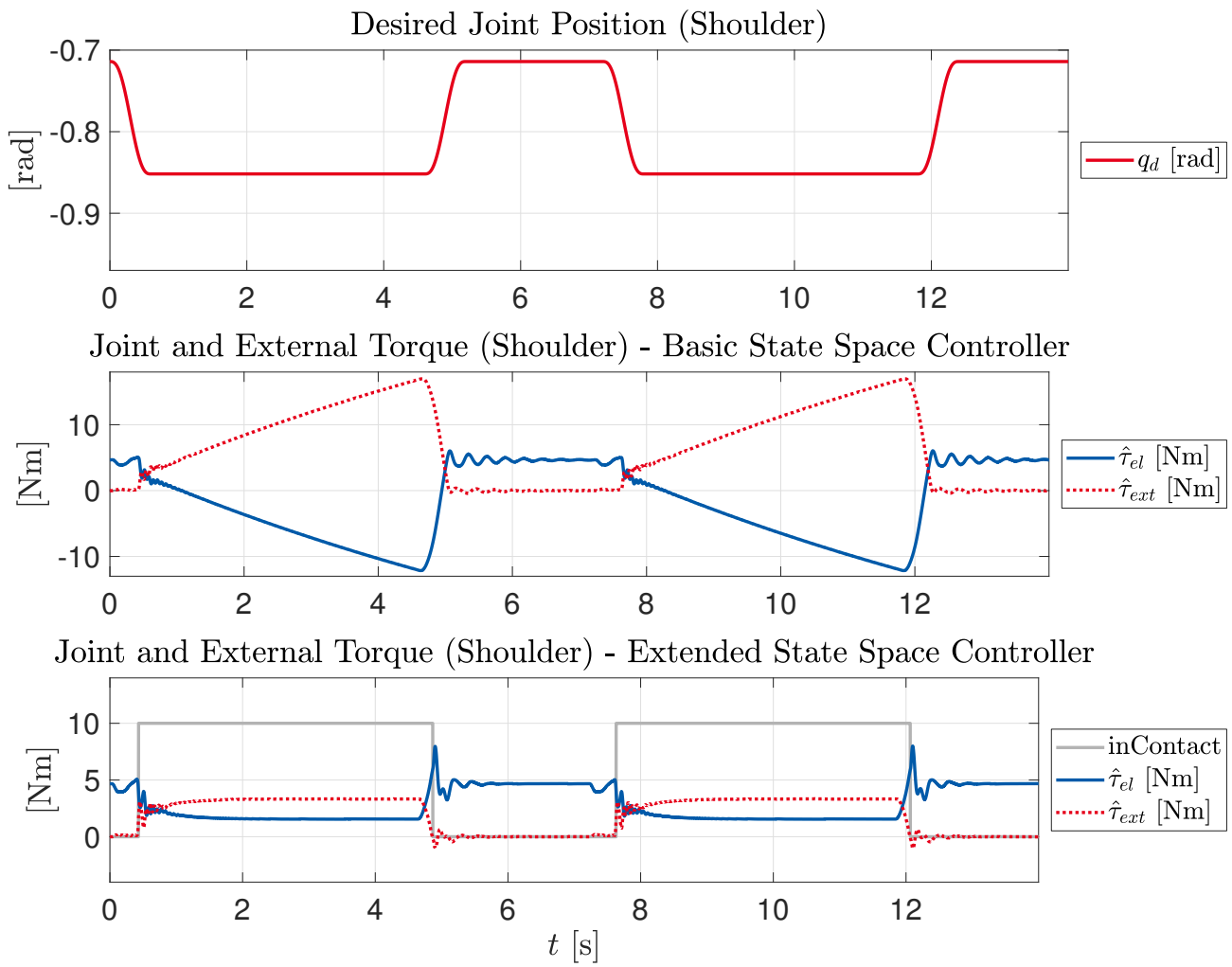

Figure 6.4.: Comparison of the estimated external joint torques $\hat{\tau}_{ext}$ and elastic joint torques $\hat{\tau}_{el}$ of the basic and extended state space controller, executed in simulation. An "inContact" value of 10 indicates that the controller is in contact mode.

control error peak, which is reduced rather immediately, compared to the basic state space controller. In total, the error curves are a bit less oscillating, and the control error is removed faster than with the basic state space controller.

The experiment shows that the proposed controller is only sensitive to elastic transmission ratio errors, since the reflected motor position error increases and thus the estimated joint torque. This will be equalized by the friction observer delayed by its time constant resulting in an overshoot peak.

Repeating the experiments with changing model errors in the ranges $[-20°, 20°]$ for the initialization error, $[-50\,\%, 100\,\%]$ for the gravity torque error, and $[-50\,\%, 100\,\%]$ for the spring stiffness error showed no change of the extended state space control performance. Only the elastic transmission ratio errors again increased the over- or undershoot error, which is canceled out with no static control error.

For the pick trajectory with contact, the lower pick point has been placed 1 cm deep in the ground (e.g., table). Figure 6.4 depicts the estimated external joint torques $\hat{\boldsymbol{\tau}}_{\boldsymbol{ext}}$ from the

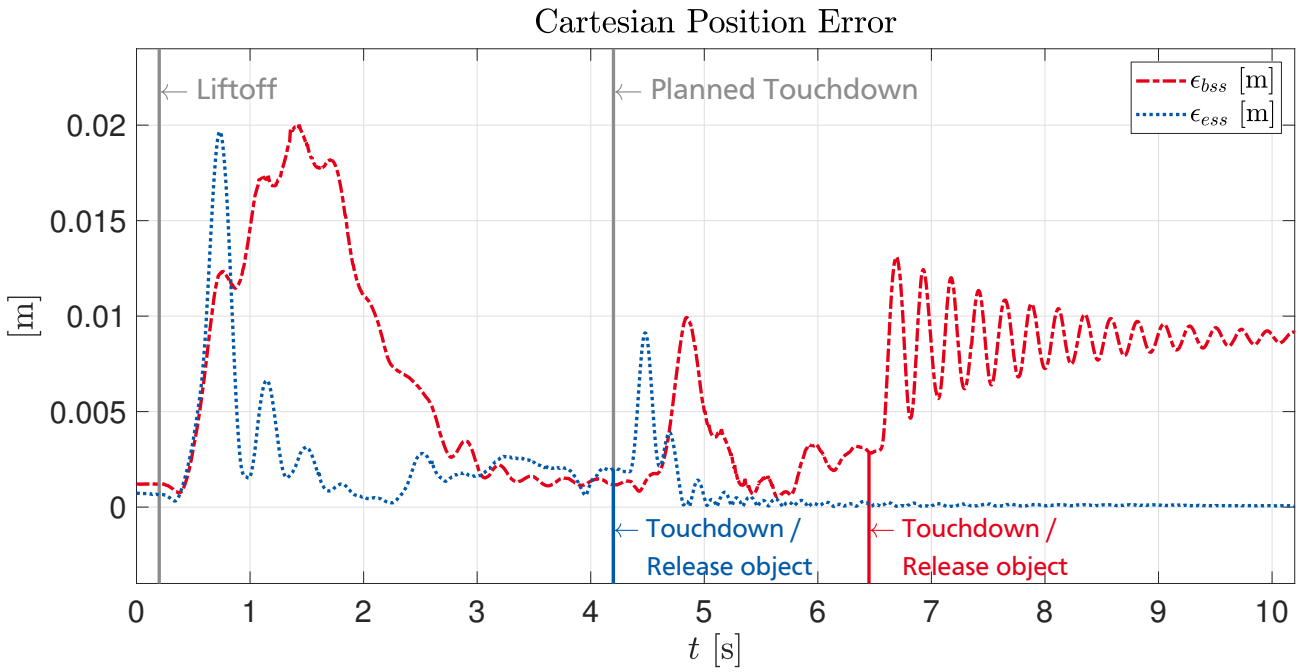

Figure 6.5.: Comparison of the Cartesian position error and execution time of the basic ϵ_{bss} and extended state space controller ϵ_{ess}, while lifting an object weighing 500 g, executed on the real robot.

disturbance observer and the estimated joint torques $\hat{\boldsymbol{\tau}}_{\boldsymbol{el}}$. As expected, the control torque of the basic state space controller continues to increase in contact. In contrast, the new control approach reacts on the estimated external force and keeps the control torque constant during contact. This results in a nearly constant joint torque and thus end-effector force.

6.4.2 Evaluation in Robot Experiments

In order to evaluate the trajectory tracking performance of both controllers, the Cartesian position error computed from the measured and desired joint angles is investigated. In all experiments, the inaccuracies, former artificially introduced in simulation (like initialization error, inaccurate elastic transmission stiffness, and ratio, model-based gravity compensation, and joint torque estimation), are present.

Figure 6.5 shows the Cartesian position error for a lift task. Here, an object of 500 g is picked up from the table, vertically lifted about 15 cm and placed back on the table. The lift and lower motion are planned with a duration of 2 s. The top position has to be reached with an accuracy of about 1 mm, the release position with 3 mm accuracy. The liftoff and planned touchdown times are shown in gray.

The Cartesian errors in Figure 6.5 show, that the extended state space controller (see Figure 6.2) outperforms the basic one. The planned execution time is met (see blue touchdown mark). In contrast to the basic controller, the extended one compensates for the dynamics change caused

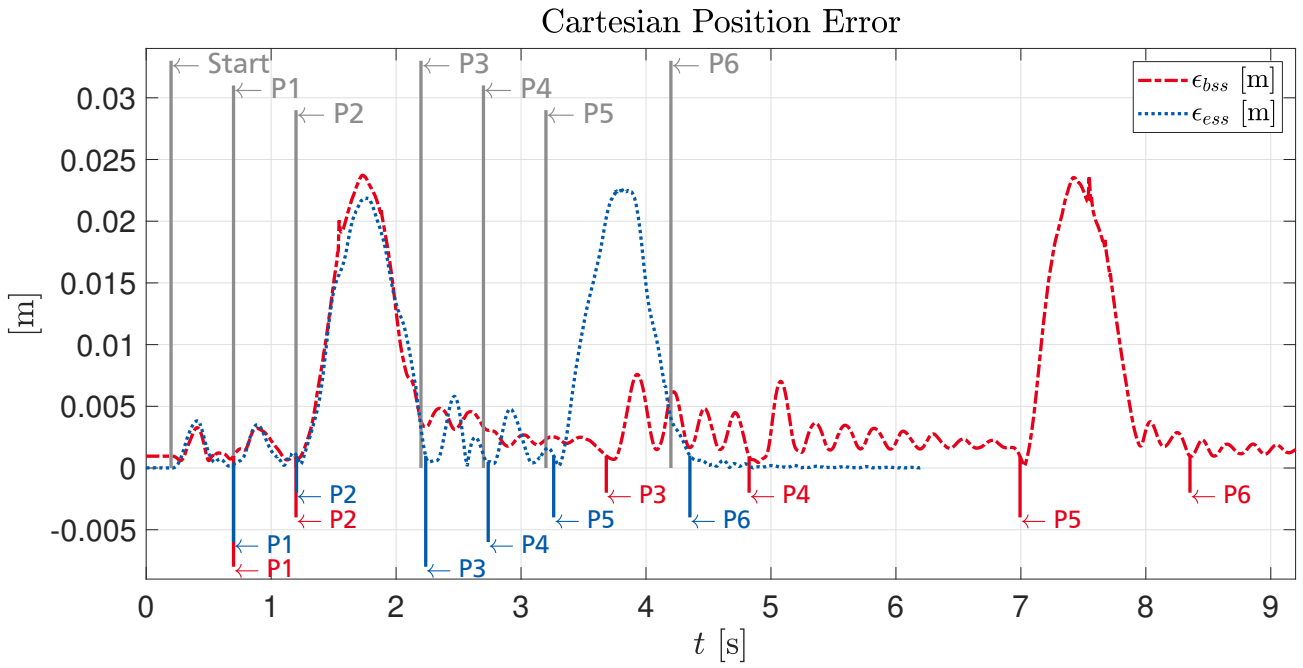

Figure 6.6.: Comparison of the Cartesian position error and execution time of the basic ϵ_{bss} and extended state space controller ϵ_{ess}, during Inch-Foot-inch trajectory execution on the real robot. Marks P1 to P6 indicate the trajectory point's planned (gray) and executed reaching time.

by releasing the object with only a short peak. It rather immediately eliminates the resulting control error.

Similar results can be seen in Figure 6.6 for the Inch-Foot-Inch trajectory. The trajectory is defined with only stop points that have to be reached with an accuracy of 1 mm. As in the previous experiment, the extended state space controller eliminated the position errors at the stop points rather immediately and closely met the planned execution times (indicated by the gray marks). In contrast, the basic state space controller needs more time to reduce the position error caused by model inaccuracies, initialization error, and unmodeled effects till the accuracy threshold is reached. Since the trajectory continues as soon as the trajectory points are reached, this results in longer execution time.

These experiments showed that the presented control approach performs well in trajectory tracking. The planned execution times are almost met. Feeding back the estimated joint torques $\hat{\boldsymbol{\tau}}_{el}$ does not negatively affect the control performance or cause oscillation effects. It instead enables to consider changes in the robot's rigid dynamics. Even in fast pick motions, where torques of dynamic effects partially influence the estimated joint torques, the resulting motion shows only a few oscillations.

6.5 Conclusion

In this chapter, a robust trajectory tracking control approach for tendon driven, ultra lightweight robots with elastic joints has been presented. It does not depend on highly accurate models

of the robot dynamics or the elastic drive train. Furthermore, it only requires the measured angular joint and angular motor position. Explicitly measured joint torques are not available but estimated via the reflected motor and joint position difference and the elastic transmission spring stiffness.

The proposed controller adopts two observer strategies, initially developed on robots with joint torque sensing and only moderate joint elasticity. In addition, it uses the estimated joint torques as feedback information for gravity compensation and equilibrium controlled stiffness. This enables to react to changes in the robot's dynamics caused, e.g., by gripped objects with previously unknown masses.

In order to cope with contact situations, the controller checks the estimated external end-effector force and switches to a contact mode if this force exceeds a user-defined threshold. This contact mode holds the control torque until the contact is released again. Thus, in contrast to a PID controller, the produced joint torques do not continue to increase. This protects the robot's structure as well as the environment, which may include human workmates.

It has been shown in simulation and robot experiments that the proposed controller compensates for the drawbacks of joint torque estimation and is robust against various model inaccuracies. The used friction compensation in combination with the estimated joint torques of the elastic joints acts like an integrational term, improving control performance in accuracy, settling time and oscillation effects. The equilibrium controlled stiffness scheme further enables compensation against dynamics changes introduced by gripped objects.

In order to reduce the influence of noise, the used observers and the fed back estimated joint torques are low pass filtered. The tuned time constant influences the reactivity of the controller. This has to be considered in each specific system.

The considered approach can also be used if one integrates additional elastic joints in the lower arm (yaw rotation) and at the end-effector (roll rotation), equipped with motor and joint position sensors, to create a full 6 DoF robot.

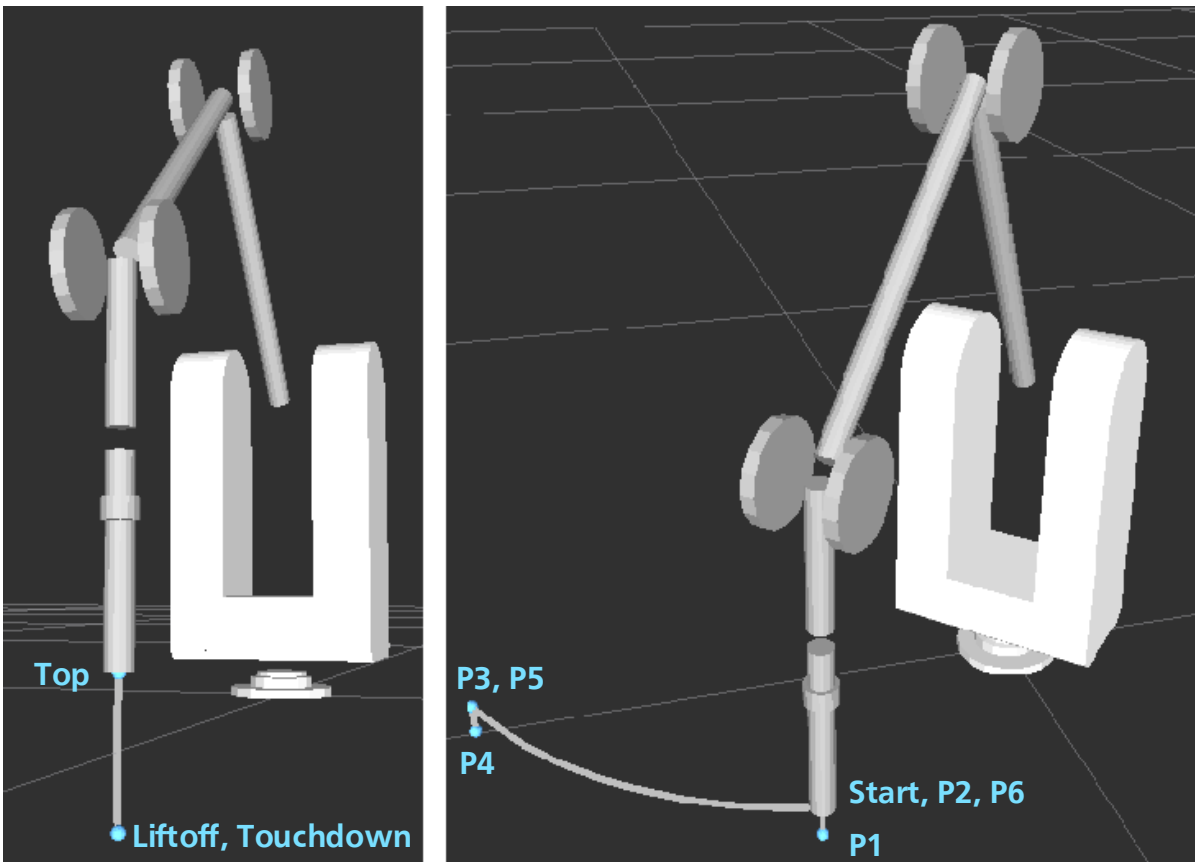

Figure 6.7.: Visualization of the planned pick and Inch-Foot-Inch trajectory, used for experiments.

7 Human-Robot Collaboration under Drive Train Uncertainties

7.1 Introduction

Introducing a human in a robot's environment extends the dependability considerations to include human-robot interactions. Hence, rather than a specific motion execution, the human's safety and the robot's usability stay in focus. To realize this, the interaction of the robot with its environment or a human has to be detected and the behavior appropriately adapted. For this purpose, many different sensors for workspace monitoring and analysis can be used, but a basic interaction detection should also be possible without the need for additional sensors.

Besides the physical interaction, the understanding regarding the performed action of the collaborator is essential to avoid misunderstandings and complete the collaborative task. Perceiving the environment is very challenging for an artificial system like a robot and in many situations only possible to a certain extent. In contrast to this, humans are used to handle situations in unstructured or even unknown environments. In human-robot collaboration, the human partner probably has additional information about the process and a certain experience that can help to solve the task. For this reason, the robot should provide useful information that supports the human during the collaboration to enable smooth operation and increase the human's situation awareness.

This chapter is concerned with human-robot collaboration featuring joint elastic tendon driven robots that are equipped with only motor and joint position encoders. The presented contributions with regards to the capabilities for a transparent interaction are

- the analysis of the disturbance estimation sensitivity on drive train model errors to enable physical interaction sensing,
- a joint space admittance-based approach for teach-in control to facilitate intuitive collaborative task programming,
- a preliminary user study that investigated the influence of various current robot state information visualizations on the user's situation awareness,
- and the definition of metrics in combination with a monitoring approach to trace the robot's health and detect wear in the drive train.

7.2 Related Work and Background

Human-robot collaboration (HRC) takes place each time a common task should be solved by at least one human and one robot. Solving a tasks is a general formulation and can be composed of a variety of different actions. During these actions communication between the collaborators must take place to coordinate the steps needed to reach the task's goal. An overview of the general concepts and mechanisms involved in HRC is given in [11]. It is described that human-robot interaction (HRI) is a general term, which includes collaboration, that describes any action that involves a human or robot, who does not necessarily profit from it. An overview of HRI is given in [43]. In [11] it is further stated, that HRC is an interdisciplinary research area comprising classical robotics, cognitive sciences, and psychology. A common plan is needed to obtain a successful collaboration, that can be created with the joint intentions of all collaborators. Thus, the robot needs to estimate the other's intention, to plan its actions in a way that the common goal (joint intention) is reached. Besides the mechanisms required to perceive, learn, and estimate the intention and creating a joint action, these can be communicated via different ways using, e.g., speech, gestures, actions, haptic signals or physiological signals. A dialog strategy to enable a natural and intuitive interaction in order to achieve a given interaction goal autonomously is presented in [41].

In industrial applications, the environment is typically structured or at least semi-structured. Further, the common goal of the collaborating team is defined by the performed production process. In this scenario, the adaption of the initial robot plan is only necessary, when the process or the human workmate's behavior alters from the intended process. Here, these alterations can lead to undesired collisions with the environment or the need for motion correction. An industrial robot, designed for safe physical HRI, equipped with sensors for contact force estimation, workspace observation, and object recognition is presented in [55]. It implements a behavior that is determined by the sensed environment and distinguishes four different functional modes to realize safe collaboration: autonomous task execution (human absence), human-friendly behavior (human presence), co-worker behavior (human-in-the-loop), and fault reaction behavior (safe fault behavior). In the autonomous task execution, a taught process is performed in a way that the productivity is maximized. An alternative approach for safe HRC based on separation monitoring with real-time human tracking using depth cameras has been presented in [104].

In order to teach the initial execution plan and to collaborate with the robot an appropriate control approach has to be used that allows the physical interaction, that is done based on torque sensing in [55]. For conventional robots, typically force/torque sensors in the wrist are used to solve interaction tasks by force control schemes. In [16] contact force/torque observer approaches were presented for dynamic manipulation tasks that improve the force/torque measurements by considering the dynamic effects of the tool. In [90] the current position and interaction forces are used to estimate the human's intention, based on an unknown limb model that is learned using neural networks, to realize an impedance control for interaction.

In the above examples, the robot adjusts its plan according to the sensed environment, in particular, the human's intention. For this, it is equipped with appropriate sensors. But on the other side, the human should also be able to perceive the robot's intention to check if the common goal is met, especially if the robot autonomously adapts its execution plan. In [33] the benefits from motions that explicitly enables the collaborator only by motion observation, to infer

on the success of the collaboration are investigated. It is suggested that motions that clearly express the robot's intent lead to more fluent collaborations than motions designed to match the human's expectations. In [35] it was investigated, that besides fulfilling the safety needs in HRC, the robotic co-worker must meet the innate expectations of the human, and has to have the ability to communicate its intentions clearly. General principles for efficient HRI concerning information-processing have been presented in [42]. The communication needs for HRC have been reviewed in [46] and the use of augmented reality (AR) has been discussed. It was stated that AR has many benefits with regards to supporting HRC and grounding the communication.

Before using a robotic system for HRC the fundamental collaboration capabilities must be known. The investigated ultra lightweight tendon driven series elastic actuation influences the interaction sensing capabilities of the robot that are essential for collaboration. Moreover, the great human safety potential of a robot arm with this actuation enables the use in a broad spectrum of applications, which therefore emphasize the need for intuitive and direct communication. Thus, the collaboration capabilities regarding physical interaction, state communication for the robot's intention estimation, and wear monitoring to prevent failures and support the human's expectations on the robot's performance are investigated in this chapter.

7.3 Disturbance Torque Estimation

The knowledge about external disturbances during the execution of a motion is crucial for the ability to interact with the environment. These interactions can be very different, for example, detection of undesired collisions, detection if a part is gripped, contacts during peg-in-hole tasks, assembling two parts with a certain force, or interaction gestures during part delivery to a human and so on. In this section, detection of disturbance torques is shortly introduced, and the performance for ultra lightweight robot arms with only position sensing discussed.

7.3.1 Observer-Based Disturbance Estimation

The detection of external forces without additional external sensors like end-effector force/-torque sensors or capacitive skins can be typically made based on certain model information. For this purpose, an approach that uses the robot's rigid body dynamics, the generalized momentum, and a first order filter to compute the disturbance torques in joint space from the measured joint position, velocity, and joint torques only is presented in [26]. The disturbance torque observer dynamics is

$$\boldsymbol{r} = \boldsymbol{K_I}\left(\boldsymbol{p} - \int_0^t (\boldsymbol{\tau_{el}} + \boldsymbol{C}(\boldsymbol{q},\dot{\boldsymbol{q}})^T - \boldsymbol{g}(\boldsymbol{q}) + \boldsymbol{r})dt\right) \coloneqq \hat{\boldsymbol{\tau}}_{\boldsymbol{ext,L}} \tag{7.1}$$

with $\boldsymbol{K_I} \in \mathbb{R}^{N\times N}$ the diagonal matrix containing the reciprocal of the filter's cut-off frequency for each joint. The generalized momentum and its time derivative of the robot's rigid body dynamics follows from the Newtonian mechanics as

$$\begin{aligned} \boldsymbol{p} &= \boldsymbol{M}(\boldsymbol{q})\dot{\boldsymbol{q}}, \\ \dot{\boldsymbol{p}} &= \frac{d}{dt}\left(\boldsymbol{M}(\boldsymbol{q})\right)\dot{\boldsymbol{q}} + \boldsymbol{M}(\boldsymbol{q})\ddot{\boldsymbol{q}} = \dot{\boldsymbol{M}}(\boldsymbol{q})\dot{\boldsymbol{q}} + \boldsymbol{M}(\boldsymbol{q})\ddot{\boldsymbol{q}}, \end{aligned} \tag{7.2}$$

with the mass matrix $\boldsymbol{M}(\boldsymbol{q}) \in \mathbb{R}^{N\times N}$, as well as the joint position, velocity and acceleration $\boldsymbol{q}, \dot{\boldsymbol{q}}, \ddot{\boldsymbol{q}} \in \mathbb{R}^N$ respectively. The skew symmetric property of the mass matrix can be used to compute the time derivative as

$$\dot{\boldsymbol{M}}(\dot{\boldsymbol{q}}) = \boldsymbol{C}(\boldsymbol{q}, \dot{\boldsymbol{q}}) + \boldsymbol{C}(\boldsymbol{q}, \dot{\boldsymbol{q}})^T, \tag{7.3}$$

with the Coriolis matrix $\boldsymbol{C}(\boldsymbol{q}, \dot{\boldsymbol{q}}) \in \mathbb{R}^{N\times N}$. Incorporating the disturbance torques in the dynamics equation for the later observation purpose, the rigid body dynamics becomes

$$\boldsymbol{M}(\boldsymbol{q})\ddot{\boldsymbol{q}} + \boldsymbol{C}(\boldsymbol{q}, \dot{\boldsymbol{q}})\dot{\boldsymbol{q}} + \boldsymbol{g}(\boldsymbol{q}) = \boldsymbol{\tau}_{el} + \boldsymbol{\tau}_{ext}. \tag{7.4}$$

Solving equation (7.4) for $\boldsymbol{M}(\boldsymbol{q})\ddot{\boldsymbol{q}}$ and subsequently insertion with (7.3) in (7.2) leads to

$$\dot{\boldsymbol{p}} = \boldsymbol{\tau}_{el} + \boldsymbol{\tau}_{ext} - \underbrace{\left(-\boldsymbol{C}(\boldsymbol{q}, \dot{\boldsymbol{q}})^T + \boldsymbol{g}(\boldsymbol{q})\right)}_{\alpha(\boldsymbol{q}, \dot{\boldsymbol{q}})}, \tag{7.5}$$

which can be used to compute the external disturbances

$$\boldsymbol{\tau}_{ext} = \dot{\boldsymbol{p}} - \boldsymbol{\tau}_{el} + \alpha(\boldsymbol{q}, \dot{\boldsymbol{q}}). \tag{7.6}$$

Equation (7.6) still contains the time derivative of the generalized momentum $\dot{\boldsymbol{p}}$, thus, needs the joint acceleration $\ddot{\boldsymbol{q}}$ to be computed. This dependency can be resolved by introducing a first-order low-pass filter, with the filter dynamics

$$\dot{\boldsymbol{r}} = \boldsymbol{K}(\boldsymbol{\tau}_{ext} - \boldsymbol{r}). \tag{7.7}$$

Insertion of (7.6) and subsequent integration leads to the final observer dynamics as presented in (7.1), with the generalized momentum assumed as zero at time $t = 0$.

As a variation of the presented disturbance torques estimation, the motor dynamics can be integrated into the observer dynamics. This consideration can be beneficial in the case that no joint torque sensing is available. In this case, the joint torques $\boldsymbol{\tau}_{el}$ can be estimated using the motor dynamics (2.1) extended with the motor and gear friction term $\boldsymbol{\tau}_f \in \mathbb{R}^N$

$$\boldsymbol{\tau}_{el} = \boldsymbol{\tau}_m - \boldsymbol{\tau}_f - \boldsymbol{I}_m\ddot{\boldsymbol{\theta}}. \tag{7.8}$$

Insertion of (7.8) in (7.6) leads to the disturbance observer dynamics that includes both, the motor and link side dynamics

$$\boldsymbol{r} = \boldsymbol{K}_I\left(\boldsymbol{p} + \boldsymbol{p}_M - \int_0^t (\boldsymbol{\tau}_m - \boldsymbol{\tau}_f + \boldsymbol{C}(\boldsymbol{q}, \dot{\boldsymbol{q}})^T - \boldsymbol{g}(\boldsymbol{q}) + \boldsymbol{r})dt\right) := \hat{\boldsymbol{\tau}}_{ext,ML}, \tag{7.9}$$

with the generalized momentum of the link $\boldsymbol{p} = \boldsymbol{M}(\boldsymbol{q})\dot{\boldsymbol{q}}$ and motor inertia $\boldsymbol{p}_M = \boldsymbol{I}_m\dot{\boldsymbol{\theta}}$, regarded zero at time $t = 0$.

Since both approaches depend on the robot's rigid body dynamics model in the same manner, the estimation accuracy is discussed according to the remaining input data. Apart from the dynamics model, only the joint torques are needed in (7.1) for the disturbance torque observation, which can be computed either by a joint torque sensor or a model of the elastically coupled drive train (2.3). Hence, the estimation accuracy is determined by the accuracy of the joint torque sensing or estimation. As introduced in Section 3.2, the joint torque estimation in tendon driven joint elastic drive trains with only position sensing, is affected by different uncertainties (see Figure 3.3) for which the impact on the disturbance estimation is unclear.

In order to avoid the accuracy losses generated by uncertain position based joint torque estimations, the actuator dynamics can be used instead in the observer dynamics as shown in (7.9). This introduces the generalized momentum of the motor inertia, the motor torque and the actuator friction torques to the disturbance estimation, which in turn can be erroneous. The influence of the different error sources on the position or motor dynamics based joint torque estimation and, thus, the disturbance torque estimation is discussed in the next section.

7.3.2 Accuracy Limitations due to Drive Train Uncertainties

The influence of the drive train model uncertainties on the disturbance estimation is not instantly obvious. For this reason, a general error term $\boldsymbol{\epsilon}$ is introduced to investigate the resulting estimation accuracy. First, the disturbance torques based on only the link side dynamics $\hat{\boldsymbol{\tau}}_{ext,L}$ and position based joint torque estimation are considered. In the observer definition (7.1), using the generalized momentum and a first order low-pass filter is done to avoid the need for an accurate joint acceleration estimation. Nevertheless, the observed disturbance torques $\hat{\boldsymbol{\tau}}_{ext,L}$ equal the real acting torques $\boldsymbol{\tau}_{ext}$, but with a delay according to the filter's cut-off frequency. Thus, the observer must represent the real link side dynamics in (7.4), which leads to the equivalence of the estimated and the real torques

$$\begin{aligned} \hat{\boldsymbol{\tau}}_{el} + \hat{\boldsymbol{\tau}}_{ext,L} &= \boldsymbol{\tau}_{el} + \boldsymbol{\tau}_{ext} \\ \Leftrightarrow \boldsymbol{\tau}_{el} + \boldsymbol{\epsilon} + \hat{\boldsymbol{\tau}}_{ext,L} &= \boldsymbol{\tau}_{el} + \boldsymbol{\tau}_{ext} \\ \Leftrightarrow \hat{\boldsymbol{\tau}}_{ext,L} &= \boldsymbol{\tau}_{ext} - \boldsymbol{\epsilon} \end{aligned} \tag{7.10}$$

with erroneous joint torque estimation $\hat{\boldsymbol{\tau}}_{el} = \boldsymbol{\tau}_{el} + \boldsymbol{\epsilon}$. This shows, that the disturbance torque estimation accuracy is determined by the joint torque estimation error.

Using the actuator dynamics for disturbance torque estimation $\hat{\boldsymbol{\tau}}_{ext,ML}$, removes the position based joint torque estimation errors but introduces new potential inaccuracy sources if the motor torques $\boldsymbol{\tau}_m$, the friction torques $\boldsymbol{\tau}_f$, or $\boldsymbol{I}_m\ddot{\boldsymbol{\theta}}$ contain errors or are only partially known. Repeating the error consideration with an accumulated error $\boldsymbol{\epsilon}$ resulting from all error sources leads to the following equivalence with the observer representation on the left hand side and the real dynamics on the right hand side

$$\begin{aligned} \boldsymbol{\tau}_m - \boldsymbol{I}_m\ddot{\boldsymbol{\theta}} - \boldsymbol{\tau}_f + \hat{\boldsymbol{\tau}}_{ext,ML} + \boldsymbol{\epsilon} &= \boldsymbol{\tau}_m - \boldsymbol{I}_m\ddot{\boldsymbol{\theta}} - \boldsymbol{\tau}_f + \boldsymbol{\tau}_{ext} \\ \Leftrightarrow \hat{\boldsymbol{\tau}}_{ext,ML} &= \boldsymbol{\tau}_{ext} - \boldsymbol{\epsilon}, \end{aligned} \tag{7.11}$$

Table 7.1.: Error sources and influences of position based joint torque estimation $\hat{\tau}_{el}$ that determines the disturbance estimation error in $\hat{\tau}_{ext,L}$.

Error	Variable	Error unit	Error relation with τ_{el} estimation	Error type
Tendon elongation	ϵ_{tendon}	rad	$\epsilon_{tendon} = \frac{l}{R}$ $\hat{\tau}_{el} = k_e(\theta - (q + \epsilon_{tendon}))$	const.
Pulley ratio	ϵ_{n_t}	-	$\hat{\theta} = \frac{\theta_r}{n_g \cdot (n_t + \epsilon_{n_t})}$ $\hat{\tau}_{el} = k_e(\hat{\theta} - q)$	linear with motor angle
Joint position sensor	$\epsilon_q(q)$	rad	$\hat{q} = q + \epsilon_q(q)$ $\hat{\tau}_{el} = k_e(\theta - \hat{q})$	nonlinear with joint angle
Motor initialization	ϵ_{init}	rad	$\hat{\theta} = \theta + \epsilon_{init}$ $\hat{\tau}_{el} = k_e(\hat{\theta} - q)$	nonlinear with joint angle
Stiffness	ϵ_{k_e}	$\frac{\text{Nm}}{\text{rad}}$	$\hat{k}_e = k_e + \epsilon_{k_e}$ $\hat{\tau}_{el} = \hat{k}_e(\theta - q)$	const.

where the error sign depends on the sum of the particular error sources. Again, it is assumed that the link side dynamics are exactly known since only the errors related to the actuation concept are investigated. In the case of unknown friction the external torque estimation results in

$$\hat{\boldsymbol{\tau}}_{\boldsymbol{ext,ML}} = \boldsymbol{\tau}_{\boldsymbol{ext}} - \boldsymbol{\epsilon} - \boldsymbol{\tau}_{\boldsymbol{f}}. \tag{7.12}$$

In summary, the estimation accuracy of external disturbances depends on the probably inaccurate drive train model and sensor information, but the impact of the particular error on the resulting disturbance estimation $\hat{\boldsymbol{\tau}}_{\boldsymbol{ext,L}}$ or $\hat{\boldsymbol{\tau}}_{\boldsymbol{ext,ML}}$ is not obvious. The investigation above showed that the estimation error in $\hat{\boldsymbol{\tau}}_{\boldsymbol{ext,L}}$ is determined by the error in joint torque estimation, and in $\hat{\boldsymbol{\tau}}_{\boldsymbol{ext,ML}}$ by the actuator dynamics term errors. Concerning this, the possible error sources are listed in Table 7.1 and Table 7.2 and shortly described in the next paragraph. Here, each error influence is regarded separately.

As discussed in Chapter 5, synthetic fiber ropes, that are well suited to be used as tendons in ultra lightweight structures with small pulley radii, show elongation effects according to the applied load, time interval, and temperature. This elongation l results in a larger angle between reflected motor position and joint position and, thus, a joint torque estimation error determined by ϵ_{tendon} multiplied by the spring stiffness coefficient.
In contrast to the motor gear ratio n_g, the transmission ratio n_t of the tendon driven drive train can vary because of changing or inaccurately determined rope diameter. This transmission ratio error ϵ_{n_t} affects the motor position reflection (and its time derivatives) to joint side, producing a linear increasing, motor position dependent position error. This effect is amplified by the typically large gear ratio n_g, which in turn causes large reflected motor position errors and consequently large joint torque estimation errors.

Table 7.2.: Error sources and influences on computation terms in $\hat{\tau}_{ext,ML}$.

Erroneous term	Variable	Error unit	Influence on τ_{el} estimation	Error type
Friction	ϵ_f	Nm	$\hat{\tau}_f = \tau_f + \epsilon_f$	nonlinear with velocity and load
Generalized momentum	ϵ_{n_t}	-	$\dot{p}_r = I_r \cdot \ddot{\theta}_r \quad \hat{z} = (n_g \cdot (n_t + \epsilon_{n_t}))$ $\frac{\hat{\dot{p}}}{\hat{z}} = I_r \cdot \ddot{\theta} \cdot \hat{z} \quad \hat{\dot{p}} = I_r \cdot \hat{z}^2 \cdot \ddot{\theta}$ $\Rightarrow \hat{\dot{p}} = I_r \cdot \hat{z}^2 \cdot \dot{\theta}$	linear with motor velocity
Motor torque	ϵ_{n_t}	-	$\tau_r = \frac{u_c - u_{ind}}{R_a} \cdot k_t \quad u_{ind} = \dot{\theta}_r \cdot k_v$ $\hat{\tau}_m = \hat{z} \cdot (\frac{u_c - u_{ind}}{R_a} \cdot k_t)$ $\hat{z} = (n_g \cdot (n_t + \epsilon_{n_t}))$	lin. with motor velocity and com. voltage

Independent of the transmission ratios, the joint or motor position measurement can directly be influenced by sensor inaccuracies as position dependent errors, for example, the absolute Hall sensors ϵ_q, or motor position offset regarding the equilibrium position because of incorrect initialization of relative motor position encoders ϵ_{init}. These errors result in a joint torque estimation error according to the stiffness coefficient, also producing large estimation errors in case of high stiffness. For all error cases, also the stiffness coefficient itself can be inaccurate or changes over time because of wear-related stiffness changes in the used tendons ϵ_{k_e}.
Whereas the sources and severity of the various errors can be very different and are highly dependent on a particular system, the errors that alter the reflected motor position or joint position values distort the joint torque estimation according to the joint stiffness. Thus, systems with high stiffness are vulnerable to large estimation errors and make higher demands on the tendon driven drive train to diminish the possible errors.

The terms concerning the motor dynamics used in the observer (7.9), can also be error prone but in a more assessable manner. The accurate identification of gear friction effects consists of defining a model that describes the dissipation of motor torques during the transmission through the drive train. For this, one needs the information of the produced motor torque τ_m as well as resulting joint torque τ_{el}. As seen in the Table 7.1 the position based joint torque estimation $\hat{\tau}_{el}$ in elastically tendon driven drive trains has many influences, which make this estimation not reliable to be used for friction identification purpose. To determine the also needed motor torques τ_m, on the opposite side of the drive train, appropriate electric sensors or if not present, the commanded voltage u_c can be used to compute a motor torque estimation (see (3.8)). Thus, the parameter identification capabilities for the drive train or link dynamics model are limited in the considered system, especially if load dependent models (e.g., motor friction) that require accurate joint torque information are needed. Regarding the motor friction, this circumstance introduces a friction error ϵ_f.
For the computation of the motor's generalized momentum in (7.9), the reflected motor velocity, and inertia are necessary. Both can be affected by an inaccurate transmission ratio $\hat{z}$, which leads to incorrect values if the motor moves and vanishes if the velocity reaches zero, leading to an

erroneous generalized momentum estimation $\hat{p}$.
The required motor torque τ_m can be computed using the motor current i_a multiplied by the motor's torque constant k_t, or using the electrical motor equation and the commanded voltage u_c. Both depend on the parameters typically provided in the motor's data sheet, as the torque constant k_t, speed constant k_v, and terminal resistance R_a. Besides the inaccuracies of the motor data parameters, the computed rotor torque has to be reflected to the joint side, which in turn introduces the possible transmission ratio errors.

The accuracy of both external torque observer approaches highly depends on the specific system parameters and acting particular errors and, thus, a general comparison is not clearly possible. However, a basic evaluation regarding the error source that both observers have in common is possible.

7.3.3 Experimental Disturbance Observer Evaluation

In order to give an estimate of the dependability of the produced disturbance estimation, the performance in case of an erroneous pulley transmission ratio n_t is investigated. Both observers depend on this model parameter, hence it is suitable for a comparative performance evaluation in the absence of any further model error. The performed motion consists of two phases. First, the robot is moved to a configuration with the end-effector above a pick position. Here, estimation changes with no external disturbances are investigated. Second, the robot arm is moved down to the pick position, that is placed in an obstacle exerting a limited force on the end-effector. This experiment represents two typical scenarios, with the robot pressing into an obstacle which also can be interpreted as object gripping that changes the robot's dynamics, exerting a specific weight (according to the limited force) at the end-effector.

Contact Simulation

An appropriate contact model has to be determined, before contacts and the resulting forces can be simulated. The simulated contact uses a nonlinear damping model as presented in [97] and will be shortly described in the next paragraph and has also been used in [76] for collision experiments. In contrast to [88], only the contact forces without regarding friction effects are used, because of the focus on disturbance force estimation where the contact friction effects are not relevant.

A basic model for contact force computation is a parallel spring damper

$$F_c = -b_c \dot{x}_p - k_c x_p,$$

with the resulting contact force F_c, the damping coefficient b_c, the spring stiffness k_c, as well as the penetration depth x_p and velocity $\dot{x}_p$. But this basic model has relevant limitations. The first concerns the case when the impact occurs. In contrast to the spring, where the force starts from zero and increases with the penetration depth, the damping part of the model instantaneously

applies a force according to the penetration velocity that equals the relative collision velocity, resulting in a force step in F_c. Second, in the case of dissolving contact, the damping model creates tensile forces that hold the objects together, caused by the switched velocity sign. Thirdly, the coefficient of restitution, that is an intrinsic property of the material depends on the mass of the impacting model but should depend on the impact velocity.

As a solution, the proposed model of Hunt and Crossley [61] can be used. It replaces the linear spring damper with a nonlinear one, resulting in the contact force equation

$$F_c = -(\lambda_c x_p^{n_c})\dot{x}_p - k_c x_p^{n_c}, \tag{7.13}$$

where n_c depends on the surface geometry, and the damping on the penetration depth creating a continuous force evolution with no tensile forces as separation approaches. The parameter λ_c can be computed as in [97] resulting in a velocity-dependent coefficient of restitution.

Simulative Disturbance Observer Comparison

The pick experiment has been performed with the *BioRob* arm, where a transmission ratio error of 1% of the real transmission ratio n_t has been introduced, resulting in a higher transmission ratio value used for estimation than present in the simulated robot. This represents a rope diameter reduction of approximately 0.3 mm in the case of pulleys with a transmission ratio of approximately $n_t = 3.5$ and the resulting reduced transmission ratio $\hat{n}_t \approx 3.538$ ($r = 10.0\,\text{mm}, R = 35.0\,\text{mm}, \hat{r} = 9.85\,\text{mm}, \hat{R} = 34.85\,\text{mm}$). The model (7.13) was used to simulate the contact scenario, with the parameters $n_c = 1$ to simulate a flat surface, $\lambda_c = 5{\cdot}10^3\,\text{Ns/m}^2$ and $k_c = 10^4\,\text{N/m}$.

The disturbance torque estimation results are depicted in Figure 7.1. As one could expect because of the linear transmission ratio error dependency (see Table 7.1 and 7.2), the estimation error during free motion (Figure 7.1 (top)) grows with increasing motor angle. Here, the error influence is significantly higher for the link dynamics based observer $\hat{\tau}_{ext,L}$. In the contact case (Figure 7.1 (bottom)), the significant overestimation of $\hat{\tau}_{ext,L}$ is shown again but increased by the amount of the disturbance torque. In both cases, opposite kinds of estimation errors regarding the estimation error sign are visible. In the case of the link dynamics based observer $\hat{\tau}_{ext,L}$ the external torques are overestimated, whereas underestimated in the case of the motor and link dynamics based observer $\hat{\tau}_{ext,ML}$.

The experiment shows that the disturbance observer (7.1) that depends on the joint torque estimation is highly sensitive to errors in pulley transmission ratio n_t compared to the second observer (7.9). This can be mitigated in the case of lower joint stiffness or transmission ratio. Both are only possible to a certain extent. In the particular case, the joint stiffness should be reduced by an order of magnitude. Alternatively changing the transmission ratio can be limited by the space available for the pulleys and further the radius reduction would lead to higher forces in the tendons.

In conclusion, the link dynamics based observer estimation accuracy mainly depends on the joint torque estimation accuracy. Because of the joint stiffness, even small errors in the joint and

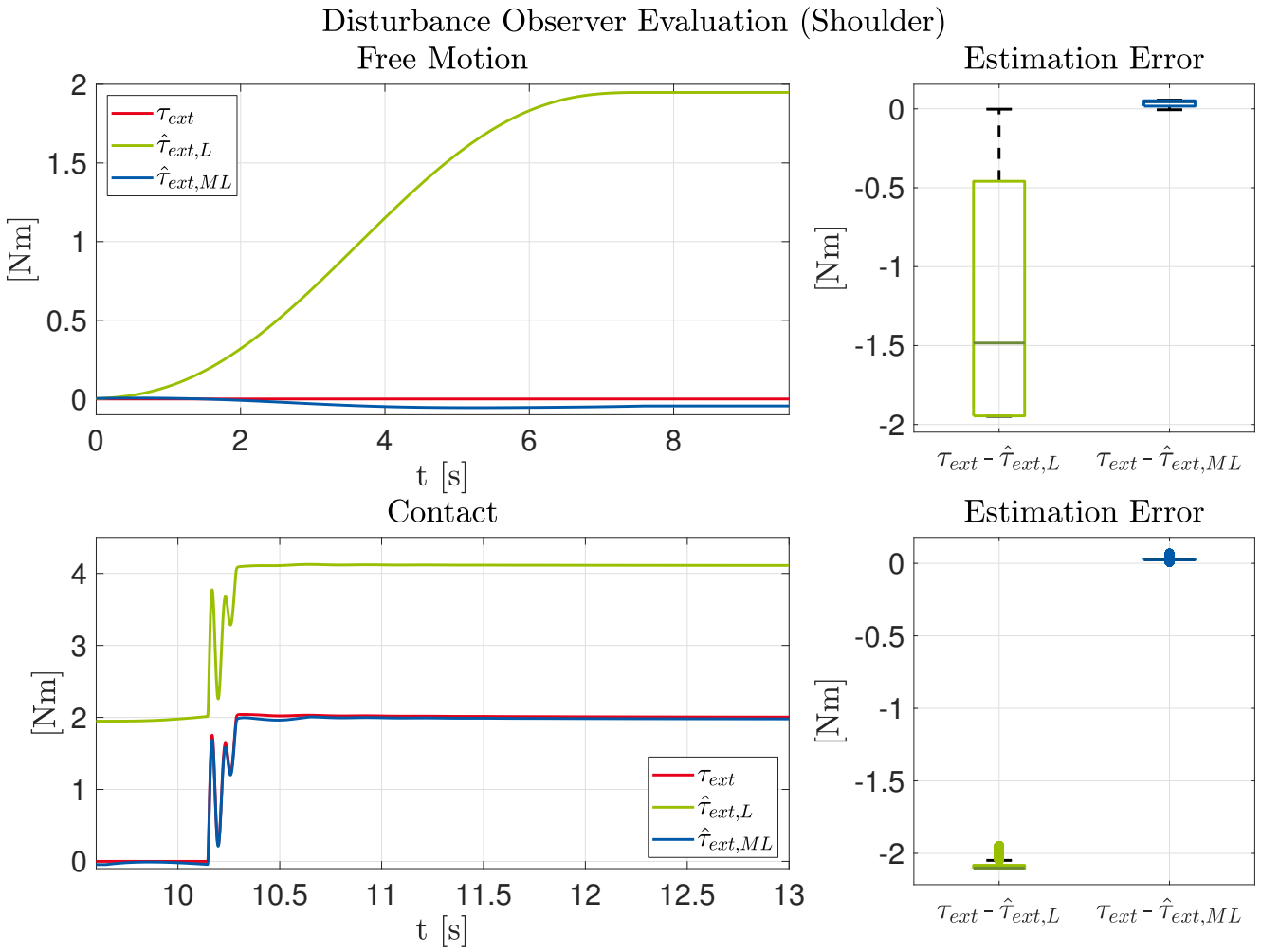

Figure 7.1.: Disturbance observer evaluation during free motion and contact with erroneous transmission ratio n_t of 1 % overestimation in the shoulder joint.

reflected motor position result in large torque estimation errors. If these errors can mechanically be kept small, the observer can serve as a good solution. Besides the transmission ratio, the motor and link dynamics dependent observer also assumes an accurate friction model and motor parameters. Especially an incorrect friction model can result in high estimation errors in the dimension of the friction error.

Robot Collision experiment

The disturbance observer evaluation on real-world data gives insights about the observer applicability beyond the drive train model related considerations made in the previous section. A scenario is regarded in which the end-effector of the *BioRob X5* collides with the hard surface of a force plate. During the motion, the robot arm is stretched out with only the shoulder joint moving at maximum velocity as illustrated in Figure 7.3 (bottom right). The recorded linear collision forces from the force plate $\boldsymbol{F}_{ext} = (F_{ext,x} \;\; F_{ext,y} \;\; F_{ext,z})^T$ have been used to compute a reference signal of the collision torques in joint space, using the transposed Jacobian matrix

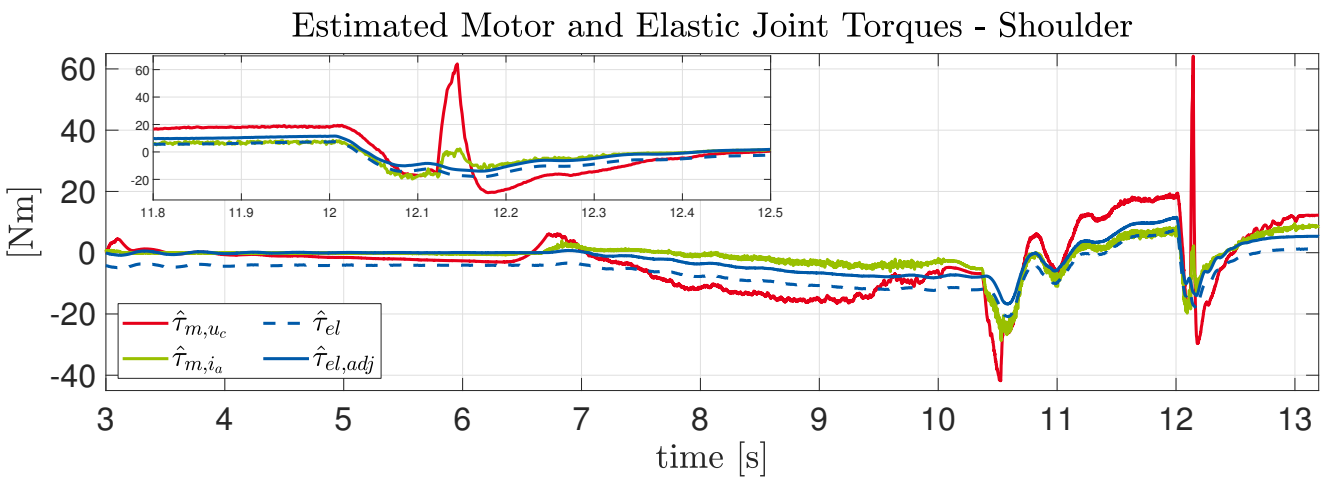

Figure 7.2.: Estimated motor torques computed from commanded voltages $\hat{\tau}_{m,u_c}$ and recorded motor currents $\hat{\tau}_{m,i_a}$, as well as elastic joint torque estimation with ($\hat{\tau}_{el,adj}$) and without ($\hat{\tau}_{el}$) motor position initialization adjustment.

$\boldsymbol{\tau_{ext}} = \boldsymbol{J_v}^T \cdot \boldsymbol{F_{ext}}$. The observers estimated the disturbance torques with a gain factor $K_I = 250.0$ for each joint.

In order to compute the disturbance estimations, the motor and joint positions, as well as the control signal voltages and motor currents have been recorded during the experiment. First, the motor torques, computed using the applied control voltages ($\hat{\tau}_{m,u_c}$) and recorded motor currents ($\hat{\tau}_{m,a_i}$), have been compared. As depicted in Figure 7.2 for the shoulder joint, these values largely differ even during free motion (collision starts at 11.9 s). This indicates that the power electronics used in the *BioRob* arm does not realize the commanded voltages as represented by the motor equation (3.5). Further, the position based elastic joint torque estimation $\hat{\tau}_{el}$ showed an offset resulting from the motor position sensor initialization error. This has been adjusted manually for the experiment to create a more reliable estimation $\hat{\tau}_{el,adj}$. For the following observer evaluation the corrected joint torque estimation $\hat{\tau}_{el,adj}$ and current based motor torque estimation $\hat{\tau}_{m,a_i}$ have been used.

As described in the previous section, an accurate friction torque estimation is necessary to obtain an exact disturbance torque estimation $\hat{\boldsymbol{\tau}}_{\boldsymbol{ext,ML}}$. According to the motor dynamics equation (7.8), the elastic joint torque can be computed using the motor torque $\boldsymbol{\tau_m}$, the torque $\boldsymbol{I_m}\ddot{\boldsymbol{\theta}}$, and the drive train friction $\boldsymbol{\tau_f}$. Regarding this, a friction model had to be determined that results in a comparable joint torque as the estimation $\hat{\boldsymbol{\tau}}_{el}$ computed using the spring stiffness joint and motor position. The identified friction model contains a load dependent (coefficient $F_{L,i}$) part combined with a Coulomb term (coefficient $F_{c,i}$)

$$\tau_{f,i} = F_{c,i} \cdot \mathrm{sgn}(\dot{\theta}_i) + F_{L,i} \cdot \left|\tau_{el,i}\right| \cdot \mathrm{sgn}(\dot{\theta}_i), \tag{7.14}$$

for each joint i. The typically included velocity dependent viscosity term to describe lubricated friction is omitted for simplicity because the effects were not evident in this experiment. The friction torques $\tau_{f,2}$ of the shoulder joint according to the recorded collision experiment values are shown in Figure A.3, illustrating the magnitude for this exemplary case.

The disturbance estimation results are shown in Figure 7.3 and the errors in Table 7.3. During the free motion, the root mean square estimation errors ϵ_{RMS} of $\hat{\tau}_{ext,L}$ are smaller in all joints

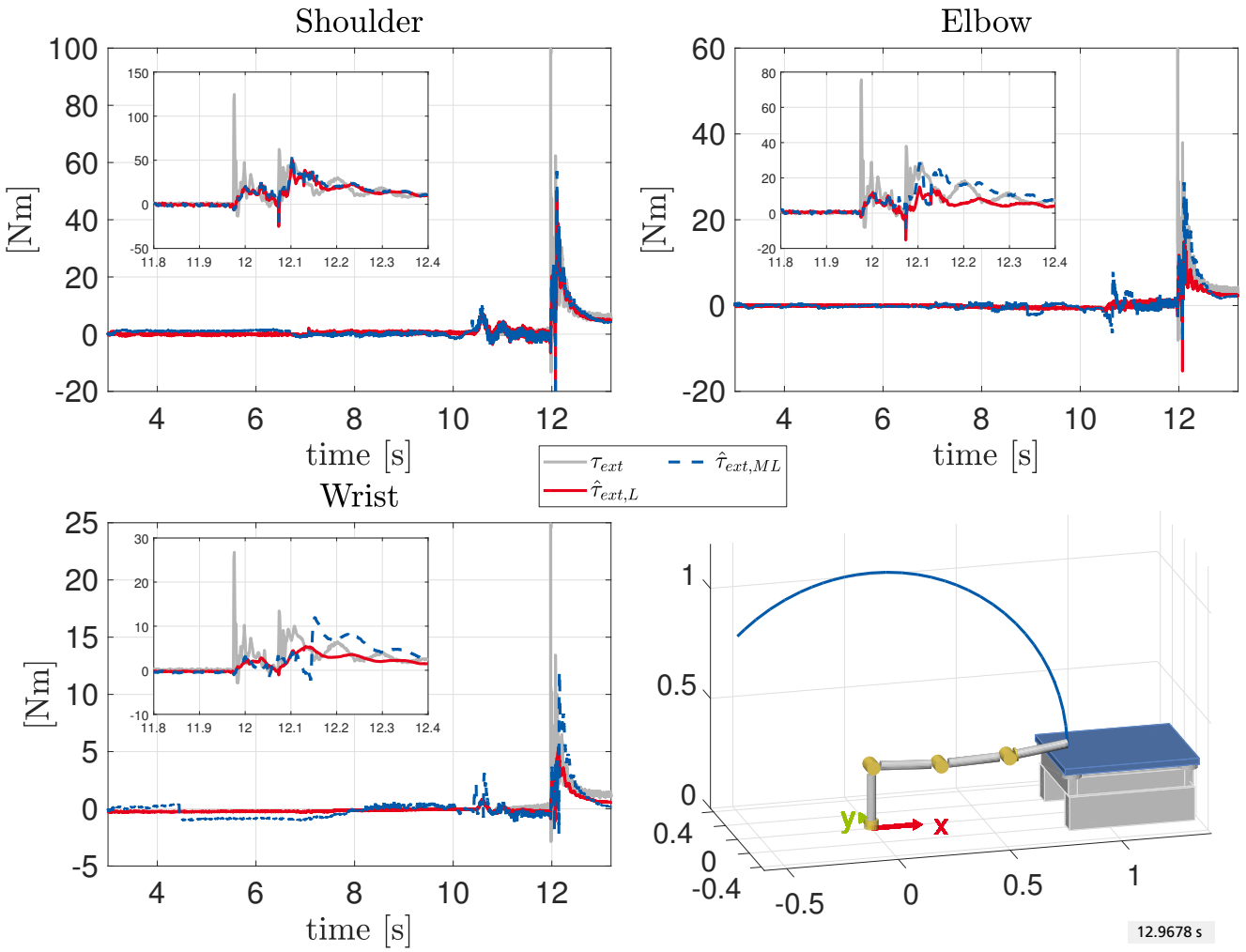

Figure 7.3.: Disturbance torque estimation results during stretched out collision motion at maximum shoulder velocity of load dynamics based $\hat{\tau}_{ext,L}$ and motor and load dynamics based $\hat{\tau}_{ext,ML}$ observer, with reference signal computed from force plate data.

compared to $\hat{\tau}_{ext,ML}$. Especially for the elbow and wrist joint, the estimation $\hat{\tau}_{ext,ML}$ shows peaks, resulting from peaks in the motor current measurements. Regarding the collision case (see close-ups), both signals are rather similar for the shoulder joint. This also holds for the elbow and wrist joint, but only for the first approximately 100 ms. Looking at the reference signal τ_{ext}, computed from the recorded force plate data, the disturbance torque estimations are not able to capture the collision peak torque. This illustrates the elastic joint's low-pass filter property that protects the gear in the collision case.

Reliable collision detection requires avoiding false positive detection that can be realized using a threshold that has to be exceeded before the collision reaction strategy is activated. According to the maximum error $\hat{\epsilon}_{MAX}$ during the free motion, the lower limit for this threshold is comparable for both estimations regarding the shoulder joint, but more than three times as large for $\hat{\tau}_{ext,ML}$ as for $\hat{\tau}_{ext,L}$ in the elbow and wrist joint for this particular motion. Looking at the estimation result without initialization correction $\hat{\tilde{\tau}}_{ext,L}$ shows, that this inaccuracy is only significant in the shoulder joint that can be caused by inaccurate initialization or tendon elongation that introduced backlash.

Table 7.3.: Disturbance estimation error during free motion ($t < 11.9\,\mathrm{s}$).

	Shoulder		Elbow		Wrist	
Estimation	ϵ_{RMS}	$\hat{\epsilon}_{MAX}$	ϵ_{RMS}	$\hat{\epsilon}_{MAX}$	ϵ_{RMS}	$\hat{\epsilon}_{MAX}$
$\hat{\tau}_{ext,ML}$	1.3459	10.0085	0.9558	7.9053	0.6094	3.1157
$\hat{\tau}_{ext,L}$	0.9388	7.3042	0.3711	1.7071	0.2123	0.8339
$\hat{\hat{\tau}}_{ext,L}$	4.5208	11.4234	0.6004	2.2923	0.2150	1.1697

The main observations regarding the estimation $\hat{\tau}_{ext,ML}$ concerns motor control and friction. It has to be ensured that the power electronics accurately realize the control signal (voltage or torque). Otherwise, the motor torque estimation based on the electrical motor model will be faulty. The same accuracy requirements hold for motor current sensing.
Regarding the drive train friction model, another challenge showed up. Bringing the robot's velocity and, thus, possible collision forces in a human-friendly range and simultaneously providing the needed torques is typically done by gears in the drive train. Using small size motors suitable for downscaled cobots with high gear reductions introduces friction effects that show load dependent behavior. In order to accurately model these effects, an accurate joint torque estimation is needed. But this is influenced by multiple errors as described in the previous section. Hence, introducing further estimation errors.
Regarding the estimation results in $\hat{\tau}_{ext,L}$, the initialization error that also could be affected by tendon elongation, should continuously be monitored in order to assess if the collision detection is still valid. If a load dependent friction model is used, this also influences the estimation of $\hat{\tau}_{ext,ML}$. Since the collision torques are typically high in comparison to the estimation errors in free motion, both approaches could be used with an appropriate detection threshold. The decision about the approach that is more suitable for the particular system, can be evaluated regarding the influences and observations made above. In the *BioRob* arm example, the observer (7.1) seems to be preferable because of the large load-dependent friction and inaccurate current measurement.

7.4 Collaborative Task Solving

Combining the robot's and the human's workspace to one common collaborative workspace sets the human safety requirements (already discussed in this work) but also the usability of the robotic system in focus. Since the robot should work with any workmate in an effective and reliable manner, the definition of how the robot's task looks like must be feasible and straightforward for non-expert users. This can be compared with the interaction between two humans, where the supervisor explains the worker the single steps of a task verbally or by demonstration. In this case, the supervisor is the expert concerning the particular process. Transferring this to a robotic workmate requires an interface that enables the supervisor to program the targeted motion and in particular the needed way points in an intuitive way, without requiring a deep understanding of the robot's functional principle. Thus, the interface serves as an abstraction layer between the robot and the process.

After defining the task, it must be reliably performed by the collaborating human and robot. For this, the human must always be able to quickly understand what the robot is doing and follow up the reasons for a specific behavior (estimate its intention). This should be possible independently of the task and the environment (industrial, domestic, etc.). In the regarded class of robots, wear-related changes in the drive train can influence the motion execution, disturbance detection, and even the ability to fulfill the intended task expectedly. This leads to the need for a communication modality that makes the current execution and health state transparent for the human.

With regard to these aspects, a teach-in by hand guided demonstration approach for tendon driven joint elastic robots with uncertain joint torque estimations is presented. Further, the influence of the execution feedback using different visualization elements on the user's situation awareness, as well as wear monitoring capabilities are investigated, necessary to evaluate the robot's intention and check if the performance expectations on the robot are met.

7.4.1 Teach-In Control Approach under Uncertain Joint Torque Estimations

The common approach for cobots to enable an intuitive way point teaching phase is to demonstrate all or a subset of target points, by moving the manipulator manually in the specific configuration. This is repeated for all motions required to perform the process. If the joints are not back-drivable, the human has to be supported to move the joints by hand during the teach-in phase. For this purpose, the joint torques exerted by the worker have to be sensed, and the joints moved accordingly. This can be realized by using the disturbance torque estimations $\hat{\boldsymbol{\tau}}_{\boldsymbol{ext}} \in \mathbb{R}^N$ of all joints. In [48] this has been done in combination with gravity compensation creating two collision reaction strategies. In the first strategy, the estimated disturbances were used as control torques moving the arm away from the collision

$$\boldsymbol{\tau_c} = \boldsymbol{g(q)} + \boldsymbol{K_R}\hat{\boldsymbol{\tau}}_{\boldsymbol{ext}}, \tag{7.15}$$

with the gravity vector $\boldsymbol{g(q)} \in \mathbb{R}^N$ and a user defined diagonal gain factor $\boldsymbol{K_R} \in \mathbb{R}^{N\times N}$. This approach has the effect that even if the disturbance torque is disappeared, the gravity compensation causes the arm to move further. Alternatively, the external torque estimation can be used to update the current desired joint position, creating a motion that resolves the collision and stops as soon as the disturbance torques vanish

$$\boldsymbol{q_d} = \boldsymbol{q_{d,c}} + \int \boldsymbol{K_R}\hat{\boldsymbol{\tau}}_{\boldsymbol{ext}}\,\mathrm{d}t, \tag{7.16}$$

with the desired joint position at the moment of collision $\boldsymbol{q_{d,c}} \in \mathbb{R}^N$ and a user defined diagonal gain factor $\boldsymbol{K_R} \in \mathbb{R}^{N\times N}$.

Using these strategies as teach-in approach has some limitations. The first strategy (7.15) requires an accurate torque control ability of the robotic system, whereas the second strategy (7.16) changes the desired joint position using an integral term assuming that the external torque will disappear during motion. If this is not the case because of continuous hand guided

motion, the desired joint position will continue to increase. Since the current joint position (or equivalently the end-effector position) is the only feedback, the user will stop moving the arm as soon as the targeted position is reached. If the position controller is not able to follow the desired value, this can lead to desired values $\boldsymbol{q_d} \in \mathbb{R}^N$ that are larger than intended by the user, depending on the exerting joint torques and gain factor $\boldsymbol{K_R}$.

As an alternative position controlled strategy, a joint side admittance control approach can be considered. Here, the external disturbances are used to compute a new desired joint position $\boldsymbol{q_d}$ based on the current joint position $\boldsymbol{q} \in \mathbb{R}^N$ and a user-defined admittance spring coefficient $k_{ad} \in \mathbb{R}$. This coefficient defines the sensitivity of the system. Since the teach-in strategy should enable moderate speed but also provide an accurate positioning ability, this value should be chosen appropriately

$$\boldsymbol{q_d} = \boldsymbol{q} + \boldsymbol{K_{ad}}\hat{\boldsymbol{\tau}}_{\boldsymbol{ext}}, \tag{7.17}$$

with $\boldsymbol{K_{ad}} \in \mathbb{R}^{N \times N}$ the diagonal matrix containing the reciprocals of the admittance spring coefficient k_{ad} of each joint. In order to get a damped motion, the desired motor velocity $\dot{\boldsymbol{\theta}}_{\boldsymbol{d}} \in \mathbb{R}^N$ and joint velocity $\dot{\boldsymbol{q}}_{\boldsymbol{d}} \in \mathbb{R}^N$ are set to zero. Since the disturbance torque estimation can be erroneous, as discussed in the previous section, a threshold $\tau_{ext,t}$ is introduced for each joint that has to be exceeded before an external torque is recognized.

$$\hat{\tau}_{ext} = \begin{cases} \hat{\tau}_{ext} - \tau_{ext,t} & \text{if } \hat{\tau}_{ext} > \tau_{ext,t} \\ \hat{\tau}_{ext} + \tau_{ext,t} & \text{if } \hat{\tau}_{ext} < \tau_{ext,t} \\ 0 & \text{otherwise} \end{cases} \tag{7.18}$$

This teach-in strategy is evaluated in simulation in combination with the position controller introduced in Chapter 6. The hand guiding is simulated by exerting a joint torque as long as the target joint position is not reached, and faded out to the threshold value $\tau_{ext,t}$ if the target position is approached. To avoid discontinuities in the exerted torque, these are faded in during a user defined duration. The simulation results are depicted in Figure 7.4, with an admittance spring coefficients $k_{ad} = 75.0\,\text{Nm/rad}$, a disturbance torque threshold of $\tau_{ext,t} = 5.0\,\text{Nm}$, a fade in duration of 2 s, and a maximum external torque of 20 Nm. The target is reached if the position error is below 0.04 °(approximately 0.04 °). The disturbance torques are estimated using the load dynamics based observer, thus $\tau_{ext} = \tau_{ext,L}$.

The experiment simulated the hand guided teach-in of a trajectory that consists of two points. The first point represents a pick position and the second point a delivery position where the picked object is handed over to a human. The motion starts at the stretched out vertical robot configuration. The current and desired joint position q and q_d show that with increasing disturbance torque $\hat{\tau}_{ext,L}$ the desired joint position is adjusted appropriately. If the target position is approached, the external torque is decreased, which leads to the desired value converging to the current joint position. The external torque is faded out as soon as the joint position reached the target position within the desired accuracy. During this fade out duration, the control error temporarily increases again, since the presented position controller needs some time for compensating the load change. The same behavior can be observed during the teach-in motion to the delivery position. Whereas the shoulder and elbow joint show a very similar torque and accuracy profile, the wrist joint position accuracy is influenced by the kinematic coupling of the

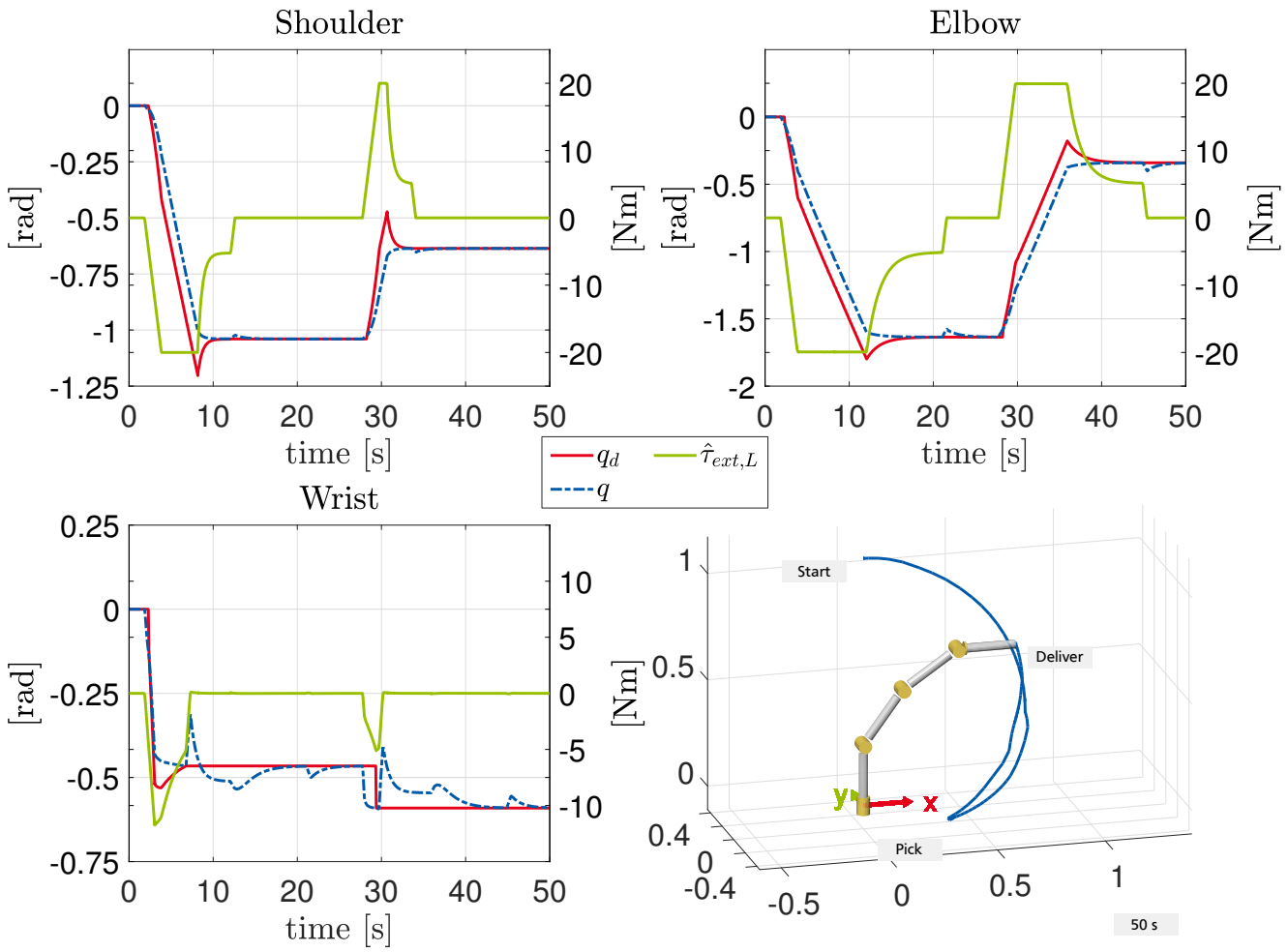

Figure 7.4.: Simulated admittance control based teach-in control evaluation of the pick and deliver motion with the resulting desired joint position q_d, the current joint position q, and the external torque estimation $\tau_{ext,L}$ in the shoulder, elbow, and wrist joint. The start, pick and deliver position in Cartesian space are shown in the bottom-right.

elbow and wrist. The additional temporary error peaks appear each time the disturbance torque in the elbow discontinuously leaves the maximum torque or enters the torque threshold region. Nevertheless, these inaccuracies are compensated by the position controller.

The hand guided teach-in capability of a robotic system built for human-robot collaboration is essential and widely used. In contrast to cobots that are equipped with joint torque sensors or force/torque sensors at the end-effector with stiff joints or only small joint elasticities, the actuation principle of tendon driven highly elastic robots introduces uncertainties in control and joint torque estimation, in particular, if only position sensing is available. In this chapter, a teach-in approach has been proposed regarding this scenario. It is based on the position controller presented in Chapter 6 that can compensate for model errors in the drive train to realize a joint space admittance reaction on estimated external torques. This approach has been evaluated in simulation, showing its applicability even in the presence of external torque estimation errors.

7.4.2 Execution Feedback for Collaborative Tasks and Performance Monitoring

Widely applied user interfaces for cobots (e.g., the *KUKA smartPAD* or the *Universal Robot PolyScope GUI*) are designed as control pads that are used for both, programming the process that has to be executed and to visualize the current execution state. With regard to this, the process is displayed as symbols aligned in the time line or tree-like structure with an additional 3D view of the current robot configuration. These visualizations provide all necessary information to monitor the current execution state, but, depending on the process complexity and process element granularity, the orientation in the process, according to the current execution updates, can be challenging for the operator. Further, the health status of the robot is not visible at a glance which is especially important regarding the drive train of an elastically tendon driven system.

In this section, the influence of the execution feedback using different visualization elements on the user's situational awareness is investigated. The visualization elements consist of the elements as mentioned above and in addition, an augmented reality based feedback, as well as health information. The augmented reality based information visualization has been developed with regard to the use of non-fixed view points, suitable for changing environments and different collaboration scenarios. Further, the wear monitoring capabilities are investigated, in order to prevent failures and check if the performance expectations on the robot are met.

Execution Feedback for Collaborative Tasks

The current trend of connecting machines to exchange information via the network also has the potential to enhance user feedback since the information flow can be forwarded to additional interfaces. Three-dimensional visualizations of the current robot configuration provide a realistic representation of the changing state, but the viewpoint is probably not suitable according to the current view of the user regarding the real scenario. This makes it challenging to transfer the visualized information to reality. Furthermore, the objects of the environment that can aid to keep the overview are not displayed. Overlaying the real scenario with additional information can be a suitable solution to create a better understanding of the current situation and supports the information flow from the robot to the human. In order to investigate the effects on human-robot collaboration, a web-based user interface has been developed containing common robot state visualization elements, as well as an augmented reality based one, creating an intuitive user experience. This web interface has been evaluated in a preliminary user study [44] in cooperation with the author.

The web-based solution provides the ability of a platform-independent visualization on different devices. Regarding human-robot collaboration, different approaches to use this visualization depending on the task are conceivable. For example, if a robot collects parts from different boxes or machines to be assembled by the human, or grasps objects to support elderly people, a statically mounted monitor with a fixed view nearby the robot or workspace can be sufficient to follow the performed motion. In the case of direct interaction, where the robot serves as a third hand and alternates its movements depending on changing conditions, a lightweight head-mounted

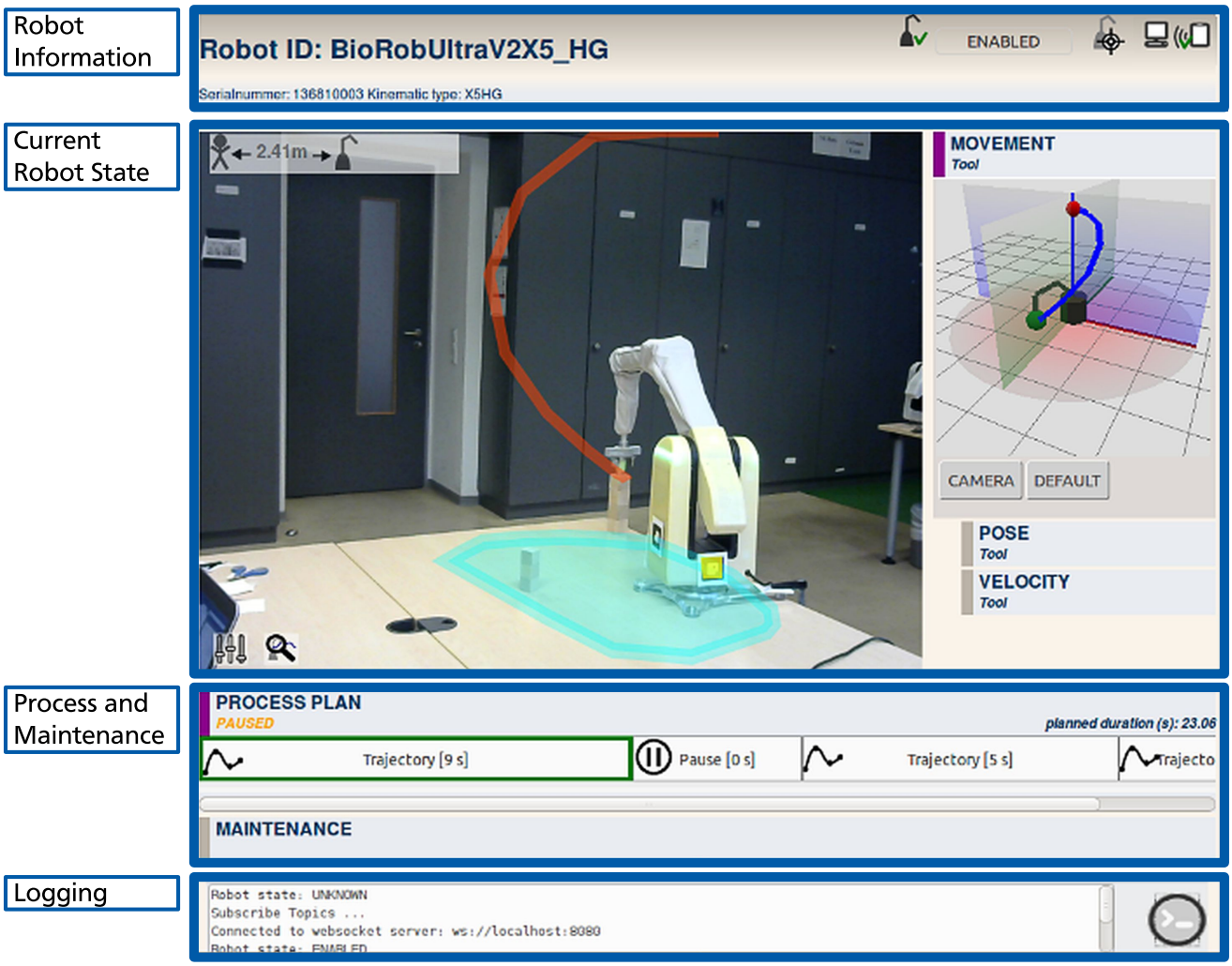

Figure 7.5.: The web-based graphical user interface to visualize the current robot state to the human, consisting of four areas to visualize the robot information, current robot state, process and maintenance, and logging information. The video stream in the robot state area can be overlayed with different information related to the current motion. This interface is used for the presented user study investigating the human's situation awareness.

display, that shows the process information if needed according to the human's perspective, would be more convenient. For inspection purposes in a production line, the visualization could be transferred to a supervisor's workstation or activated on a tablet using the integrated camera if the workstation is approached.

The developed solution uses a marker-based approach to locate the used camera relative to the robot base coordinates. Since robots designed for safe physical human-robot interaction may often change their location without having a fixed base joint, the challenge consists in realizing a localization approach where both, the markers on the robot and the camera itself are allowed to move. Based on the determined localization information and the robot state, different additional information can be displayed in combination with the real scene as depicted in Figure 7.5.

The graphical user interface consists of four areas that visualize the robot information (robot name, connection status), the current robot state (camera scene, 3D visualization, exact end-effector pose, accuracy and velocity), the process and maintenance information, as well as a logging area for debug purpose (for power users). The live stream is a central element to visualize the current robot state and can be overlayed with information about the end-effector trajectory, positions of the single joints, a safety region that represents a 2D projection of the needed space to execute the current trajectory on the table, as well as the start and goal position. The camera perspective can be freely changed during execution by moving the camera.

The questions about how the displayed information influences the user's situation awareness, the perception of the robot state, and the perception of safety has been evaluated by a user study. In the investigated task, the user had to rebuild a pattern consisting of different colored wooden pieces with the robot passing the needed objects from different locations. In the first phase of the evaluation, the user had no additional information but only the test setup with the robot moving, in the second phase the developed application supported the user. After each phase, the questionnaire was completed.

Concluding the results of the case study, the following statements can be made:

- The proposed information visualizations positively influenced the situation awareness.
- The understanding of the robot behavior (including the intention of the next movement, potential danger, and retracing the performed motion) could be improved.
- The perception of safety and trust while working with the robot hat not been negatively influenced.

During the experiments, it could be observed that the overlayed live stream has been the most perceived element. Further, displaying the health status of the robot using a percentage value led to overestimation and seems to be not suitable to decide whether the robot is able to perform well. Instead, a more meaningful metric could be used, like execution duration changes or control error of the end-effector, that is less abstract.

The case study was performed with 19 persons (six inexperienced robot users), thus, the results are not statistically valid. However, the evaluation can be used as a preliminary study for further investigations about how the information flow from the robot to the user can improve the collaboration.

Performance Monitoring

In real applications, the continuity of correct service (reliability) is a key factor for new technologies to be useful. To realize this, machines typically have a defined guaranteed live time that can be extended by appropriate maintenance. For the regarded system of elastically tendon driven robots, this life time is mainly influenced by the inherent elongation characteristics of the tendons that can vary because of changing loads or contacts and collisions. Thus, monitoring of changes in the drive train must be done continuously.

Assessing the maintenance needs of a robot to ensure the performance quality requires some measurable metrics to be available. As presented in Chapter 5 changes regarding the tendon elongation can be estimated using the link dynamics model resulting in a motor position offset $\hat{\Delta}_e$. This is limited to the case of free motions since external disturbances that cause additional elongation cannot be considered if no direct joint torque measurement is available. More parameters for system change monitoring can be computed using the reflected motor and joint position, as well as the joint space control accuracy. For a tendon driven joint elastic system one obtains the following aging metrics a_i, with $i = 1, 2, 3$, for each joint.

$$a_1 = \hat{\Delta}_e \tag{7.19}$$
$$a_2 = |\theta - q| \tag{7.20}$$
$$a_3 = |q_d - q| \tag{7.21}$$

with the estimated tendon elongation motor position offset $\hat{\Delta}_e$, the desired joint position q_d, as well as the current motor and joint position θ and q respectively. Looking at these metrics, their values can be influenced by multiple wear and aging sources resulting in similar behavior. Besides software errors and failures of the electronics and communication, the actuation principle related errors are determined by tendon elongation, position sensor errors and drive train friction changes. For identification of these wear effects, the following approach can be used in the case of free motions with no load.

The metric a_1 can be used to detect the tendon elongation. But a_1 will also increase if the motor or joint position sensor drifts. Sensor drift is regarded as a position error that increases over motion. In order to distinguish between tendon elongation and sensor drift, the value of metric a_2 can, for example, be compared after execution of one analysis motion with the value after repeating the same motion for a reasonable number of times. If a_2 stays unchanged, the increased values of a_1 is caused by tendon elongation, and by sensor drift otherwise. This kind of evaluation is possible because of the asymptotic weight dependent tendon elongation characteristic (see Chapter 5). While repeating the same analysis motion and comparing a_2 in the identical robot configuration, the tendon elongation would stay nearly static and, thus, the value of a_2 would as well. If both, the tendon elongation and the sensor drift, are increasing with the same time characteristics, it is not possible to distinguish between these error sources using the available sensors and additional analysis effort has to be performed.
Damaged position values typically result in a position value peak (if not handled by a sensor built-in error check), that will also cause a value peak in the metrics a_2 or a_3. If such sudden change peak appears, that should be larger than reasonable value peaks during typical motions (e.g., caused by collisions), an analysis motion through the whole sensor range can be executed, and both metrics checked again for change peaks. If a value peak can repeatedly be detected at the same position, a sensor damage is detected, or alternative error sources have to be checked (e.g., bus communication). Since the described error sources would cause an increased control error (a_3) during the motion (in the case of a used position control approach), only in their absence metric a_3 can be used to detect an increased friction in the drive train.
An abstract approach for the described wear identification is depicted as states and transitions in Figure 7.6. This represents a basic monitoring approach that must be adapted to each specific system (e.g., adjust thresholds or incorporate other available sensors) in order to reach a low false positive wear detection. Further, apart from the detection of not tolerable raise of a_1 and

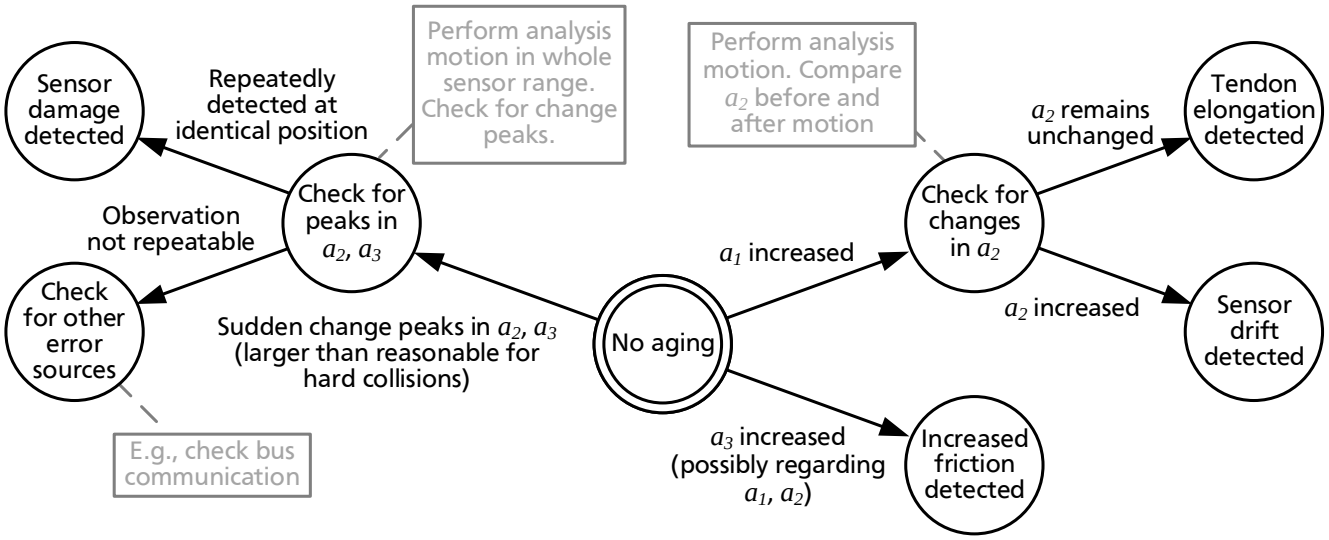

Figure 7.6.: Depiction of a wear identification approach using the presented aging metrics a_1, a_2, and a_3 as state representation.

a_3 or change peaks in a_2 and a_3, this scheme is not meant to be carried out automatically, but in a corrective maintenance step.

Besides the wear source identification as presented above, the metrics can also be used to detect aging of the system to indicate if a detailed wear identification should be conducted. In real-world applications, the presented metrics are influenced by the performed motion and loads. To overcome this weakness, one can use some statistical evaluations of the recorded values, e.g., median, mean, maximum, or minimum, during a specific evaluation motion (carried out in regular intervals) or a continuous long-term observation. In order to acquire the necessary data for a long-term evaluation, one could record the metrics presented above (and other available values as, e.g., control torques) at low frequency to keep the amount of data in a reasonable range. In parallel, a buffer window containing all data in high sample rates could be kept available and flushed for recording, if a special event occurs (e.g., collision, communication errors) for later detailed investigations.

7.5 Conclusion

In this chapter, the human-robot collaboration capabilities for ultra lightweight tendon driven series elastic robots have been analyzed, regarding the challenges that result from wear in the particular actuation design. The basic capabilities must allow to interact with the robot transparently, that consists of physical interactions as well as providing information about the internal robot state to understand the robot's behavior.

An error analysis has been proposed to investigate the influence of drive train model errors on the possible observer-based disturbance torque estimations with only position sensors available. Therefore, a pick motion in simulation and a collision experiment with a real robot has been performed. The link dynamics based observer showed significant sensitivity to changes in the drive train because of the used motor position and joint position related joint torque estimation.

Additionally using the motor dynamics resolved this sensitivity but introduces the requirement of an accurate realization of the commanded values of the power electronics or current sensing, and an exact friction model. If this friction model is load dependent, as is the case for the investigated system with high gear ratios, the wear dependent joint torque estimation is needed to compute the current friction forces, which again introduces wear dependency in the estimation. To reliably use these approaches, suitable contact and collision thresholds have to be defined and the drive train changes observed to adjust these limits automatically or to request maintenance.

In the case of human-robot collaboration, the basic mutual communication should be intuitive but in particular, enable the human to understand the robot's behavior. Based on the disturbance joint torque estimation, a manual teach-in approach has been presented that is able to perform even if drive train model inaccuracies are present. Further, a preliminary user study has been conducted, showing that an information visualization of the current robot state, executed process, and future motions positively influences the user's situation awareness. In particular, the understanding of the next movement, potential danger, and retracing the performed motion could be improved, where the augmented reality based live stream has been perceived the most beneficial in comparison to the other common visualizations.

In order to rely on the robot despite increasing operating hours, the health state of the robot has to be monitored. For this purpose, a monitoring approach has been presented and discussed to detect wear in the regarded actuation approach.

The proposed investigations and approaches showed that an ultra lightweight tendon driven series elastic system is capable of human-robot collaboration. While drive train wear strongly influences the accuracy of the detection of external disturbances, these changes can be estimated to schedule maintenance. Further, the basic internal execution state should be communicated to the human, e.g., via an augmented reality approach, to increase the understanding of the robot's behavior.

8 Conclusion

Because of their safety capabilities, ultra lightweight tendon driven series elastic robots are very suitable for safe physical human-robot interaction and collaboration. But for using a robot in the vicinity of humans, it must provide a dependable system behavior. The challenges of a tendon driven joint elastic robot affecting the robot's performance are mainly constituted by the combination of possible changes in the drive train caused by wear, unavoidable system model inaccuracies, and the high elasticities enabling oscillations in the joints. With the motivation to investigate the dependability capabilities, this thesis makes several contributions to the fields of velocity estimation, characteristics of synthetic fiber ropes for robust force transmission, trajectory control, and human-robot collaboration. In particular, the contributions in the field of velocity estimation, synthetic fiber rope characteristics, and robot state visualization are not limited to the regarded ultra lightweight tendon driven series elastic robot actuation. The individual contributions are summarized in Section 8.1 and the outlook according to the implications is given in Section 8.2.

8.1 Contributions

Safety Evaluation According to the New ISO/TS 15066

One key for productive HRC is to enable a collaboration that lets the robot perform effectively without the need for specific motion restrictions to ensure the human's safety. In the industrial environment, the ISO/TS 15066 has been introduced to complement the existing standards regarding safety requirements for collaborative robots. The risk assessment according to the ISO/TS 15066 to realize the power and force limiting safety method gives an insight into the inherent safety capabilities for collaborative robots.

Here, the relevant collision case of free and transient contacts is mentioned, which has been analyzed for the tendon driven joint elastic *BioRob* arm and the small sized, stiff UR3 robot. The evaluation showed that the effective mass reduction capability of tendon driven robots permits end-effector velocities satisfying the human's biomechanical limits, especially during handling of low loads, which are remarkably higher than for robots with downscaled and rigid kinematic structures. Albeit the energy transfer and biomechanical limits of the ISO TS/15066 are used, the effective mass has been computed in a more sophisticated way to regard the center of mass relocation at the tendon driven robot.

Additionally, the effect of high joint compliance has been investigated during a collision experiment, showing that the robot immediately bends like an elastic rod after surface contact. Besides this effect, that is also relevant at clamping situations since the human can twist the robot to free, e.g., its hand, the recorded collision forces showed that the biomechanical limits are satisfied. Altogether this shows the substantial safety potential of tendon driven robots with high joint compliance. Nevertheless, one should not neglect the stored potential energy in the

elastic elements, as well as an appropriate joint oscillation damping and collision detection, that are only partially regarded in the ISO/TS 15066.

Enhanced Velocity Estimation for Highly Joint Elastic Robots

An accurate velocity estimation is relevant in many tasks related for example to control or model-based computations. Especially for lightweight and downscaled kinematic structures, the applicable sensor size and, thus, the resolution is limited which introduces significant discretization errors. Furthermore, elasticities enable fast motions but can also lead to oscillations resulting in position signals containing a broad bandwidth of frequencies and velocities. Kalman filter approaches already showed accurate performance in position signal based velocity estimation, but within a small bandwidth that correlates with the filter's measurement variance parameter.

To obtain the knowledge about how to appropriately adjust the measurement variance parameter, it has been analyzed based on position signals in a broad velocity range and frequency bandwidth. During this analysis, the optimal measurement variance parameter has been computed minimizing the velocity estimation error. The characteristics of these optimal values revealed three observations that served as a basis for the proposed new measurement variance update rule.

The resulting novel adaptive Kalman filter approach adapts better than the compared state-of-the-art approach to the investigated application with ultra lightweight tendon driven elastic robots, producing a smoother and more accurate velocity estimation over a larger bandwidth. This has been shown in simulation and robot experiments by performing a frequency analysis, oscillation motions containing different frequencies and velocities, as well as a collaboration motion where an object is released which suddenly changes the robot's dynamics causing fast velocity changes and oscillations. Among the realized quantitative signal comparisons, a performance overview can be obtained from the frequency analysis. This showed that the proposed filter extends the bandwidth from about 10 Hz of the state-of-the-art approach to about 100 Hz.

Systematic Elongation Analysis for Tendon Material Selection

In biologically inspired mechanical structures, tendons are used to transmit forces along a kinematic chain, which must satisfy high robustness requirements by simultaneously allowing small pulley radii. Due to size and force requirements, cables or belts are often not applicable, in contrast to thin synthetic fiber ropes, because of the rope's high breaking force to weight ratio. Typically, only a little information about the rope is provided by the manufacturer, thus, it is not evident if the particular rope is suitable to be used as reliable force transmission component which mainly depends on its wear related elongation behavior. The available qualitative fiber elongation characteristics show that the different fibers have the drawback of irretrievable elongation to different extents, but it is unclear how this effect impacts the elongation of the produced rope.

In order to create new insights into the elongation characteristics of synthetic fiber ropes and supporting the rope selection, new comparative creep experiments regarding different fiber materials, manufacturers, and diameters have been performed and presented in this work. The experiments showed that the elongation characteristic does not only depend on the fiber, but also on the manufacturing process. Interesting for the practical use is, for example, the observations that a larger diameter does not necessarily result in a lower elongation regarding the

same force or that the not commonly available ropes consisting of Technora Black and Vectran showed the less elongation slope, which is relevant regarding long-term use. Using ropes in tendon driven robots typically needs to introduce pulleys for guiding purposes. Hence, the influence of varying number of pulleys that stress a rope consisting of commonly used fiber has been experimentally evaluated under different loads. Here, it was observed that stressing a rope more than once or a low bending angle result in a larger elongation.
The observations during the presented experimental evaluation support the rope selection in the design process of any tendon driven system and provide indications about long-term behavior. Since the tendon elongation influences the drive train characteristics and has to be monitored to avoid system failures, an observer approach has been proposed that enables elongation detection in tendon driven kinematic chains, only equipped with motor position and joint position sensors, even under model inaccuracies. The approach that omits the need for joint torque measurements has been successfully evaluated in simulation and robot experiments.

Robust Tracking Control under Uncertainties

The identified drive train model parameters for tendon driven joint elastic robots can be erroneous because of inaccurate parameters, unmodeled effects or variations over time, for example, because of wear or load dependent friction. Nevertheless, it is expected from a robotic system, that it accurately performs a motion without alterations over time. State-of-the-art control approaches for joint elastic robot arms rely on an accurate joint torque measurement, drive train model, and dynamics model. Available torque sensors with a suitable torque range are heavy and large and do not fit into the lightweight actuation. Thus, so far only erroneous model-based joint torque estimation and consequently inaccurate load dependent friction models can be used, for which these control approaches perform unsatisfactorily.
With the aim to reduce the model dependency, the performance of a friction observer under joint torque estimation errors has been analyzed. This led to the final proposed controller design that is able to compensate for both, drive train and load dynamics model inaccuracies. In particular, it integrates a friction observer without the need for explicit joint torque measurements, in a way that it acts as an integrational term eliminating the steady-state control error. As a result, control errors caused by external disturbances as contacts will lead to high control torques produced by the compensation. To mitigate this effect, a contact mode, based on external torque observation that limits the exerted forces is introduced.
The control performance has been evaluated in simulation and robot experiments in comparison to a common alternative state space control design, that is also able to compensate for the drive train inaccuracies but using a joint side PID controller. The results show that the proposed control approach performs more accurate, faster compensates changes in the dynamics caused by gripped objects and shows a well-damped motion. In the performed pick and inch-foot-inch motion on the real robot, this resulted in a reduction of the execution time of approximated 60 % and 55 % respectively.

Human-Robot Collaboration Capability Analysis under Uncertainties

An essential part of human-robot collaboration consists of the physical interaction and joint task solving. To sense physical interactions, the robotic arm must be able to estimate external forces that can be done by disturbance observers based only on internal data suitable for the regarded system. These estimations are influenced by possible drive train uncertainties caused by model inaccuracies or wear effects.

The accuracy limitations are investigated and discussed theoretically and via simulation experiments, to reveal the capabilities of tendon driven joint elastic robots regarding external torque estimations. They clarify which part of the drive train is relevant for high accuracy and should carefully be treated during the robot design process. Furthermore, the user should be able to teach the needed robot motion for the executed process without high effort. For this purpose, a teach-in controller that enables hand guided motions even under drive train errors is presented for the considered system and evaluated in simulation experiments.
Besides the physical interaction, successful collaboration requires clear communication between the human and robot, so that the robot behavior is transparent for the human at any time. One influence on this is the information provided to the user concerning the robot's execution state or its intention. Regarding this, a first preliminary user study has been performed that investigated the influence of state visualizations on the user's situation awareness in collaborative task solving. Besides the commonly used visualization elements, an augmented reality based feedback, as well as health information have been used in the created clear user interface. The evaluation showed that the execution state visualizations positively influenced the user's situational awareness and understanding of the robot's behavior during the collaboration. In particular, the augmented reality based video stream has been perceived the most. Further, the user should be able to assess the robot's health state, increasing the trust in collaboration. For this purpose, the possible wear estimation metrics have been introduced and discussed.

8.2 Summary and Outlook

In this work, the dependability capabilities of ultra lightweight tendon driven series elastic robots have been investigated. It was shown, that the inherent challenges of the considered actuation approach mainly influence the reliability of the system because of its time-varying characteristics, unavoidable system model inaccuracies, and the high mechanical elasticities. The contributions made introduced new approaches to compensate the drive train uncertainties regarding velocity estimation, that constitutes an important basis for further computations, or trajectory tracking control. The presented synthetic fiber rope experiments gained new insights into the rope characteristics, which supports the material selection and rope routing decision during a robot design process, in order to reduce the effect of wear in the tendon related drive train, creating a robust torque transmission. The performed preliminary user study investigated the information provision of the robot's execution state to increase the human's understanding of the robot's intention. It showed that the execution state visualization positively influences the situational awareness during the collaboration. Further, the augmented reality based visualization approach has been perceived more intensively than the single 3D or process visualization.

Whereas the motivation is derived from the regarded ultra lightweight tendon driven joint elastic system, the results concerning Kalman filter based velocity filtering, synthetic fiber rope characteristics, and situation awareness in human-robot collaboration are rather general and can also be used in other research fields concerning these issues. Regarding collaboration, it was shown that in particular the disturbance estimation, based on uncertain joint torque estimations, reduces the accuracy of perceiving contacts. Nevertheless, this can be compensated to a certain extent by thresholding the estimated joint torques and continuously monitoring the drive

train changes as tendon elongation or performance loss, to schedule corrective maintenance if necessary.

The contributions made in this thesis have some implications for future research.
The theoretical safety analysis of collaborative robots according to the biomechanical limits in ISO/TS 15066 showed the great potential of tendon driven systems, whereas joint elasticities with low stiffness further lower injury risk. In order to reduce the above-mentioned accuracy influence of uncertain joint torque estimations on contact perception, new highly integrated ultra lightweight joints should be considered in future research. Those joints should provide an accurate torque estimation and position measurements. Additionally, the uncertainties introduced by tendons can be avoided in those joints of the kinematic chain, where shifting the motor does not significantly reduces the robot's effective mass.
The synthetic fiber rope investigations revealed that the rope's elongation characteristics are influenced by the manufacturer's production process and the used braiding. Besides the fiber's elongation characteristics, it is interesting to analyze which production process would lead to a preferably low elongation, with the purpose to use ropes as dependable actuation component.
Finally, the information flow of the current robot state is essential for human-robot collaboration in both directions. Since the human is good at observing, interpreting and understanding, a new communication mean that simplifies these steps is needed. As presented, an augmented reality based approach can be a suitable solution, but this is not applicable or would not be accepted by the user in any situation because of the needed glasses. Thus, in collaboration scenarios where multiple modalities and interfaces cannot be used, more basic communication tools are required. For example, a LED ring could be mounted at the end-effector, with the LED lit in the direction of the current or subsequent motion.
The usage of the unique safety features of the regarded actuation approach is also interesting for other fields of research where musculoskeletal approaches can be beneficial, as for example for orthoses or exoskeletons. Here, the presented contributions, in particular, the proposed control approach, the velocity estimation approach, the disturbance torque investigations, and tendon characteristics, can be integrated to promote their evolution.

A Appendix

A.1 Effective Mass Computation

As presented in [73], the effective mass represents the perceived mass at the operational point along a certain direction. The effective mass of a manipulator can be computed using the robot's inertia matrix $\boldsymbol{M}(\boldsymbol{q})$ and the Jacobian matrix $\boldsymbol{J}(\boldsymbol{q})$ as

$$\boldsymbol{\Lambda}(\boldsymbol{q}) = \left(\boldsymbol{J}(\boldsymbol{q})\boldsymbol{M}^{-1}(\boldsymbol{q})\boldsymbol{J}^{T}(\boldsymbol{q})\right)^{-1},$$

with the "pseudo kinetic energy matrix" $\boldsymbol{\Lambda}(\boldsymbol{q})$ representing the end-effector inertial properties. Regarding the case of positioning the end-effector in the workspace, the Jacobian matrix related to the linear velocity $\boldsymbol{J}_{v}(\boldsymbol{q})$ determines the pseudo kinetic energy matrix

$$\boldsymbol{\Lambda}_{v}^{-1}(\boldsymbol{q}) = \boldsymbol{J}_{v}(\boldsymbol{q})\boldsymbol{M}^{-1}(\boldsymbol{q})\boldsymbol{J}_{v}^{T}(\boldsymbol{q}), \tag{A.1}$$

which describes the end-effector translational response to a force. If the force direction is described by the unit vector $\boldsymbol{u}$, the effective mass $m_{\boldsymbol{u}}$ along $\boldsymbol{u}$ is given with (A.1) by

$$m_{\boldsymbol{u}} = \left(\boldsymbol{u}^{T}\boldsymbol{\Lambda}_{v}^{-1}(\boldsymbol{q})\boldsymbol{u}\right)^{-1}, \tag{A.2}$$

for the current manipulator joint configuration $\boldsymbol{q}$. In order to characterize the bounds of the effective mass for all force directions at a specific joint configuration, the eigenvalues σ and associated eigenvectors $\boldsymbol{\nu}$ of $\boldsymbol{\Lambda}_{v}^{-1}(\boldsymbol{q})$ can be used. For example, by setting the direction vector $\boldsymbol{u}$ in (A.2) to the eigenvector $\boldsymbol{\nu}_{\max}$ that corresponds to the largest eigenvalue $\sigma_{\max}$, one receives the maximum effective mass $m_{\boldsymbol{\nu}_{\max}}$ for a given joint configuration $\boldsymbol{q}$, and the minimum effective mass $m_{\boldsymbol{\nu}_{\min}}$ by using the eigenvector $\boldsymbol{\nu}_{\min}$ corresponding to the smallest eigenvalue $\sigma_{\min}$ instead. If the manipulator approaches a singular joint configuration, $m_{\boldsymbol{\nu}_{\min}}$ will continuously decrease and $m_{\boldsymbol{\nu}_{\max}}$ simultaneously increase.

Since the effective mass depends on the current joint configuration, comparing different robots can be realized by computing $m_{\boldsymbol{\nu}_{\max}}$ for a particular joint configuration as for example done in [126] and [88]. But, if the kinematic structure of the compared robots is not identical, the comparison of the resulting effective mass of each robot is biased by the distance of the particular joint configuration to a singularity. As alternative, one can regard a set of more than just one joint configuration.

Within this set, the joint configurations near to singularities must be removed, since for these, even for robots with low inertia, the effective mass will grow unbounded with serious consequences for the human's safety [54] in the end-effector force direction corresponding to $m_{\boldsymbol{\nu}_{\max}}$.

In order to classify whether a joint configuration is in or near to a singularity, the ratio of minimum to maximum effective mass $\beta = \frac{m_{\boldsymbol{\nu}_{\min}}}{m_{\boldsymbol{\nu}_{\max}}}$ can be regarded. A small value of β indicates

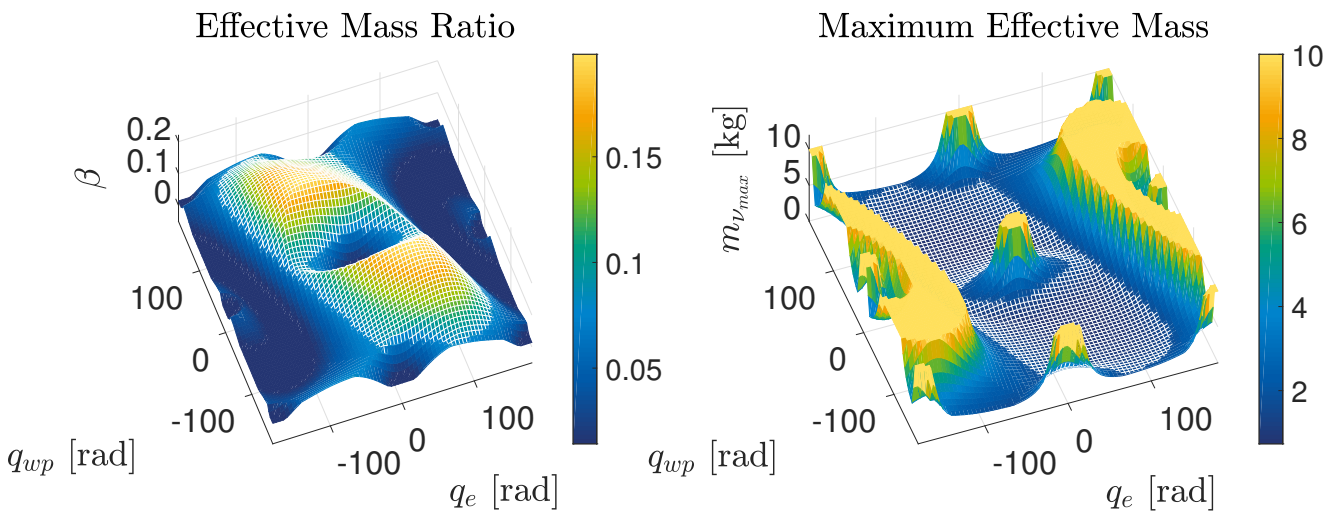

Figure A.1.: Effective mass ratio (left) and maximum effective mass (right) for sampled elbow joint q_e and wrist pritch joint q_{wp} of the *BioRob X5* arm, with fixed joint configuration for shoulder and wrist roll joint. The areas marked with white edges visualize the joint configurations and corresponding maximum effective mass values that fulfill (A.3) with $p = \frac{1}{3}$, which are distant to singularities.

that the corresponding arm configuration is closer to a singular configuration, in comparison to those with large values of β. Based on this classification one is able to compute the mean maximum effective mass using the portion of joint configurations whose effective masses are larger than a specific threshold. By determining this threshold as portion of the whole range one gets

$$\beta \geq \beta_{\min} + p \cdot (\beta_{\max} - \beta_{\min}), \tag{A.3}$$

with $p \in [0, 1]$. As visualization of this classification scheme, Figure A.1 shows the effective mass ratio β on the left and maximum effective mass $m_{\nu_{\max}}$ on the right in the case of the *BioRob X5* arm. Here, the shoulder is in a horizontal position ($q_s = -90\,^\circ$), and the elbow joint q_e as well as the wrist joint q_{wp} (changing the end-effector pitch) are sampled in a range of -180 ° to 180 ° with 5 ° steps. Since, for the last wrist joint the center of mass is assumed to be on the rotational axis with symmetric and equal mass distribution, its rotation only changes the end-effector roll angle and not the effective mass and, thus, is also set to a fixed value ($q_{wr} = 0\,^\circ$). The effective mass ratios that satisfy the inequality (A.3), with $p = \frac{1}{3}$, and the corresponding maximum effective mass values are marked with white edges.

By computing the mean maximum effective mass $\bar{m}$ and the corresponding standard deviation $\tilde{s}$ based on sampling all joints for the *UR3* [1] and *BioRob X5* [2] arm (except for the base and last joint of both robots, that do not effect the effective mass because of the kinematic structure or

[1] Shoulder: from $q_{s,\min} = -90\,^\circ$ to $q_{s,\max} = 90\,^\circ$ in 10 ° steps, elbow: from $q_{e,\min} = -180\,^\circ$ to $q_{e,\max} = 180\,^\circ$ in 5 ° steps, wrist pitch: from $q_{wp,\min} = -180\,^\circ$ to $q_{wp,\max} = 180\,^\circ$ in 5 ° steps, and wrist yaw: from $q_{wy,\min} = -180\,^\circ$ to $q_{wy,\max} = 180\,^\circ$ in 45 ° steps

[2] Shoulder: from $q_{s,\min} = -180\,^\circ$ to $q_{s,\max} = 0\,^\circ$ in 10 ° steps, elbow: from $q_{e,\min} = -180\,^\circ$ to $q_{e,\max} = 180\,^\circ$ in 5 ° steps, and wrist pitch: from $q_{wp,\min} = -180\,^\circ$ to $q_{wp,\max} = 180\,^\circ$ in 5 ° steps

center of mass assumption as above) with all values that satisfy inequation (A.3) with $p = \frac{1}{3}$, one gets

$$\bar{m}_{\text{BioRob}} = 1.13\,\text{kg}, \quad \tilde{s}_{\text{BioRob}} = 0.30\,\text{kg}$$
$$\bar{m}_{\text{UR3}} = 3.38\,\text{kg}, \quad \tilde{s}_{\text{UR3}} = 0.47\,\text{kg}$$

for the mean maximum effective masses.

This procedure enables to compute a single effective mass value for a robot regarding the whole range of joint configurations. The comparison made above showed, that the tendon driven joint elastic *BioRob* arm has an effective mass of about one third of the effective mass of the stiff UR3 robot with downscaled kinematic structure.

A.2 Velocity Estimation

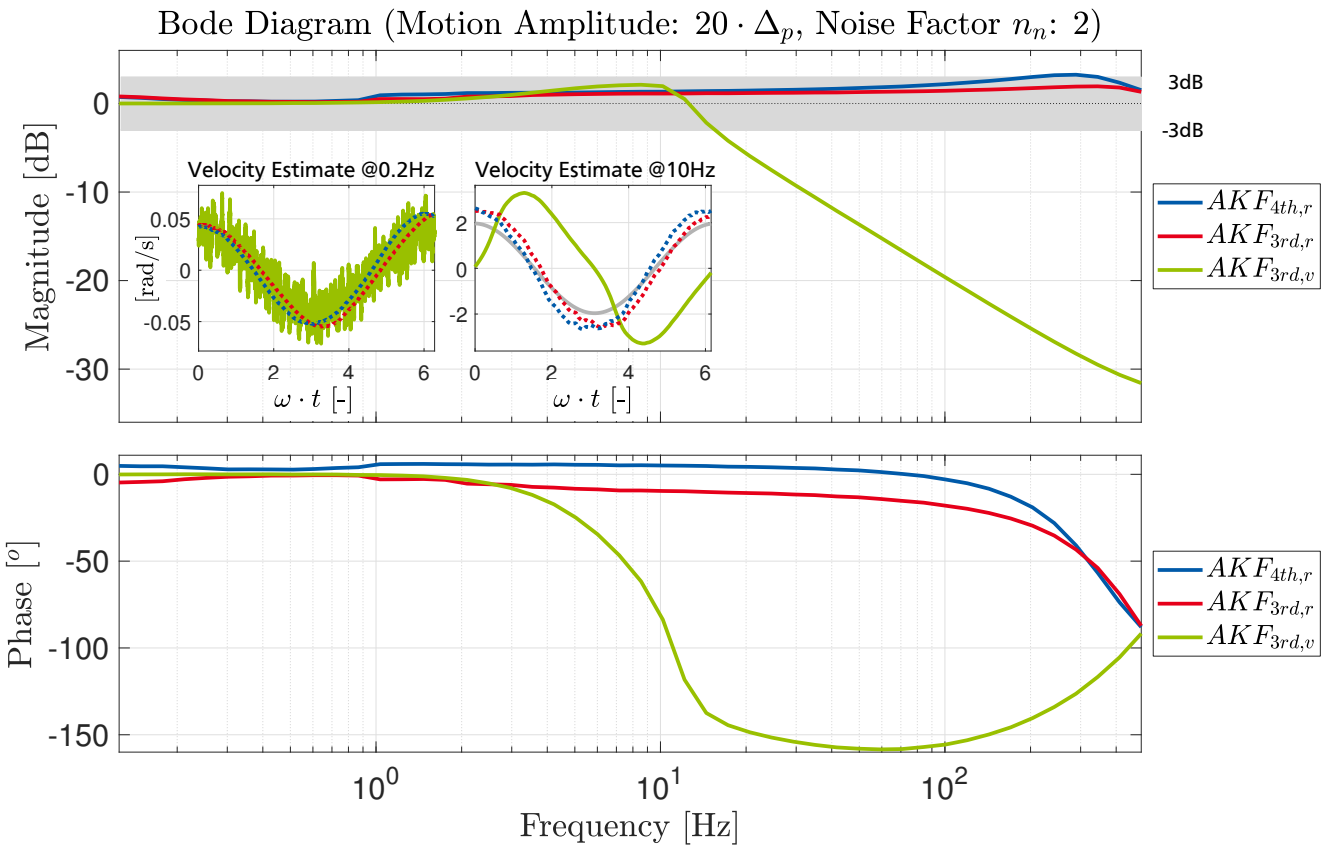

Figure A.2.: Bode diagram for the adaptive Kalman filters. Analyzed amplitude amplification and phase shift of velocity estimation resulting from a sinusoidal motion with an amplitude of $20 \cdot \Delta_p$ sensor resolution steps and a noise factor of $n_n = 2.0$. Gray area represents the 3 dB region. Detail plots show the time domain velocity estimation according to 0.2 Hz and 10 Hz motion with true velocity in gray.

A.3 Disturbance Observer

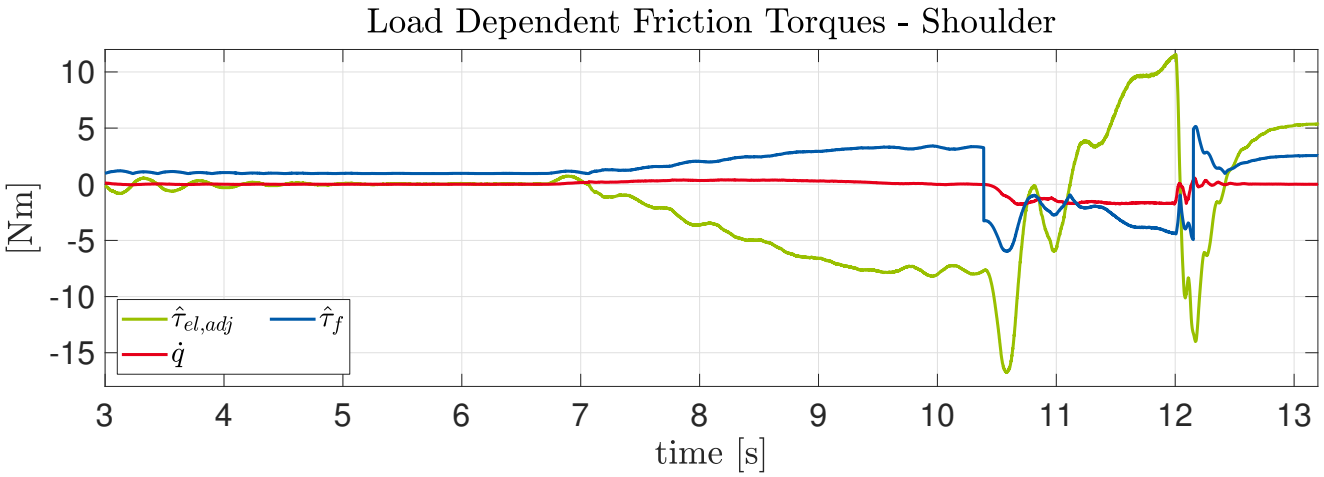

Figure A.3.: Estimated load and velocity dependent friction forces of *BioRob X5* shoulder joint during collision experiment. The friction coefficients are set to F_c = 0.95 and F_L = 0.30.

Bibliography

[1] ABB Asea Brown Boveri Limited. YuMi - Creating an automated future together. ROB0317EN_YuMi.pdf. YuMi website. [Online]. Available: http://new.abb.com/products/robotics/industrial-robots/yumi [Accessed: April 10, 2017]

[2] ABI Research. (2015, June 9) Collaborative robotics market exceeds US$ 1 billion by 2020. [Online]. Available: https://www.abiresearch.com/press/collaborative-robotics-market-exceeds-us1-billion-/ [Accessed: April 27, 2016]

[3] R. Alami, A. Albu-Schäffer, A. Bicchi, R. Bischoff, R. Chatila, A. De Luca, A. De Santis, G. Giralt, J. Guiochet, G. Hirzinger, F. Ingrand, V. Lippiello, R. Mattone, D. Powell, S. Sen, B. Siciliano, G. Tonietti, and L. Villani, "Safe and dependable physical human-robot interaction in anthropic domains: State of the art and challenges," Beijing, China, October 9-15, 2006, pp. 1–16.

[4] A. Albu-Schäffer and G. Hirzinger, "A globally stable state feedback controller for flexible joint robots," *Advanced Robotics*, vol. 15, no. 8, pp. 799–814, April 2001.

[5] A. Albu-Schäffer, C. Ott, U. Frese, and G. Hirzinger, "Cartesian impedance control of redundant robots: Recent results with the DLR-light-weight-arms," in *Proceedings of the IEEE International Conference on Robotics and Automation*, vol. 3, Taipei, Taiwan, September 14-19, 2003, pp. 3704–3709.

[6] A. Albu-Schäffer, C. Ott, and G. Hirzinger, "A passivity based cartesian impedance controller for flexible joint robots - part II: Full state feedback, impedance design and experiments," in *Proceedings of the IEEE International Conference on Robotics and Automation*, vol. 3, New Orleans, LA, USA, April 24 - May 1, 2004, pp. 2666–2672.

[7] ——, "A unified passivity-based control framework for position, torque and impedance control of flexible joint robots," *The International Journal of Robotics Research*, vol. 26, no. 1, pp. 23–39, January 2007.

[8] Automata Technologies Limited. Introducing Eva. Eva website. [Online]. Available: https://automata.tech/product.html [Accessed: April 10, 2017]

[9] A. Avižienis, J. C. Laprie, B. Randell, and C. Landwehr, "Basic concepts and taxonomy of dependable and secure computing," *IEEE Transactions on Dependable and Secure Computing*, vol. 1, no. 1, pp. 11–33, January-March 2004.

[10] Barrett Technology. WAM Arm. DS_WAM.pdf. WAM Arm website. [Online]. Available: http://www.barrett.com/products-arm.htm [Accessed: August 10, 2017]

[11] A. Bauer, D. Wollherr, and M. Buss, "Human-robot collaboration: A survey," *International Journal of Humanoid Robotics*, vol. 05, no. 01, pp. 47–66, 2008.

[12] P. R. Belanger, P. Dobrovolny, A. Helmy, and X. Zhang, "Estimation of angular velocity and acceleration from shaft-encoder measurements," *The International Journal of Robotics Research*, vol. 17, no. 11, pp. 1225–1233, November 1998.

[13] A. Bicchi and G. Tonietti, "Fast and "soft-arm" tactics [robot arm design]," *IEEE Robotics Automation Magazine*, vol. 11, no. 2, pp. 22–33, June 2004.

[14] R. Bischoff, J. Kurth, G. Schreiber, R. Koeppe, A. Albu-Schäffer, A. Beyer, O. Eiberger, S. Haddadin, A. Stemmer, G. Grunwald, and G. Hirzinger, "The KUKA-DLR lightweight robot arm - a new reference platform for robotics research and manufacturing," in *Proceedings of the 41st International Symposium on Robotics (ISR 2010) / 6th German Conference on Robotics (ROBOTIK 2010)*, Munich, Germany, June 7-9, 2010, pp. 1–8.

[15] R. H. Brown, S. C. Schneider, and M. G. Mulligan, "Analysis of algorithms for velocity estimation from discrete position versus time data," *IEEE Transactions on Industrial Electronics*, vol. 39, no. 1, pp. 11–19, February 1992.

[16] G. Bätz, B. Weber, M. Scheint, D. Wollherr, and M. Buss, "Dynamic contact force/torque observer: Sensor fusion for improved interaction control," *The International Journal of Robotics Research*, vol. 32, no. 4, pp. 446–457, April 2013.

[17] A. Calanca, R. Muradore, and P. Fiorini, "A review of algorithms for compliant control of stiff and fixed-compliance robots," *IEEE/ASME Transactions on Mechatronics*, vol. 21, no. 2, pp. 613–624, April 2016.

[18] Carbon Robotics. Kick Ass Trainable Intelligent Arm. Carbon Robotics website. [Online]. Available: http://www.carbon.ai/ [Accessed: April 10, 2017]

[19] W. Chen and M. Tomizuka, "Direct joint space state estimation in robots with multiple elastic joints," *IEEE/ASME Transactions on Mechatronics*, vol. 19, no. 2, pp. 697–706, April 2014.

[20] J. Colgate and M. Peshkin, "Cobots," U.S. Patent 5,952,796, Sep. 14, 1999.

[21] D. Crestani and K. Godary-Dejean, "Fault tolerance in control architectures for mobile robots: Fantasy or reality?" in *Proceedings of the 7th National Conference on Control Architectures of Robots*, Nancy, France, May 10-11, 2012.

[22] J. D. Crisman, C. Kanojia, and I. Zeid, "Graspar: A flexible, easily controllable robotic hand," *IEEE Robotics & Automation Magazine*, vol. 3, no. 2, pp. 32–38, June 1996.

[23] A. Damiano, G. L. Gatto, I. Marongiu, and A. Pisano, "Second-order sliding-mode control of dc drives," *IEEE Transactions on Industrial Electronics*, vol. 51, no. 2, pp. 364–373, April 2004.

[24] P. Davies, Y. Reaud, L. Dussud, and P. Woerther, "Mechanical behaviour of HMPE and aramid fibre ropes for deep sea handling operations," *Ocean Engineering*, vol. 38, no. 17, pp. 2208–2214, December 2011.

[25] A. De Luca and P. Lucibello, "A general algorithm for dynamic feedback linearization of robots with elastic joints," in *Proceedings of the IEEE International Conference on Robotics and Automation*, vol. 1, May 16-20, 1998, pp. 504–510.

[26] A. De Luca and R. Mattone, "Actuator failure detection and isolation using generalized momenta," vol. 1, September 14-19, 2003, pp. 634–639.

[27] A. De Luca and R. Mattone, "Sensorless robot collision detection and hybrid force/motion control," in *Proceedings of the IEEE International Conference on Robotics and Automation*, Barcelona, Spain, April 18-22, 2005, pp. 999–1004.

[28] A. De Luca, “Feedforward/feedback laws for the control of flexible robots,” vol. 1, April 24-28, 2000, pp. 233–240.

[29] A. De Luca, A. Albu-Schäffer, S. Haddadin, and G. Hirzinger, “Collision detection and safe reaction with the DLR-III lightweight manipulator arm,” in *Proceedings of the IEEE/RSJ International Conference on Intelligent Robots and Systems*, Beijing, China, October 9-15, 2006, pp. 1623–1630.

[30] A. De Luca and W. Book, “Robots with flexible elements,” in *Springer Handbook of Robotics*, B. Siciliano and O. Khatib, Eds. Springer, Berlin, Heidelberg, 2008, ch. 13, pp. 287–319.

[31] A. De Luca, B. Siciliano, and L. Zollo, “PD control with on-line gravity compensation for robots with elastic joints: Theory and experiments,” *Automatica*, vol. 41, no. 10, pp. 1809–1819, October 2005.

[32] A. De Santis, B. Siciliano, A. De Luca, and A. Bicchi, “An atlas of physical human–robot interaction,” *Mechanism and Machine Theory*, vol. 43, no. 3, pp. 253–270, March 2008.

[33] A. D. Dragan, S. Bauman, J. Forlizzi, and S. S. Srinivasa, “Effects of robot motion on human-robot collaboration,” in *Proceedings of the ACM/IEEE International Conference on Human-Robot Interaction*, Portland, Oregon, USA, March 2-5, 2015, pp. 51–58.

[34] H. Durrant-Whyte and T. C. Henderson, “Multisensor data fusion,” in *Springer Handbook of Robotics*, B. Siciliano and O. Khatib, Eds. Springer, Berlin, Heidelberg, 2008, ch. 25, pp. 585–610.

[35] K. Eder, C. Harper, and U. Leonards, “Towards the safety of human-in-the-loop robotics: Challenges and opportunities for safety assurance of robotic co-workers,” in *Proceedings of the IEEE International Symposium on Robot and Human Interactive Communication*, Edinburgh, UK, August 25-29 2014, pp. 660–665.

[36] R. Filippini, S. Sen, and A. Bicchi, “Toward soft robots you can depend on,” *IEEE Robotics Automation Magazine*, vol. 15, no. 3, pp. 31–41, September 2008.

[37] F. Flacco and A. De Luca, “Residual-based stiffness estimation in robots with flexible transmissions,” in *Proceedings of the IEEE International Conference on Robotics and Automation*, Shanghai, China, May 9-13, 2011, pp. 5541–5547.

[38] F. Flacco, A. De Luca, I. Sardellitti, and N. G. Tsagarakis, “Robust estimation of variable stiffness in flexible joints,” in *Proceedings of the IEEE/RSJ International Conference on Intelligent Robots and Systems*, San Francisco, CA, USA, September 25-30, 2011, pp. 4026–4033.

[39] F&P Robotics AG. Products. Datasheet_P-Arm2R_DE.pdf. P-Rob 2R website. [Online]. Available: https://www.fp-robotics.com/de/technology/ [Accessed: April 10, 2017]

[40] Franka Emika GmbH. Franka Emika. FRANKA-EMIKA-technical-data.pdf. Frank Emika website. [Online]. Available: https://www.franka.de/ [Accessed: April 10, 2017]

[41] B. Gonsior, D. Wollherr, and M. Buss, “Towards a dialog strategy for handling miscommunication in human-robot dialog,” in *Proceedings of the 19th International Symposium in Robot and Human Interactive Communication*, Viareggio, Italy, September 13-15, 2010, pp. 264–269.

[42] M. A. Goodrich and D. R. Olsen, “Seven principles of efficient human robot interaction,” in *Proceedings of the IEEE International Conference on Systems, Man and Cybernetics*, vol. 4, Washington, DC, USA, October 5-8, 2003, pp. 3943–3948.

[43] M. A. Goodrich and A. C. Schultz, “Human-robot interaction: A survey,” *Foundations and Trends in Human-Computer Interaction*, vol. 1, no. 3, pp. 203–275, February 2007.

[44] A. Grabiec, “Augmented reality-based robot state and process visualization on an industrial process automation example,” Master’s thesis, Technische Universität Darmstadt, Darmstadt, Germany, 2016.

[45] M. Grebenstein, A. Albu-Schäffer, T. Bahls, M. Chalon, O. Eiberger, W. Friedl, R. Gruber, S. Haddadin, U. Hagn, R. Haslinger, H. Höppner, S. Jörg, M. Nickl, A. Nothhelfer, F. Petit, J. Reill, N. Seitz, T. Wimböck, S. Wolf, T. Wüsthoff, and G. Hirzinger, “The DLR hand arm system,” in *Proceedings of the IEEE International Conference on Robotics and Automation*, Shanghai, China, May 9-13, 2011, pp. 3175–3182.

[46] S. A. Green, M. Billinghurst, X. Chen, and J. G. Chase, “Human-robot collaboration: A literature review and augmented reality approach in design,” *International Journal of Advanced Robotic Systems*, vol. 5, no. 1, pp. 1–18, January 2008.

[47] S. Haddadin, A. Albu-Schäffer, O. Eiberger, and G. Hirzinger, “New insights concerning intrinsic joint elasticity for safety,” in *Proceedings of the IEEE/RSJ International Conference on Intelligent Robots and Systems*, Taipei, Taiwan, October 18-22, 2010, pp. 2181–2187.

[48] S. Haddadin, A. Albu-Schäffer, A. De Luca, and G. Hirzinger, “Collision detection and reaction: A contribution to safe physical human-robot interaction,” in *Proceedings of the IEEE/RSJ International Conference on Intelligent Robots and Systems*, Nice, France, September 22-26, 2008, pp. 3356–3363.

[49] S. Haddadin, A. Albu-Schäffer, M. Frommberger, J. Rossmann, and G. Hirzinger, “The "DLR crash report": Towards a standard crash-testing protocol for robot safety - part I: Results,” in *Proceedings of the IEEE International Conference on Robotics and Automation*, Kobe, Japan, May 12-17, 2009, pp. 272–279.

[50] S. Haddadin, A. Albu-Schäffer, and G. Hirzinger, “Safety evaluation of physical human-robot interaction via crash-testing,” in *Proceedings of the Robotics: Science and Systems Conference*, Atlanta, USA, June 27-30, 2007, pp. 217–224.

[51] ——, “The role of the robot mass and velocity in physical human-robot interaction - part I: Non-constrained blunt impacts,” in *Proceedings of the IEEE International Conference on Robotics and Automation*, Pasadena, CA, USA, May 19-23, 2008, pp. 1331–1338.

[52] ——, “The role of the robot mass and velocity in physical human-robot interaction - part II: Constrained blunt impacts,” in *Proceedings of the IEEE International Conference on Robotics and Automation*, Pasadena, CA, USA, May 19-23, 2008, pp. 1339–1345.

[53] ——, “Soft-tissue injury in robotics,” in *Proceedings of the IEEE International Conference on Robotics and Automation*, Anchorage, AK, USA, May 3-7, 2010, pp. 3426–3433.

[54] S. Haddadin, A. Albu-Schäffer, and G. Hirzinger, “Requirements for safe robots: Measurements, analysis and new insights,” *The International Journal of Robotics Research*, vol. 28, no. 11-12, pp. 1507–1527, August 2009.

[55] S. Haddadin, M. Suppa, S. Fuchs, T. Bodenmüller, A. Albu-Schäffer, and G. Hirzinger, “Towards the robotic co-worker,” in *Robotics Research*, C. Pradalier, R. Siegwart, and G. Hirzinger, Eds. Springer, Berlin, Heidelberg, 2011, pp. 261–282.

[56] B. Halder and N. Sarkar, “Robust fault detection of a robotic manipulator,” *The International Journal of Robotics Research*, vol. 26, no. 3, pp. 273–285, March 2007.

[57] D. L. Hamilton, I. D. Walker, and J. K. Bennett, “Fault tolerance versus performance metrics for robot systems,” in *Proceedings of the IEEE International Conference on Robotics and Automation*, vol. 4, Minneapolis, MN, USA, April 22-28, 1996, pp. 3073–3080.

[58] G. Hirzinger, A. Albu-Schäffer, M. Hähnle, I. Schaefer, and N. Sporer, “On a new generation of torque controlled light-weight robots,” in *Proceedings of the IEEE International Conference on Robotics and Automation*, vol. 4, Seoul, South Korea, May 21-26, 2001, pp. 3356–3363.

[59] G. Hirzinger, N. Sporer, A. Albu-Schäffer, M. Hähnle, R. Krenn, A. Pascucci, and M. Schedl, “DLR’s torque-controlled light weight robot III - are we reaching the technological limits now?” in *Proceedings of the IEEE International Conference on Robotics and Automation*, vol. 2, Washington, DC, USA, May 11-15, 2002, pp. 1710–1716.

[60] N. Hogan, “Impedance control: An approach to manipulation: Part II—Implementation,” *Journal of Dynamic Systems, Measurement, and Control*, vol. 107, no. 1, pp. 8–16, March 1985.

[61] K. H. Hunt and F. R. E. Crossley, “Coefficient of restitution interpreted as damping in vibroimpact,” *Journal of Applied Mechanics*, vol. 42, no. 2, pp. 440–445, June 1975.

[62] Igus GmbH. robolink - modular system for robotics. robolink W website. [Online]. Available: http://www.igus.eu/wpck/6076/robolink [Accessed: January 13, 2017]

[63] R. Isermann, *Fault-Diagnosis Systems: An Introduction from Fault Detection to Fault Tolerance*. Springer-Verlag Berlin Heidelberg, 2006.

[64] *Determination of creep behaviour - Part 1: Tensile creep*, ISO Standard 899-1:2003, 2003.

[65] *Plastics - Standard atmospheres for conditioning and testing*, ISO Standard 291:2008, 2008.

[66] *Robots and robotic devices - Safety requirements for industrial robots - Part 1: Robots*, ISO Standard 10 218-1:2011, 2011.

[67] *Robots and robotic devices - Safety requirements for industrial robots - Part 2: Robot systems and integration*, ISO Standard 10 218-2:2011, 2011.

[68] *Robots and robotic devices - Collaborative robots*, ISO Technical Specification ISO/TS 15 066:2016, 2016.

[69] S. Jacobsen, E. Iversen, D. Knutti, R. Johnson, and K. Biggers, "Design of the Utah/M.I.T. dextrous hand," in *Proceedings of the IEEE International Conference on Robotics and Automation*, vol. 3, San Francisco, CA, USA, April 7-10, 1986, pp. 1520–1532.

[70] S. C. Jacobsen, H. Ko, E. K. Iversen, and C. C. Davis, "Antagonistic control of a tendon driven manipulator," in *Proceedings of the IEEE International Conference on Robotics and Automation*, vol. 3, May 14-19, 1989, pp. 1334–1339.

[71] F. Janabi-Sharifi, V. Hayward, and C.-S. J. Chen, "Discrete-time adaptive windowing for velocity estimation," *IEEE Transactions on Control Systems Technology*, vol. 8, no. 6, pp. 1003–1009, November 2000.

[72] R. E. Kalman, "A new approach to linear filtering and prediction problems," *Transactions of the ASME - Journal of Basic Engineering*, vol. 82, no. 1, pp. 35–45, March 1960.

[73] O. Khatib, "Inertial properties in robotic manipulation: An object-level framework," *The International Journal of Robotics Research*, vol. 14, no. 1, pp. 19–36, February 1995.

[74] E. Kilic, O. Baser, M. Dolen, and E. I. Konukseven, "An enhanced adaptive windowing technique for velocity and acceleration estimation using incremental position encoders," in *Proceedings of the International Conference on Signals and Electronic Circuits*, Gliwice, Poland, September 1-10, 2010, pp. 61–64.

[75] Kinova Incorporated. Robot arms. JACO^2_4DOF_Technical-specifications-v1.0.pdf, MICO^2_6DOF_Technical-specifications-v1.0.pdf. JACO and MICO websites. [Online]. Available: http://www.kinovarobotics.com/service-robotics/products/robot-arms/ [Accessed: April 10, 2017]

[76] J. Kirchhoff, "Parameter identification for a non-modular elastic joint robot arm for observer-based collision detection," Master's thesis, Technische Universität Darmstadt, Darmstadt, Germany, 2011.

[77] J. Kirchhoff and O. von Stryk, "Robust trajectory tracking control for an ultra lightweight tendon driven series elastic robot arm," in *Proceedings of the IEEE International Conference on Advanced Intelligent Mechatronics*, Banff, AB, Canada, July 12-15, 2016, pp. 1297–1304.

[78] ——, "New insights in synthetic fiber rope elongation and its detection for ultra lightweight tendon driven series elastic robots," in *Proceedings of the IEEE International Conference on Advanced Intelligent Mechatronics*, Munich, Germany, July 3-7, 2017, pp. 64–69.

[79] ——, "Velocity estimation for ultra lightweight tendon driven series elastic robots," *IEEE Robotics and Automation Letters*, vol. 3, no. 2, pp. 664–671, April 2018.

[80] KUKA AG. LBR iiwa. LBR iiwa product website. [Online]. Available: https://www.kuka.com/en-de/products/robot-systems/industrial-robots/lbr-iiwa [Accessed: April 10, 2017]

[81] J.-C. Laprie, "Dependability - its attributes, impairments and means," in *Predictably Dependable Computing Systems*, B. Randell, J.-C. Laprie, H. Kopetz, and B. Littlewood, Eds. Springer, Berlin, Heidelberg, 1995, pp. 3–18.

[82] L. Le Tien, A. Albu-Schäffer, A. De Luca, and G. Hirzinger, "Friction observer and compensation for control of robots with joint torque measurement," in *Proceedings of the IEEE/RSJ International Conference on Intelligent Robots and Systems*, Nice, France, September 22-26, 2008, pp. 3789–3795.

[83] L. Le Tien, A. Albu-Schäffer, and G. Hirzinger, "MIMO state feedback controller for a flexible joint robot with strong joint coupling," in *Proceedings of the IEEE International Conference on Robotics and Automation*, Roma, Italy, April 10-14, 2007, pp. 3824–3830.

[84] S.-H. Lee and J.-B. Song, "Acceleration estimator for low-velocity and low-acceleration regions based on encoder position data," *IEEE/ASME Transactions on Mechatronics*, vol. 6, no. 1, pp. 58–64, March 2001.

[85] T. Lens, J. Kunz, C. Trommer, A. Karguth, and O. von Stryk, "BioRob-Arm: A quickly deployable and intrinsically safe, light- weight robot arm for service robotics applications," in *Proceedings of the 41st International Symposium on Robotics (ISR 2010) / 6th German Conference on Robotics (ROBOTIK 2010)*, Munich, Germany, June 7-9, 2010, pp. 905–910.

[86] T. Lens, J. Kunz, and O. von Stryk, "Dynamic modeling of the 4 DoF BioRob series elastic robot arm for simulation and control," in *Proceedings of the International Conference on Simulation, Modeling, and Programming for Autonomous Robots*, ser. Lecture Notes in Computer Science, N. Ando, S. Balakirsky, T. Hemker, M. Reggiani, and O. von Stryk, Eds. Springer, Berlin, Heidelberg, November 15-18, 2010, pp. 411–422.

[87] T. Lens and O. von Stryk, "Design and dynamics model of a lightweight series elastic tendon-driven robot arm," in *Proceedings of the IEEE International Conference on Robotics and Automation*, Karlsruhe, Germany, May 6-10, 2013, pp. 4512–4518.

[88] T. Lens, "Physical human-robot interaction with a lightweight, elastic tendon driven robotic arm: Modeling, control, and safety analysis," Ph.D. dissertation, TU Darmstadt, Department of Computer Science, July 4, 2012.

[89] T. Lens, J. Kirchhoff, and O. von Stryk, "Dynamic modeling of elastic tendon actuators with tendon slackening," in *Proceedings of the IEEE-RAS International Conference on Humanoid Robots*, Osaka, Japan, November 29 - December 1, 2012, pp. 779–784.

[90] Y. Li and S. S. Ge, "Human-robot collaboration based on motion intention estimation," *IEEE/ASME Transactions on Mechatronics*, vol. 19, no. 3, pp. 1007–1014, June 2014.

[91] Y. Lian, H. Liu, Y. Zhang, and L. Li, "An experimental investigation on fatigue behaviors of HMPE ropes," *Ocean Engineering*, vol. 139, pp. 237–249, July 2017.

[92] G. Liu, "On velocity estimation using position measurements," in *Proceedings of the IEEE American Control Conference*, vol. 2, Anchorage, AK, USA, May 8-10, 2002, pp. 1115–1120.

[93] H. Liu, W. Huang, Y. Lian, and L. Li, "An experimental investigation on nonlinear behaviors of synthetic fiber ropes for deepwater moorings under cyclic loading," *Applied Ocean Research*, vol. 45, pp. 22–32, March 2014.

[94] F. Lotti, P. Tiezzi, G. Vassura, L. Biagiotti, and C. Melchiorri, "UBH 3: An anthropomorphic hand with simplified endo-skeletal structure and soft continuous fingerpads," in *Proceedings of the IEEE International Conference on Robotics and Automation*, vol. 5, New Orleans, LA, USA, April 26 - May 1, 2004, pp. 4736–4741.

[95] MABI AG Robotic. Products. Speedy 6 and Speedy 12 product websites. [Online]. Available: http://mabi-robotic.com/en/products [Accessed: April 10, 2017]

[96] E. Magrini and A. De Luca, "Hybrid force/velocity control for physical human-robot collaboration tasks," in *Proceedings of the IEEE/RSJ International Conference on Intelligent Robots and Systems*, Daejeon, South Korea, October 9-14, 2016, pp. 857–863.

[97] D. W. Marhefka and D. E. Orin, "Simulation of contact using a nonlinear damping model," in *Proceedings of the IEEE International Conference on Robotics and Automation*, vol. 2, April 22-28, 1996, pp. 1662–1668.

[98] Markets and Marktes. Collaborative robots market by payload (up to 5 kg, up to 10 kg, and above 10 kg), application, industry and geography - global forecast to 2022. [Online]. Available: http://www.marketsandmarkets.com/Market-Reports/collaborative-robot-market-194541294.html [Accessed: April 10, 2017]

[99] M. T. Mason, "Compliance and force control for computer controlled manipulators," *IEEE Transactions on Systems, Man and Cybernetics*, vol. 11, no. 6, pp. 418–432, June 1981.

[100] A. Mazumdar, S. J. Spencer, C. Hobart, J. Dabling, T. Blada, K. Dullea, M. Kuehl, and S. P. Buerger, "Synthetic fiber capstan drives for highly efficient, torque controlled, robotic applications," *IEEE Robotics and Automation Letters*, vol. 2, no. 2, pp. 554–561, April 2017.

[101] K. Mehrotra and P. R. Mahapatra, "A jerk model for tracking highly maneuvering targets," *IEEE Transactions on Aerospace and Electronic Systems*, vol. 33, no. 4, pp. 1094–1105, October 1997.

[102] M. Melia, M. Schmidt, B. Geissler, J. König, U. Krahn, H. J. Ottersbach, S. Letzel, and A. Muttray, "Measuring mechanical pain: The refinement and standardization of pressure pain threshold measurements," *Behavior Research Methods*, vol. 47, no. 1, pp. 216–227, March 2015.

[103] R. J. E. Merry, M. J. G. van de Molengraft, and M. Steinbuch, "Velocity and acceleration estimation for optical incremental encoders," *Mechatronics*, vol. 20, no. 1, pp. 20 – 26, February 2010.

[104] C. Morato, K. N. Kaipa, B. Zhao, and S. K. Gupta, "Toward safe human robot collaboration by using multiple kinects based real-time human tracking," *Journal of Computing and Information Science in Engineering*, vol. 14, no. 1, pp. 1–9, March 2014.

[105] R. Müller, M. Hessinger, H. F. Schlaak, and P. P. Pott, "Modelling and characterisation of twisted string actuation for usage in active knee orthoses," in *Proceedings of the 9th IFAC Symposium on Biological and Medical Systems*, vol. 48, no. 20, Berlin, Germany, August 31 - September 2, 2015, pp. 207–212.

[106] F. Nägele, M. Naumann, and A. Verl, "A framework for a fault tolerant and learning robotic assembly system," in *Proceedings of the 7th German Conference on Robotics (ROBOTIK 2012)*, Munich, Germany, May 21-22, 2012, pp. 1–6.

[107] C. Ott, A. Albu-Schäffer, A. Kugi, and G. Hirzinger, "On the passivity-based impedance control of flexible joint robots," *IEEE Transactions on Robotics*, vol. 24, no. 2, pp. 416–429, April 2008.

[108] C. Ott, R. Mukherjee, and Y. Nakamura, "Unified impedance and admittance control," in *Proceedings of the IEEE International Conference on Robotics and Automation*, Anchorage, AK, USA, May 3-7, 2010, pp. 554–561.

[109] C. Ott, *Cartesian Impedance Control of Redundant and Flexible-Joint Robots*. Springer-Verlag Berlin Heidelberg, 2008.

[110] C. Ott, A. Albu-Schäffer, A. Kugi, S. Stramigioli, and G. Hirzinger, "A passivity based cartesian impedance controller for flexible joint robots - part I: Torque feedback and gravity compensation," in *Proceedings of the IEEE International Conference on Robotics and Automation*, vol. 3, New Orleans, LA, USA, April 24 - May 1, 2004, pp. 2659–2665.

[111] C. Ott, R. Mukherjee, and Y. Nakamura, "A hybrid system framework for unified impedance and admittance control," *Journal of Intelligent & Robotic Systems*, vol. 78, no. 3-4, pp. 359–375, June 2015.

[112] G. Perner, L. Yousif, S. Rinderknecht, and P. Beckerle, "Feature extraction for fault diagnosis in series elastic actuators," in *Proceedings of the 3rd Conference on Control and Fault-Tolerant Systems*, Barcelona, Spain, September 7-9, 2016, pp. 220–226.

[113] R. Petrella, M. Tursini, L. Peretti, and M. Zigliotto, "Speed measurement algorithms for low-resolution incremental encoder equipped drives: A comparative analysis," in *Proceedings of the International Aegean Conference on Electrical Machines and Power Electronics*, Bodrum, Turkey, September 10-12, 2007, pp. 780–787.

[114] V. Potkonjak, B. Svetozarevic, K. Jovanovic, and O. Holland, "The puller-follower control of compliant and noncompliant antagonistic tendon drives in robotic systems," *International Journal of Advanced Robotic Systems*, vol. 8, no. 5, pp. 143–155, November 2011.

[115] G. A. Pratt and M. M. Williamson, "Series elastic actuators," in *Proceedings of the IEEE/RSJ International Conference on Intelligent Robots and Systems*, vol. 1, Pittsburgh, PA, USA, August 5-9, 1995, pp. 399–406.

[116] L. J. Puglisi, R. J. Saltaren, and C. E. Garcia Cena, "On the velocity and acceleration estimation from discrete time-position sensors," *Journal of Control Engineering and Applied Informatics*, vol. 17, no. 3, pp. 30–40, 2015.

[117] K. Radkhah, C. Maufroy, M. Maus, D. Scholz, A. Seyfarth, and O. von Stryk, "Concept and design of the biobiped1 robot for human-like walking and running," *International Journal of Humanoid Robotics*, vol. 8, no. 3, pp. 439–458, 2011.

[118] M. H. Raibert and J. J. Craig, "Hybrid position/force control of manipulators," *Journal of Dynamic Systems, Measurement, and Control*, vol. 103, no. 2, pp. 126–133, June 1981.

[119] Rethink Robotics Incorporated. Rethink Robotics | Advanced Robotics Technology. Baxter_Datasheet_Oct2015.pdf, Sawyer_Datasheet_Nov_2015_web.pdf. Baxter and Sawyer website. [Online]. Available: http://www.rethinkrobotics.com/ [Accessed: April 10, 2017]

[120] Robert Bosch Manufacturing Solutions GmbH. APAS website. 160923-Bosch-APAS-Broschure-deutsch-LoRes.pdf. APAS website. [Online]. Available: https://www.bosch-apas.com/en/home/ [Accessed: April 10, 2017]

[121] B. Rooks, "The harmonious robot," *Industrial Robot: An International Journal*, vol. 33, no. 2, pp. 125–130, 2006.

[122] Samson Rope, "Rope user's manual: Guide to rope selection, handling, usage, and retirement," Samson Rope Technologies Incorporated, Ferndale, WA, USA, Tech. Rep. No. 109101 2.5K 10/2016, 2016.

[123] C. Schindlbeck and S. Haddadin, "Unified passivity-based cartesian force/impedance control for rigid and flexible joint robots via task-energy tanks," in *Proceedings of the IEEE International Conference on Robotics and Automation*, Seattle, WA, USA, May 26-30, 2015, pp. 440–447.

[124] D. Scholz, C. Maufroy, S. Kurowski, K. Radkhah, O. von Stryk, and A. Seyfarth, "Simulation and experimental evaluation of the contribution of biarticular gastrocnemius structure to joint synchronization in human-inspired three-segmented elastic legs," in *Proceedings of the International Conference on Simulation, Modeling, and Programming for Autonomous Robots*, ser. Lecture Notes in Computer Science, I. Noda, N. Ando, D. Brugali, and J. J. Kuffner, Eds. Springer, Berlin, Heidelberg, November 5-8, 2012, pp. 251–260.

[125] W. Shaowei and W. Shanming, "Velocity and acceleration computations by single-dimensional kalman filter with adaptive noise variance," *Przeglad Elektrotechniczny*, vol. 88, no. 2, pp. 283–287, January 2012.

[126] D. Shin, I. Sardellitti, Y.-L. Park, O. Khatib, and M. Cutkosky, "Design and control of a bio-inspired human-friendly robot," *The International Journal of Robotics Research*, vol. 29, no. 5, pp. 571–584, April 2010.

[127] M. W. Spong, "Modeling and control of elastic joint robots," *Journal of Dynamic Systems, Measurement, and Control*, vol. 109, no. 4, pp. 310–318, December 1987.

[128] M. P. Summers, "Rope selection for rope drive transmissions used in robotic manipulation," Bachelor's thesis, Oregon State University, Corvallis, OR, USA, 2010.

[129] R. Tinós, M. H. Terra, and M. Bergerman, "A fault tolerance framework for cooperative robotic manipulators," *Control Engineering Practice*, vol. 15, no. 5, pp. 615–625, May 2007.

[130] P. Tomei, "A simple PD controller for robots with elastic joints," *IEEE Transactions on Automatic Control*, vol. 36, no. 10, pp. 1208–1213, October 1991.

[131] Universal Robots. Actual center of mass for robot - 17264. [Online]. Available: https://www.universal-robots.com/how-tos-and-faqs/faq/ur-faq/actual-center-of-mass-for-robot-17264/ [Accessed: March 11, 2016]

[132] Universal Robots. Collaborative Industrial Robotic Robot Arms. 101081_199917_ur3_technical_details_web_a4_art03_rls_de.pdf, 10108_199917_ur5_technical_details_web_a4_art03_rls_de.pdf, 101081_199917_ur10_technical_details_web_a4_art03_rls_de.pdf. UR3, UR5, and UR10 website. [Online]. Available: https://www.universal-robots.com/ [Accessed: April 10, 2017]

[133] R. Van Ham, T. Sugar, B. Vanderborght, K. Hollander, and D. Lefeber, "Compliant actuator designs," *IEEE Robotics & Automation Magazine*, vol. 16, no. 3, pp. 81–94, September 2009.

[134] S. Vannei, Y. Mizutani, G. Endo, Y. Suzuki, and A. Todoroki, "Consecutive impact loading and preloading effect on stiffness of woven synthetic-fiber rope," *Journal of Textile Science and Technology*, vol. 3, pp. 1–16, February 2017.

[135] *Design Methodology for Mechatronic Systems*, Verein Deutscher Ingenieure (VDI) Guideline 2206, June 2004.

[136] M. L. Visinsky, J. R. Cavallaro, and I. D. Walker, "Robotic fault detection and fault tolerance: A survey," *Reliability Engineering and System Safety*, vol. 46, no. 2, pp. 139–158, 1994.

[137] M. Vukobratovic, D. Surdilovic, Y. Ekalo, and D. Katic, *Control of Robots in Contact Tasks: A Survey*. World Scientific, 2009, ch. 1, pp. 1–76.

[138] G. Welch and G. Bishop, "An introduction to the kalman filter," in *Computer Graphics*, SIGGRAPH 2001 Course Pack ed., ser. Annual Conference on Computer Graphics & Interactive Techniques. Los Angeles, CA, USA: ACM Press, Addison-Wesley, August 12-17, 2001, Course 8.

[139] J. G. Ziegler and N. B. Nichols, "Optimum settings for automatic controllers," *Transactions of the ASME*, vol. 64, pp. 759–768, November 1942.

[140] M. Zinn, O. Khatib, B. Roth, and J. K. Salisbury, "Playing it safe [human-friendly robots]," *IEEE Robotics and Automation Magazine*, vol. 11, no. 2, pp. 12–21, June 2004.

[141] M. Zinn, B. Roth, O. Khatib, and J. K. Salisbury, "A new actuation approach for human friendly robot design," *The International Journal of Robotics Research*, vol. 23, no. 4-5, pp. 379–398, April 2004.

[142] L. Zollo, B. Siciliano, A. De Luca, E. Guglielmelli, and P. Dario, "Compliance control for an anthropomorphic robot with elastic joints: Theory and experiments," *Journal of Dynamic Systems, Measurement, and Control*, vol. 127, no. 3, pp. 321–328, July 2004.

Publications

Journal Papers

Jérôme Kirchhoff and Oskar von Stryk. Velocity estimation for ultra lightweight tendon driven series elastic robots. *IEEE Robotics and Automation Letters*, 3(2):664–671, April 2018.

Conference Papers

Thomas Lens, Jérôme Kirchhoff, and Oskar von Stryk. Dynamic modeling of elastic tendon actuators with tendon slackening. In *Proceedings of the IEEE-RAS International Conference on Humanoid Robots*, pages 779–784, Osaka, Japan, November 29 - December 1, 2012.

Jérôme Kirchhoff and Oskar von Stryk. Robust trajectory tracking control for an ultra lightweight tendon driven series elastic robot arm. In *Proceedings of the IEEE International Conference on Advanced Intelligent Mechatronics*, pages 1297–1304, Banff, AB, Canada, July 12-15, 2016.

Jérôme Kirchhoff and Oskar von Stryk. New insights in synthetic fiber rope elongation and its detection for ultra lightweight tendon driven series elastic robots. In *Proceedings of the IEEE International Conference on Advanced Intelligent Mechatronics*, pages 64–69, Munich, Germany, July 3-7, 2017.

Wissenschaftlicher Werdegang

Der Lebenslauf ist in der Online-Verison aus Gründen des Datenschutzes nicht enthalten.

Erklärung[1]

Hiermit erkläre ich, dass ich die vorliegende Arbeit, mit Ausnahme der ausdrücklich genannten Hilfsmittel, selbständig verfasst habe.

[1] gemäß § 9 Abs. 1 der Promotionsordnung der TU Darmstadt